

# Non-axially symmetric field and trajectory calculations for the KATRIN-experiment

Diplomarbeit  
vorgelegt  
von

**Benjamin Leiber**

Am Institut für Experimentelle Kernphysik (IEKP)  
Karlsruhe Institute of Technology (KIT)

Referent: Prof. Dr. G. Drexlin  
Korreferent: Prof. Dr. W. de Boer

Bearbeitungszeit: 01. Mai 2009 – 30. April 2010



# Erklärung

Hiermit bestätige ich, dass ich die vorliegende Arbeit selbst verfasst und keine anderen als die angegebenen Quellen und Hilfsmittel verwendet und diese im Text kenntlich gemacht habe.

Benjamin Leiber, April 2010



# Zusammenfassung

Das **KARlsruher TRItium Neutrino Experiment** wird die Masse des Elektron Antineutrinos mit einer Sensitivität von  $0.2 \text{ eV}/c^2$  (90%C.L.) über die Messung des Tritium  $\beta$ -Spektrums in der Nähe des Endpunktes bestimmen.

Um die Energie der Zerfallselektronen zu analysieren, werden diese in einem elektrostatischen Spektrometer nach dem MAC-E Filter-Prinzip entlang von Magnetfeldlinien geführt. Durch die adiabatische Änderung des Feldes um einen Faktor von 20.000 wird die transversale Energie der Zerfallselektronen in longitudinale umgewandelt, welche dann mit dem elektrischen Retardierungspotential analysiert wird.

Zur Optimierung des experimentellen Aufbaus werden Simulationen des elektromagnetischen Designs durchgeführt. Dies erfordert eine flexible und modulare Software, um die auftretenden elektromagnetischen Felder und damit auch die Teilchenbahnen der Zerfallselektronen im Experiment mit großer Genauigkeit zu simulieren. Besonderes Augenmerk galt im Rahmen dieser Diplomarbeit der Nicht-Axialsymmetrie des Magnetfeldes, wie es z.B. durch Verformungen des Luftspulensystems, welches das Hauptspektrometer umschließt und den magnetischen Materialien in den Wänden der Spektrometerhalle verursacht wird.

In dem nun Folgenden sollen die einzelnen Kapitel dieser Arbeit kurz vorgestellt und ein kurzer Überblick über sie gegeben werden. Eine ausführliche Darstellung inklusive dazugehöriger Quellenangaben ist im englischsprachigen Haupttext zu finden.

1. **Einleitung** Neutrinos sind seit ihrer Postulation durch W. Pauli in den 30er Jahren des 20ten Jahrhundert Gegenstand intensiver Forschungen. Als “Geisterteilchen”, die nur schwach wechselwirken entzogen sie sich lange der direkten Beobachtung und können auch heute nur mit Hilfe von Prozessen, in denen durch sie geladene Teilchen erzeugt werden, nachgewiesen werden.

Im Standard-Modell der Teilchenphysik gelten die Neutrinos als masselos. Das Super-Kamiokande Experiment wies jedoch durch die Beobachtung von Neutrinooszillationen nach, dass es sich bei Neutrinos um massive Teilchen handeln muss. Allerdings liefern Neutrino-Oszillations-Experimente keine absoluten Werte für die Neutrinomassen, lediglich Massendifferenzen, die aus Mischverhältnissen abgeleitet werden.

Zur absoluten Massenbestimmung gibt es eine Reihe anderer Methoden, die sich grob in zwei Kategorien einteilen lassen: direkt und indirekt. Die indirekten Methoden leiten aus kosmologischen und astronomischen Beobachtungen Grenzen für die Summe der Neutrinomassen her, die allerdings sehr stark modellabhängig sind. Zu den direkten Nachweismethoden gehören die Suche

nach dem neutrinolosen Doppelbeta-Zerfall, die aber ebenfalls stark modellabhängig ist und die kinematische Vermessung des Myon- und Tau-Zerfalls und im Speziellen die von  $\beta$ -Zerfällen. Diese brauchen keine Modellannahmen zu treffen, da sie nur die Impuls- und Energieerhaltung voraussetzen. Das KATRIN Experiment verfolgt einen solch modellunabhängigen Ansatz und wird das  $\beta$ -Spektrum des Tritium-Zerfalls nahe dessen Endpunkt vermessen.

2. **Das KATRIN Experiment** Die aktuelle Obergrenze für die Masse des Elektron-Antineutrinos wurde durch die beiden Experimente in Troitsk und Mainz, die wie KATRIN den Tritium- $\beta$ -Zerfall untersuchten, aufgestellt, und liegt bei  $2.0 \text{ eV}/c^2$ . KATRIN soll diese Obergrenze um eine Größenordnung verbessern und sie damit auf  $0.2 \text{ eV}/c^2$  reduzieren. Dies erfordert eine signifikante Verbesserung der Hauptkomponenten des Experiments im Vergleich zu den Vorgängerexperimenten.

Die Energie der Zerfallselektronen wird analog zu den Vorgängerexperimenten mit Hilfe eines sogenannten MAC-E Filters vermessen. Dieses elektrostatische Spektrometer blockiert Elektronen unterhalb einer bestimmaren Energie, so dass ein integriertes Spektrum aufgenommen werden kann. Ein Magnetfeld dient zur Führung der Elektronen von der Quelle zum Detektor, gleichzeitig wird dieses innerhalb der Spektrometer so verringert, dass die transversale Energie der Elektronen in longitudinale umgewandelt wird. Dieses Prinzip heisst magnetische adiabatische Kollimation. Im Bereich des kleinsten Magnetfeldes, der sogenannten Analysierebene erreicht das elektrische Retardierungspotential seinen Maximalwert. Hier haben die Elektronen minimale transversale Energie und laufen gegen die Potentialbarriere an. Nur Elektronen mit größerer kinetischer Energie als die Barriere werden transmittiert und gelangen zum Detektor. Die Zentrale Komponente hierbei ist der MAC-E Filter, der sowohl möglichst die gesamte transversale in longitudinale Energie umwandeln, eine hohe Transmittivität für Signal-Elektronen und eine niedrige Rate an Sekundär-Elektronen haben soll. Es gilt also ihn in dieserlei Hinsichten zu optimieren.

3. **Methoden zur elektrischen und magnetischen Feldberechnung** Das Zusammenspiel von statischen elektrischen und magnetischen Feldern ist wichtig für die Funktion der Spektrometer. Um ihre Eigenschaften ohne experimentellen Aufwand zu studieren und um Anpassungen am elektromagnetischen Design abzuschätzen, wurden in der Vergangenheit verschiedene, auf der Programmiersprache C basierende Programme verwendet. Die Routinen zur magnetischen und elektrischen Feldberechnung verwenden einerseits die numerische Integration von elliptischen Integralen und andererseits eine Legendre-Polynom-Entwicklung, die besonders schnell ist. Im Rahmen dieser Arbeit wurden die C-Programme überarbeitet und in eine objektoriente Form in der Programmiersprache C++ gebracht. Sie sind nun flexibel und benutzerfreundlich in dem Programmpaket KAFCA zusammengefasst. Zusätzlich zur Modernisierung bestehender Programme wurden zwei Feldberechnungen für nicht axialsymmetrische Magnetfelder und eine universell einsetzbare Interpolationsmethode aus bestehenden C-routinen neu implementiert. Diese bilden das in C++ geschriebene KNAXS-Programmpaket.
4. **Bahnverfolgung geladener Teilchen** Um die Auswirkungen der elektrischen und magnetischen Felder auf die adiabatische Energietransformation und die

Transmission der Elektronen im Experiment zu untersuchen, braucht man Routinen zur Simulation der Elektron-Bewegung. Die Bewegungsgleichung eines Elektrons im elektromagnetischen Feld ist bestimmt durch die Lorentz-Kraft. Diese lässt sich durch verschiedene Verfahren numerisch lösen. Die Runge-Kutta Methoden verbinden hierbei hohe Geschwindigkeit mit ausgezeichneter Präzision. Zudem kann man die Bahnverfolgung durch geschickte, dynamische Wahl der Schrittgröße weiter optimieren. Für sehr große Schrittgrößen wird die numerische Lösung der Lorentz-Gleichung allerdings sehr ungenau. In diesem Fall besteht die Möglichkeit eine adiabatische Näherung der Teilchenbahn zu verwenden. Bei dieser Näherung wird lediglich der Weg des Führungszentrums der Zyklotronbahn des Elektrons genau berechnet und, abhängig vom Magnetfeld, anschließend eine Bewegung senkrecht dazu addiert. Diese Näherung bietet einen enormen Geschwindigkeitsgewinn, allerdings nur in Bereichen in denen sich das Elektron adiabatisch bewegt.

Dank der Flexibilität der Runge-Kutta Methode, lassen sich damit alle möglichen Differentialgleichungssysteme erster Ordnung lösen. So kann man damit analog zur adiabatischen Näherung auch Feldlinien berechnen, die ebenfalls einer "Kraft" in Richtung des Feldvektors folgen.

Abschließend ist es für die Untersuchung vieler Probleme wichtig, wo sich das Teilchen relativ zur felderzeugenden Geometrie befindet und ob es auf bestimmte Körper wie z.B. einen Elektrodendraht oder den Detektor trifft. Zu diesem Zweck benutzt man eine dreidimensionale Abstandsberechnung, die auf einfachen Vektorbeziehungen basiert.

5. **Implementierung** Die in den vorangegangenen zwei Kapiteln vorgestellten Methoden zur Feld- und Teilchenbahnberechnung, existierten in der Mehrheit bereits als C-Programme, welche, wenn überhaupt, nur schwer miteinander zu kombinieren und zu verwenden waren. Mit Hilfe von F. Glück, S. Mertens und mit Beiträgen von N. Wandkowsky wurde während dieser Diplomarbeit die Anstrengung unternommen, die Feldberechnungsmethoden objektorientiert umzugestalten, sie zu erweitern und ein Bahnrechnungs-System zu schaffen, welches vielseitig und komfortabel zu bedienen ist. Erreicht wurde dies durch langüberlegte Planung und konsequente Umsetzung objektorientierter Ansätze wie das Klassen- und das Vererbungsprinzip. Dies führte zu der nun existierenden Software bestehend aus den Programmpaketen KTrack, KAFA und KNAXS, die dank ihres logischen Aufbaus komplizierte Berechnungen mit einfacher Bedienung und hoher Geschwindigkeit verbindet.

Um die Berechnungsgeschwindigkeit bei statischen Feldern weiter zu erhöhen enthält KNAXS die Hermite-3D-Interpolationsmethode, die sich durch sehr hohe Präzision bei gleichzeitig enormer Berechnungsgeschwindigkeit bei der Interpolation von homogenen Felder auszeichnet.

6. **Untersuchung von Untergrund, verursacht durch nicht axialsymmetrische Felder** Magnetfeldmessungen in der KATRIN-Halle und Messungen der Verformung des Luftspulensystems lassen auf ein magnetisches Streufeld, das über den ursprünglichen Erwartungen liegt schließen. Deshalb ist es wichtig, die Auswirkungen solchen Streufelder auf das Experiment genau zu kennen. Mit Hilfe der KNAXS Software lassen sich Modelle, der Verformung sowie der magnetischen Materialien in Hallenwänden und -böden erstellen, die die Messungen wiedergeben.

Mit diesen Modellen kann man wiederum mit Hilfe von KTrack die Auswirkungen der Streufelder auf Teilchenbahnen im Experiment berechnen. Die Berechnungen zeigen, dass Signal-Elektronen nur unbedeutende Ablenkungen durch die magnetischen Streufelder erfahren. Anders sieht es aus für Sekundärelektronen, die durch Hintergrund-Strahlung und kosmische Teilchen aus den Wänden des Hauptspektrometers ausgeschlagen werden. Es wird angenommen, dass etwa  $10^7$  solcher Teilchen pro Sekunde auf der inneren Oberfläche des Tanks entstehen. Die niederenergetischen von ihnen können gespeichert werden und eine radiale Drift, verursacht durch die magnetische Streufelder in den Flussschlauch vollführen. Da sich diese Elektronen im Maximum des Streuquerschnitts mit Restgasmolekülen befinden, ist es sehr wahrscheinlich, dass sie eine Art von Untergrundsignal durch Restgasionisierung oder Streuung in Richtung des Detektors verursachen.

- 7. Zusammenfassung und Ausblick** Zusammenfassend lässt sich sagen, dass mit der Erweiterung und Verbesserung der vorhandenen Simulationswerkzeuge ein guter Weg beschritten wurde und die Entwicklung der Programme auch in Zukunft vorangetrieben werden wird. Zudem ist es nun möglich, verhältnismäßig komplizierte Simulationen schnell und einfach zu konfigurieren und auch nicht-axialsymmetrische Feldbeiträge in die Bahnverfolgung mitein zu beziehen.

In Zukunft wird eine große Monte-Carlo-Simulation der Elektronen, die von den Spektrometerwänden starten, für Vor- und Hauptspektrometer durchgeführt werden, in welcher die tatsächlichen Sekundärelektronen-Verteilungen und -Spektren berücksichtigt werden. Mit Simulationen dieser Art lässt sich die durch die magnetischen Streufelder verursachte Untergrundrate im Experiment studieren.

# Contents

<b>1</b>	<b>Introduction</b>	<b>1</b>
1.1	Evidence for massive neutrinos . . . . .	1
1.1.1	Atmospheric neutrino anomaly . . . . .	1
1.1.2	The solar neutrino problem . . . . .	1
1.2	Neutrino oscillations . . . . .	3
1.2.1	Measurements of the parameters of neutrino oscillation . . . . .	4
1.2.2	Conclusions . . . . .	6
1.3	Direct measurements of neutrino mass . . . . .	6
1.3.1	$\beta$ -decay . . . . .	7
1.3.2	$\pi$ - and $\tau$ -decay . . . . .	9
1.3.3	Neutrinoless double- $\beta$ -decay . . . . .	10
1.4	Indirect measurements of the neutrino mass . . . . .	10
<b>2</b>	<b>The KATRIN experiment</b>	<b>13</b>
2.1	The tritium $\beta$ -decay . . . . .	13
2.2	Basic setup . . . . .	14
2.2.1	WGTS . . . . .	14
2.2.2	Transport section . . . . .	14
2.2.3	Spectrometers . . . . .	15
2.2.4	Detector . . . . .	15
2.3	MAC-E filter . . . . .	16
2.3.1	Principle . . . . .	16
2.3.2	Characteristics . . . . .	17
2.3.3	KATRIN spectrometers . . . . .	20
2.3.4	Aircoil system . . . . .	22
2.3.5	Background . . . . .	22
<b>3</b>	<b>Methods for electric and magnetic field-calculation</b>	<b>25</b>
3.1	Magnetic field calculation . . . . .	25
3.1.1	Line-segment discretization methods . . . . .	25
3.1.1.1	Integrated Biot-Savart . . . . .	26
3.1.1.2	Magnetic dipole-bars . . . . .	27
3.1.2	Legendre polynomial expansion . . . . .	28
3.1.2.1	Elliptic Integrals . . . . .	28
3.1.2.2	Zonal Harmonic Expansion . . . . .	29
3.1.2.3	Application . . . . .	30
3.2	Electric field calculation . . . . .	32
3.2.1	Boundary element method . . . . .	32
3.2.2	Legendre polynomial expansion . . . . .	34

3.3	Three-dimensional Hermite-interpolation . . . . .	34
3.3.1	Motivation . . . . .	34
3.3.2	Theory . . . . .	35
<b>4</b>	<b>Tracking of charged particles</b>	<b>37</b>
4.1	The Runge-Kutta method . . . . .	37
4.2	Particle motion in general force fields . . . . .	39
4.3	Charged particle motion in electric and magnetic fields . . . . .	39
4.4	Field lines . . . . .	40
4.5	Adiabatic approximation . . . . .	41
4.6	Distance calculation . . . . .	42
<b>5</b>	<b>Code implementation</b>	<b>45</b>
5.1	Overview . . . . .	45
5.2	Field classes . . . . .	46
5.2.1	Magfield3 . . . . .	47
5.2.2	Elfield2 . . . . .	48
5.2.3	Elfield32 . . . . .	49
5.2.4	Elfield33 . . . . .	49
5.2.5	BiotSavart . . . . .	51
5.2.6	MagMaterials . . . . .	52
5.2.7	Interpolation . . . . .	53
5.3	Tracking classes . . . . .	54
5.3.1	KTrackParticle . . . . .	55
5.3.2	StepSize . . . . .	55
5.3.3	DiffEqSolver . . . . .	56
5.3.4	StepComputer . . . . .	56
5.4	Comparison . . . . .	57
5.4.1	Ktrack compared to singletraj.c . . . . .	57
5.4.2	Interpolation precision and computation time . . . . .	58
<b>6</b>	<b>Investigation of background due to non-axially-symmetric fields</b>	<b>63</b>
6.1	Magnetic shielding . . . . .	63
6.2	Non-axially symmetric field contributions . . . . .	64
6.2.1	Deformed LFCS . . . . .	65
6.2.2	Magnetic materials in the building's walls . . . . .	65
6.3	Particle tracks influenced by non-axisymmetric magnetic fields . . . . .	66
<b>7</b>	<b>Summary and outlook</b>	<b>69</b>
	<b>Bibliography</b>	<b>71</b>

# 1. Introduction

Since their postulation in 1930 by W. Pauli, neutrinos have been the subject of great scientific interest. Due to their elusive nature, the observation and investigation of neutrinos is a technically and mentally challenging branch of astroparticle physics. The observation of the oscillation of atmospheric neutrinos in 1998 by the Super-Kamiokande experiment laid the corner stone for a new generation of neutrino experiments. These intend to further investigate the properties of neutrinos and in particular search for the masses of the neutrinos.

This chapter will give a short overview to today's questions in neutrino physics and the experimental states. At first the numerous evidences for massive neutrinos will be discussed, as they were discovered by various experiments. This is followed by a brief annotation of neutrino oscillations and their parameters. The chapter will close with a description of the main aspects used for direct measurements of neutrino masses, followed by an outline.

## 1.1 Evidence for massive neutrinos

### 1.1.1 Atmospheric neutrino anomaly

Atmospheric neutrinos are produced in interactions of cosmic rays with atomic nuclei of the Earth-atmosphere. Experiments like Kamiokande [H<sup>+</sup>88] that used water-Cherenkov-detectors and Soudan 2 [A<sup>+</sup>97], Frejus [B<sup>+</sup>89] and NUSEX [B<sup>+</sup>82] which used calorimeter measured the flux of atmospheric  $\nu_\mu$  and  $\nu_e$  with directional resolution. It was shown that the ratio  $r = \nu_\mu/\nu_e$  varied with the zenith-angle (see figure 1.1). The ratio  $r_b$  of atmospheric neutrinos that travelled through Earth and reached the detector from below was found to be smaller than the ratio  $r_a$  of atmospheric neutrinos that travelled a much smaller distance coming directly from above. This was the first irrevocable evidence of  $\nu_\mu$  oscillating into  $\nu_e$  and therefore non-zero neutrino masses.

### 1.1.2 The solar neutrino problem

The so called solar neutrinos have their origin within the sun. Solar neutrinos are of special interest, because, on the one hand, they yield information about the inner

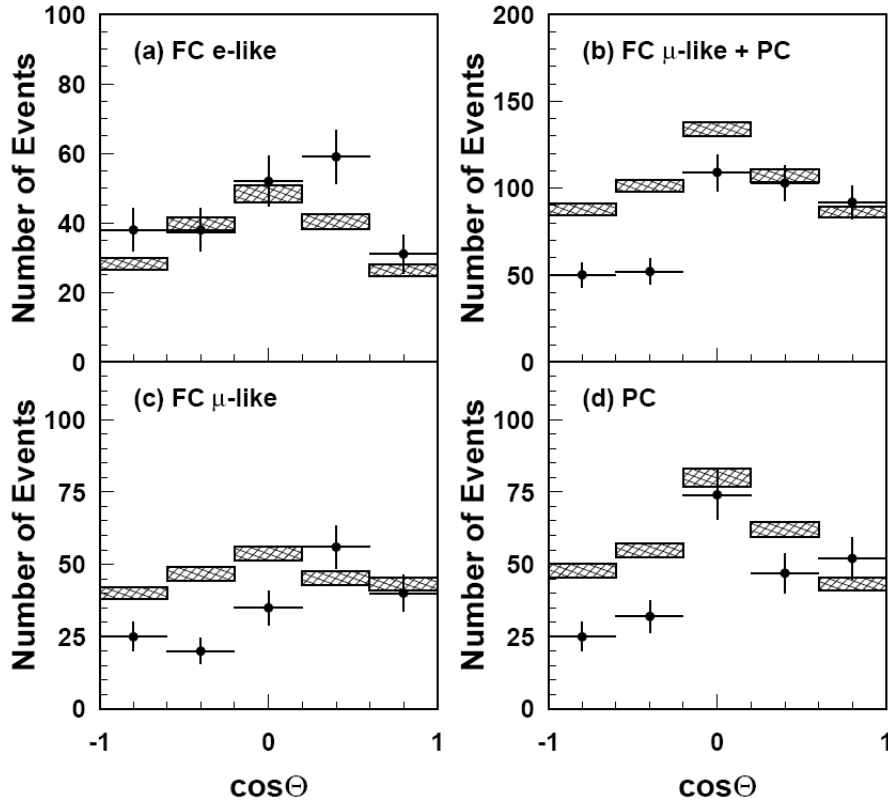
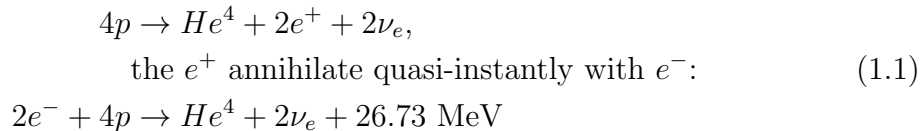


Figure 1.1: Zenith angle distributions for: (a)  $e$ -like events, (b)  $\mu$ -like fully- and partially-contained events, (c)  $\mu$ -like events and (d) all partially-contained events.  $\cos \theta = 1$  means down-going. The histograms with the shaded error bars show the Monte Carlo predictions with their statistical uncertainties. Figure taken from [aaa98]

sun and the ongoing processes there, and, on the other hand, they allow us to study neutrinos, that have relative low energies ( $\langle E_\nu \rangle \approx 0.3$  MeV) and travelled a long way through the sun-matter and the space between Earth and sun. The neutrinos in the sun are produced through the exothermic thermo-nuclear fusion of Hydrogen to Helium:



This so called  $pp$ -reaction takes place in the deep inner of the sun and is the source of the vast majority of solar neutrinos. On an average, only 2% of the released energy are given to the both neutrinos, thus giving them a distinct energy signature. There exist other processes in the sun that have far smaller contribution to the total solar neutrino flux and which have their own distinct energy signature (see Figure 1.2).

There have been several experiments that targeted to measure the flux of solar neutrinos in different energy regimes. Radiochemical experiments like the  $Cl^{37}$ -Experiment (Homestake) [Dav94], GALLEX [H<sup>+</sup>99] and SAGE [A<sup>+</sup>02a] count the rate of  $\nu$ -induced inverse  $\beta$ -decays. The Kamiokande- and the Super-Kamiokande experiments [F<sup>+</sup>98] used a water-Cherenkov-detector to look for  $\nu_e$ -scattering. Those

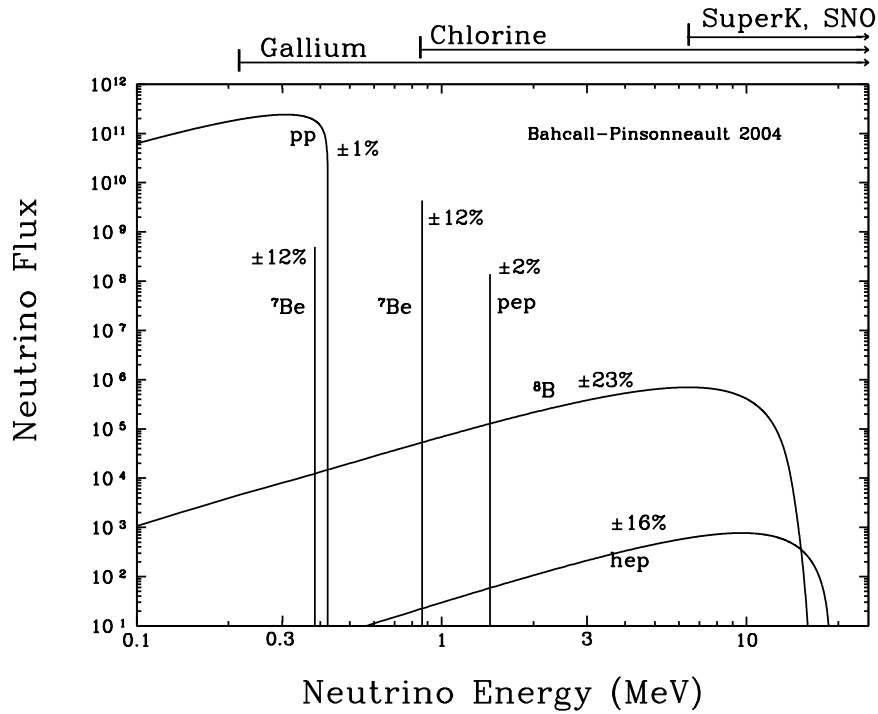


Figure 1.2: Solar neutrino energy spectrum for the SSM. Figure taken from [BPG04]

experiments only measured 32-64% of the solar neutrino flux predicted by the SSM<sup>1</sup>. This deficit caused the so called *solar neutrino problem*. An explanation for this disappearance of  $\nu_e$  are the so called neutrino-flavour-oscillations. This means that neutrinos have massive eigenstates that are not identical to the weak interaction eigenstates.

## 1.2 Neutrino oscillations

As the weak interaction eigenstates of the neutrinos do not correspond to their mass eigenstates, they can be expressed as superposition of them:

$$|\nu_\alpha\rangle = \sum_i U_{\alpha i} |\nu_i\rangle \quad (1.2)$$

with  $\alpha$  being the neutrino flavour,  $i$  the number of the mass eigenstate and  $U_{\alpha i}$  the mixing matrix called Maki-Nakagawa-Sakata-Pontecorvo-matrix. The mass eigenstates  $|\nu_i\rangle$  are stationary and can be propagated into time dependent form:

$$|\nu_i(t)\rangle = e^{-iE_i t} |\nu_i\rangle \quad (1.3)$$

A flavourstate  $|\nu_\alpha\rangle$  that is pure at the time  $t = 0$  propagates into:

$$|\nu(t)\rangle = \sum_i U_{\alpha i} e^{-iE_i t} |\nu_i\rangle = \sum_{i,\beta} U_{\alpha i} U_{\beta i}^* e^{-iE_i t} |\nu_\beta\rangle \quad (1.4)$$

<sup>1</sup>Standard Sun Model

For the transition-probability from flavour  $\alpha \rightarrow \beta$ , in the ultra-relativistic limit we get the transition amplitudes [GGN03], [Kay03]:

$$\begin{aligned}
P(\nu_\alpha \rightarrow \nu_\beta) &= |\langle \nu_\beta(t) | \nu_\alpha(t) \rangle|^2 = \left| \sum_i U_{\alpha i} U_{\beta i}^* e^{-\frac{im_i^2 L}{2E}} \right|^2 \\
&= \delta_{\alpha\beta} - 4 \sum_{i>j} \text{Re}(U_{\alpha i}^* U_{\beta i} U_{\alpha j} U_{\beta j}^*) \sin^2 \left( \frac{\Delta m_{ij}^2 L}{4E} \right) \\
&\quad + 2 \sum_{i>j} \text{Im}(U_{\alpha i}^* U_{\beta i} U_{\alpha j} U_{\beta j}^*) \sin^2 \left( \frac{\Delta m_{ij}^2 L}{2E} \right)
\end{aligned} \tag{1.5}$$

the oscillation phase is given through  $\Delta m_{ij}^2 \equiv m_i^2 - m_j^2$ . This model is able to describe the disappearance of neutrinos of a certain flavour  $\alpha$ , depending on their energy and oscillation length as well as the appearance of neutrinos of a flavour  $\beta$  different from the flavour  $\alpha$  which was emitted at the source.

### 1.2.1 Measurements of the parameters of neutrino oscillation

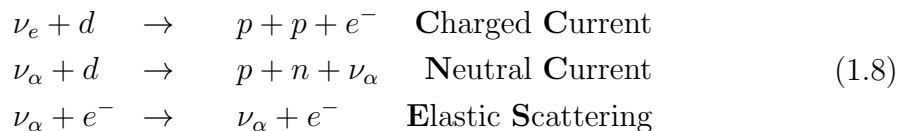
**Atmospheric neutrinos** The matrix  $U$  can be decomposed into rotation matrices that describe the mixing between the single states  $\nu_i$ . Data from the Super-Kamiokande experiment showed that the number of atmospheric  $\nu_\mu$  that reached the detector is dependent on the incident angle. The muon neutrinos that come from below have to travel a longer path through the Earth and therefore have a greater possibility to oscillate into tau neutrinos. With the available experimental data, the parameter  $\Theta_{23}$  of the mixing matrix  $U$  was determined to a limit of:

$$\sin^2(2\Theta_{23}) > 0.92 \tag{1.6}$$

and the mass difference  $\Delta m_{23}^2$  was narrowed down to the range [A<sup>+</sup>05d]:

$$1.5 \cdot 10^{-3} \text{eV}^2 < \Delta m_{23}^2 < 3.4 \cdot 10^{-3} \text{eV}^2 \tag{1.7}$$

**Solar neutrinos** The SNO experiment [A<sup>+</sup>02b] was able to measure the total solar neutrino flux of all flavours, as well as the flux of electron neutrinos. To achieve this, three different reactions are used:



The experiment came to the results that only one third of the electron neutrinos originating from the Sun still have their initial flavour when reaching the detector [A<sup>+</sup>05a]:

$$\frac{\phi(\nu_e)}{\phi(\nu_e) + \phi(\nu_{\mu,\tau})} = 0.340 \pm 0.023_{-0.031}^{+0.029} \tag{1.9}$$

Knowing that the Sun only emits electron neutrinos, this measurement is a strong indicator for neutrino oscillations. Furthermore, the summed flux of all reactions is consistent with the flux of solar neutrinos predicted by the SSM (shown in figure 1.3). A global fit of all available solar neutrino data gives the oscillation parameters with

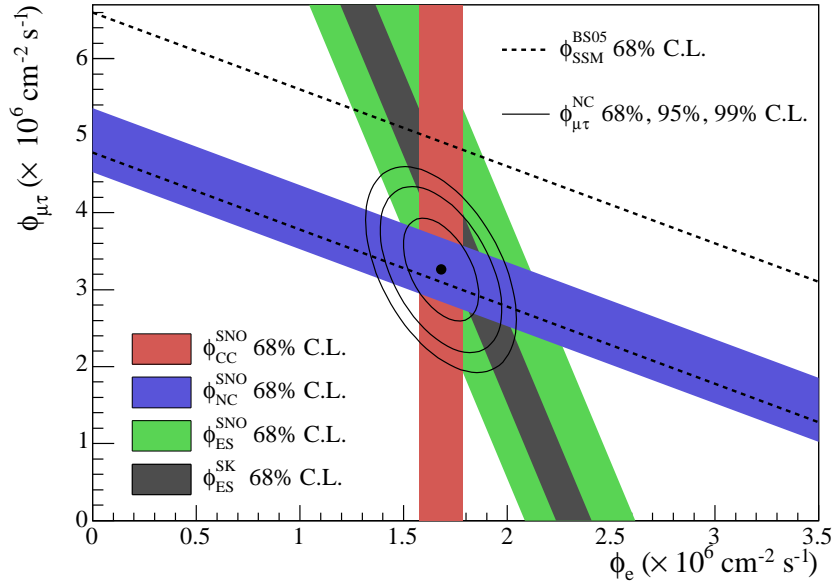


Figure 1.3: Solar neutrino fluxes  $\phi_{\mu\tau}$  versus  $\phi_e$  as measured by the SNO and Super-Kamiokande experiments. The dashed lines mark the neutrino flux predicted by the SSM. The flux  $\phi_e$  is given by the CC-flux (marked by a point and lines, that represent various confidence levels) and  $\phi_{\mu\tau}$  by the difference of the fluxes NC - CC. Figure taken from [A<sup>+</sup>05a]

$1\sigma$  uncertainties:

$$\tan^2(\Theta_{12}) = 0.45_{-0.08}^{+0.09} \quad \text{and} \quad \Delta m_{12}^2 = 6.5_{-2.3}^{+4.4} \cdot 10^{-5} \text{eV}^2 \quad (1.10)$$

Hence, the mixing angle  $\Theta_{12}$  is quite large, but not maximal.

**Reactor neutrinos** Fission reactors are a copious source of electron anti-neutrinos that are produced in the  $\beta$ -decays of neutron-rich nuclei. These electron anti-neutrinos are produced by the chain of  $\beta$ -decay of the fission products. A typical modern nuclear power plant has several reactor cores, each with a thermal power of the order of  $3\text{GW}_{th}$ . On average, each fission produces 200MeV with release of about  $6\bar{\nu}_e$ . That means the flux of electron neutrinos is about  $2 \cdot 10^{20} \text{s}^{-1}$  per  $\text{GW}_{th}$ . Although the anti-neutrino flux is very high, it is isotropic and decreases rapidly with distance. Fortunately, the released anti-neutrinos have a relatively low energy in the order of a few MeV, which implies a short oscillation length.

Reactor electron anti-neutrinos are detected through the *inverse neutron decay process* [GK07]:



This reaction was already used for the first detection of electron anti-neutrinos produced in the Savannah River power plant. The KamLAND experiment [E<sup>+</sup>03] used this reaction to observe the flux of electron anti-neutrinos from nearby reactors with an average distance of about 180km. For these distances, the transition probability mainly depends on  $\Theta_{12}$  and  $\Delta m_{12}^2$  as for short distances ( $< 5\text{km}$ ) the influence of  $\Theta_{12}$  and  $\Delta m_{12}^2$  is negligible and the transition probability is mainly dependent on  $\Theta_{13}$  and  $\Delta m_{13}^2$ . The experiment observed evidence for the disappearance of electron

anti-neutrinos. The analysis of the measured data yields [A<sup>+</sup>05c]:

$$\tan^2(\Theta_{12}) = 0.46 \quad \text{and} \quad \Delta m_{12}^2 = 7.9_{-0.5}^{+0.6} \cdot 10^{-5} \text{eV}^2 \quad (1.12)$$

These results can be combined with the SNO measurements of the solar neutrinos and then constrain the angle to [A<sup>+</sup>03]:

$$\tan^2(\Theta_{12}) = 0.40_{-0.07}^{+0.10} \quad (1.13)$$

The Double CHOOZ collaboration is planning to set up two detectors at short distances to a nuclear reactor. The experiment aims to measure  $\sin^2(2\Theta_{13})$  up to a sensitivity of  $\sin^2(2\Theta_{13}) < 0.03$  at 90% C.L [Las06].

**Accelerator neutrinos** The neutrino beams in accelerator experiments are produced through pion decay at flight, muon decay at rest and beam dump. These experiments are therefore sensitive to the oscillation of a muon- into a tau-neutrino, a fact that allows the determination of  $\Theta_{23}$  and  $\Delta m_{23}^2$  with these kind of experiments. In the Japanese K2K experiment an almost pure  $\nu_\mu$ -beam was sent over 250km from the KEK laboratory to the Super-Kamiokande detector. Under the assumption  $\sin^2(2\Theta_{12}) = 1$ , the experimental data yields a best-fit value of the mass difference of [A<sup>+</sup>05b]:

$$\Delta m_{23}^2 = 2.8 \cdot 10^{-3} \text{eV}^2 \quad (1.14)$$

Future experiments will have the primary objective to discover  $\nu_\mu \leftrightarrow \nu_e$  oscillations in these beams. Such a measurement would give information on the element  $U_{e3}$  of the neutrino mixing matrix in case of three-neutrino-mixing.

## 1.2.2 Conclusions

The theory of neutrino oscillations is currently being supported by the results of a wide selection of experiments. The oscillation parameters like the mixing angles or squared mass differences have been measured or restricted. In figure 1.4 a summary of the data presently available is shown. Still, some main issues remain unsolved:

- **Absolute mass scale** oscillation experiments are only sensitive to the squared mass differences. The absolute mass scale is still to be determined.
- **Mass hierarchy** It is not known, how the mass eigenstates of the neutrinos are ordered in respect to absolute mass. This could be hierarchical ( $m_1 < m_2 < m_3$ ) as well as inverted hierarchical ( $m_3 < m_2 < m_1$ ) or even degenerate ( $m_3 \approx m_2 \approx m_1$ ).

## 1.3 Direct measurements of neutrino mass

As we have seen in section 1.2, the results of neutrino oscillation experiments have recently proved that neutrinos are massive. Since these experiments give only information on the squared-mass-differences of the neutrino masses, it is currently known that there are at least two massive neutrinos. One with a mass larger than  $\Delta m_{21} \approx 9 \cdot 10^{-3} \text{eV}$  and another with a mass larger than  $\Delta m_{31} \approx 5 \cdot 10^{-2} \text{eV}$ . Any information about the absolute values of the neutrino masses has to be investigated with other methods.

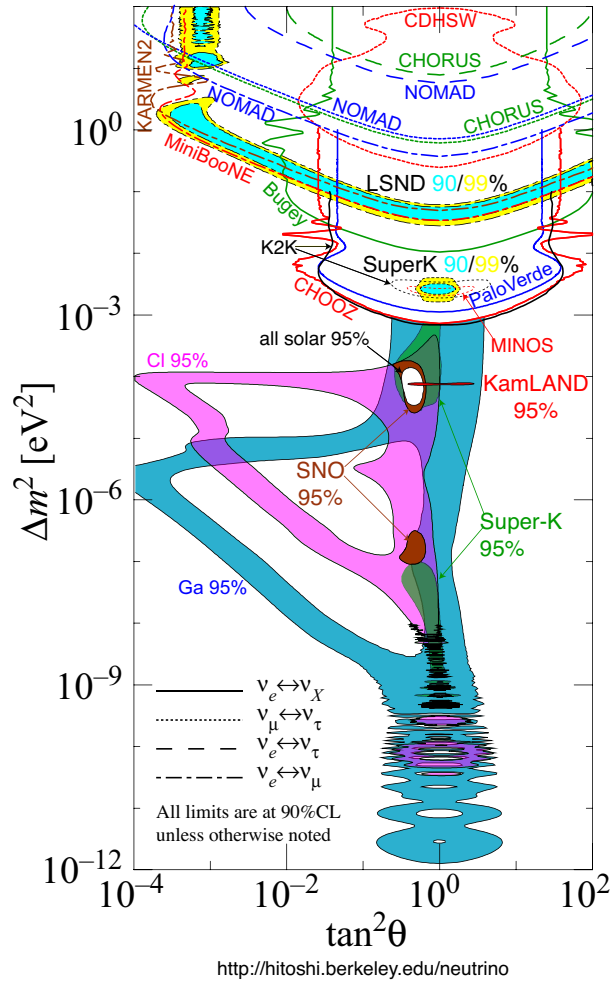


Figure 1.4: Some previous experiments have failed to detect neutrino oscillations due to their lack of sensitivity. However, this lack of signal can be interpreted as upper limit on the mass difference and the mixing angle between types of neutrinos. This plot of  $\Delta m^2$  as a function of  $\tan^2 \Theta$  shows the regions inside the lines that are excluded. The filled areas highlight the preferred values of  $\Delta m^2$  and  $\tan^2 \Theta$  measured in different experiments. Figure taken from [Mur08].

### 1.3.1 $\beta$ -decay

Today the most sensitive known method to measure the mass of the electron neutrino directly is by observing the electron energy spectrum in nuclear  $\beta$ -decay

$$\mathcal{N}(A, Z) \rightarrow \mathcal{N}(A, Z + 1) + e^- + \bar{\nu}_e \quad (1.15)$$

where  $A$  and  $Z$  are the mass and atomic numbers of the parent nucleus.

As described in equation (1.2) the electron neutrino, in general, does not have a definite mass, but is a mixture of massive neutrinos. However, traditionally the electron neutrino is treated as a superposition of mass eigenstates and the effects of neutrino mixing in nuclear  $\beta$ -decay are discussed separately.

One can introduce a step function into the spectrum, arguing that due to energy conservation, the total energy  $E_0$ , that is released in the decay must be at least equal to the sum of the rest energies of the particles generated in the decay.

$$\Theta(E_0 - m_e c^2 - m_{\bar{\nu}_e} c^2) \quad (1.16)$$

We use Fermi's Golden Rule to describe the transition probability  $T$  for the decay:

$$T \propto |\mathcal{M}|^2 \rho(E) \quad (1.17)$$

This means that the probability for the decay depends on the overlap between the initial- and final-state wave functions. In case of so called ‘‘allowed’’  $\beta$ -decays, the final-state wave functions of the electron and the anti-neutrino can be considered constant, as they are given by the nuclear matrix element  $|\mathcal{M}|^2$ . The density of the available final states  $\rho$  can be derived [Fer34]. We find a decay rate dependent on the electron energy  $E$  [Wei]:

$$\frac{d\dot{N}}{dE} = R(E)(E_0 - E)\sqrt{(E_0 - E)^2 - m_{\bar{\nu}_e}^2 c^4} \Theta(E_0 - E - m_{\bar{\nu}_e} c^2) \quad (1.18)$$

$R(E)$  is a product of factors, that are not relevant for the neutrino mass determination:

$$R(E) = \frac{G_F^2}{2\pi^3 \hbar^7} \cos^2 \theta_C |\mathcal{M}|^2 F(Z+1, E) p(E + m_e c^2), \quad (1.19)$$

where  $G_F$  is the Fermi coupling constant,  $\theta_C$  is the Cabibbo angle,  $\mathcal{M}$  is the nuclear matrix element,  $E$  and  $p$  are the electron kinetic energy and momentum.  $F(Z+1, E)$  is the Fermi function that describes the electromagnetic interaction of the produced electron with the final-state nucleus.

The figure of interest in equation (1.18) is of course  $m_{\bar{\nu}_e} c^2$ , which expresses the dependency of the spectrum on the neutrino mass. If this mass is not zero, the endpoint of the spectrum will shift to a lower energy whereas in regions with high count rates, the effect of the neutrino mass on the spectrum will be rather insignificant. This is plotted in figure 1.5.

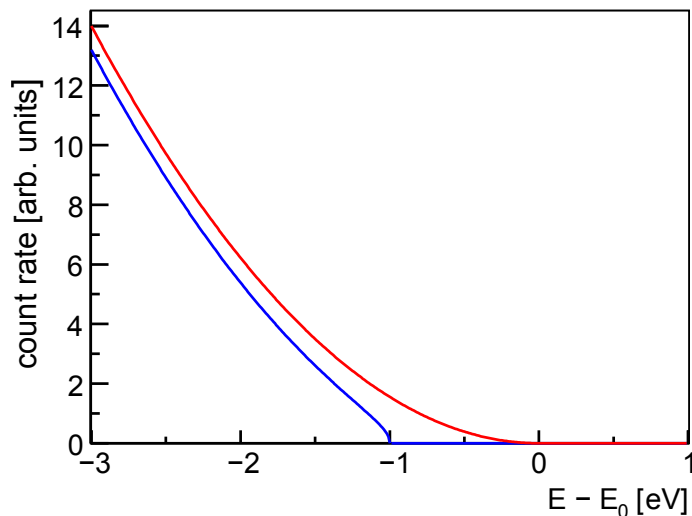


Figure 1.5: Spectra around the  $\beta$ -decay endpoint  $E - 0$  for 0 (red) and 1 eV (blue)  $\bar{\nu}_e$ -mass. Figure taken from [Höt09]

As mentioned before, we now want to take into account the effects of neutrino mixing. Therefore, we express the electron neutrino as a weighted superposition of the mass-eigenstates:

$$\nu_e = \sum_i U_{ei} \nu_i \quad (1.20)$$

Introducing this superposition into the decay spectrum gives us:

$$\frac{d\dot{N}}{dE} = R(E) \sum_i |U_{ei}|^2 (E_0 - E) \sqrt{(E_0 - E)^2 - m_i^2 c^4} \Theta(E_0 - E - m_i c^2) \quad (1.21)$$

This leads to fine structures in the spectrum, which, up to now, cannot be resolved in measurements due to the very small mass differences (see 1.2.1). So in current measurements only a weighted sum is observable:

$$m_{\nu_e}^2 = \sum_{i=1}^3 |U_{ei}|^2 m_{\nu_i}^2 \quad (1.22)$$

Most of the parameters of the spectrum described in (1.21) are well known. So in kinematic searches the data analysis turns out to be rather simple, as the only unknown quantities that have to be taken into account are the  $m_{\nu_e}$  and the endpoint energy  $E_0$ .

### 1.3.2 $\pi$ - and $\tau$ -decay

Another direct way to measure the neutrino mass experimentally are the pion- and tau-decays. The resulting experimental constraints are much less stringent than those obtained in  $\beta$ -decay experiments. Still these pion- and tau-decay experiments are historically interesting as they can be used to constrain the mixing of  $\nu_\mu$  and  $\nu_\tau$  with heavy neutrinos beyond three-neutrino mixing.

Measurements of the kinematics in the decay of charged pions can give information on the neutrino masses. The most sensitive experiment up to now was performed at PSI and has used the following decay:

$$\pi^+ \rightarrow \mu^+ + \nu_\mu. \quad (1.23)$$

Since this decay has a two-body final state, the mass of the neutrino can be determined by energy-momentum conservation if the momenta of the pion and muon can be measured with sufficient accuracy. In case of neutrino mixing, the muon neutrino is a superposition of different massive neutrinos. A measurement of the neutrino mass forces the superposition to collapse on the massive neutrino whose mass has been measured. Therefore, in analogy to (1.21), the decay rate must have peaks corresponding to the values of the neutrino masses, which are given by

$$m_i^2 = m_\pi^2 + m_\mu^2 - 2m_\pi \sqrt{m_\mu^2 + |\vec{p}_\mu|^2} \quad (i = 1, 2, 3) \quad (1.24)$$

for pions decaying at rest.

The value of the muon momentum measured in the PSI experiment is [A<sup>+</sup>96]:

$$|\vec{p}_\mu|^2 = 29.79200 \pm 0.00011 \text{MeV}^2 \quad (1.25)$$

leading to upper limits of  $m_i$  (at 90% C.L.)

$$m_i < 0.17 \text{MeV} \quad (i = 1, 2, 3) \quad (1.26)$$

The ALEPH experiment has used tau-decays for measurement of neutrino masses. The decays

$$\tau^- \rightarrow 2\pi^- + \pi^+ + \nu_\tau \quad \text{and} \quad \tau^- \rightarrow 3\pi^- + 2\pi^+ + \nu_\tau + \pi^0 \quad (1.27)$$

have been studied, with the result (at 95% C.L.) [B<sup>+</sup>98]:

$$m_i < 18.2 \text{ MeV} \quad (i = 1, 2, 3) \quad (1.28)$$

It is unlikely that in the future the measurements of neutrino masses with pion- and tau-decay experiments may improve so much to reach a precision at the eV level, comparable with  $\beta$ -decay experiments. As mentioned before, their interest lies mainly in the possibility of constraining the admixture of the muon and tau neutrinos with heavy neutrinos beyond three-neutrino mixing.

### 1.3.3 Neutrinoless double- $\beta$ -decay

Neutrinoless double- $\beta$ -decay experiments are considered as the best way to investigate the Majorana nature of neutrinos. In addition, such experiments offer the possibility of determination of the absolute neutrino mass scale and verification of the mass hierarchy of neutrinos.

The neutrinoless double- $\beta$ -decay processes of the types

$$\begin{aligned} \mathcal{N}(A, Z) &\rightarrow \mathcal{N}(A, Z + 2) + 2e^- \quad (2\beta_{0\nu}^-) \\ \mathcal{N}(A, Z) &\rightarrow \mathcal{N}(A, Z - 2) + 2e^+ \quad (2\beta_{0\nu}^+) \end{aligned} \quad (1.29)$$

are forbidden in the SM<sup>2</sup> if the neutrinos are Dirac particles. But they are possible if neutrinos are massive Majorana particles. In this case, a nucleus which can decay through a  $2\beta_{2\nu}$  process can also decay through a  $2\beta_{0\nu}$  process, albeit with a different lifetime.

The Heidelberg-Moscow experiment used a well shielded Germanium-counter to look for the double- $\beta$  decay of the isotope <sup>76</sup>Ge into <sup>76</sup>Se. Figure 1.6 shows the hypothetical spectrum of such a decay. After ten years of measurement, the data yields [KKDHK01]:

$$\tau_{2\nu} = 1.74 \pm 0.01_{-0.16}^{+0.18} \cdot 10^{21} a \quad \text{and} \quad \tau_{0\nu} = 1.5_{-0.7}^{+1.68} \cdot 10^{25} a \quad (1.30)$$

If these results can be confirmed by other experiments with higher statistics, it would in fact prove that neutrinos are massive Majorana particles. The estimated neutrino mass is:

$$\langle m_\nu \rangle = 0.39_{-0.34}^{+0.45} \text{ eV} \quad (1.31)$$

This mass lies in a scale accessible by  $\beta$ -decay experiments, so that it could be confirmed by experiments like KATRIN in the near future. Still one has to keep in mind the high model-dependence of these values: the complex Majorana phases that are used for the mass calculation are not known precisely, the elements of the nuclear transition matrix are not known with sufficient precision and there could be other theoretical explanations for the neutrinoless double  $\beta$ -decay than massive neutrinos, as for example super-symmetric particles or right-handed weak-couplings.

## 1.4 Indirect measurements of the neutrino mass

Cosmology offers several ways to indirectly determine the neutrino mass from various experimental data. However, most of them are only sensitive to the sum of the

---

<sup>2</sup>Standard Model

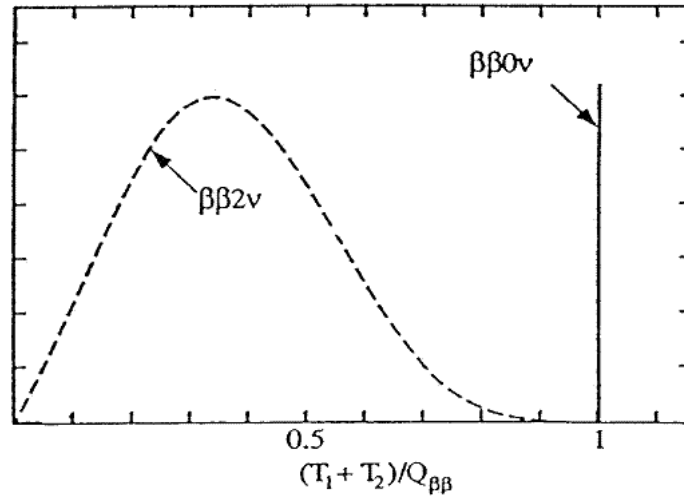


Figure 1.6: Energy spectrum of a double- $\beta$ -decay. The continuum stands for the summed energy of both charged leptons from the  $2\beta_{2\nu}$ -decay. The monoenergetic line at the total energy of the transition derives from the  $2\beta_{0\nu}$ -decay. Figure taken from [BSS]

masses of all neutrinos and the results are very model-specific [Han05].

When a supernovae transforms into a neutron star through the fusion of electrons and protons there are many neutrinos created. The time of flight of one neutrino to a detector on the Earth depends on its energy and mass. From the time difference between the detection of neutrinos from the same supernova and their measured energy an upper limit between 5.7 eV and 23 eV for the mass of the  $\nu_3$  can be derived. These values are very dependent on model-assumptions and the analysis-method [LL02], [KST87].

From the analysis of the structure of the cosmic microwave background radiation and a comparison with the estimated distribution of matter in the universe, an upper limit for the sum of all neutrino masses between 0.42 eV and 1.8 eV can be derived [Han05].



## 2. The KATRIN experiment

The goal of the KATRIN experiment [O<sup>+</sup>] is to determine the mass of the electron anti-neutrino by examining the shape of the tritium- $\beta$ -spectrum close to its endpoint. With approximately 1000 days of data-taking, the experiment will be able to achieve a mass determination down to 0.35 eV/c<sup>2</sup> ( $5\sigma$ ) or to set an upper limit of 0.2 eV/c<sup>2</sup> ( $3\sigma$ ) [Col04].

The following chapter will give a short introduction to the experiment, briefly describing the basic mechanics and its core components.

### 2.1 The tritium $\beta$ -decay

As KATRIN is built to perform an ultra-precise measurement of the kinematics of  $\beta$ -decay electrons, the  $\beta$ -source is of very special importance. For the KATRIN experiment, it was decided to use the hydrogen-isotope tritium (<sup>3</sup>H) because it has the following key advantages.

- **low endpoint energy** The  $\beta$ -spectrum of tritium has an endpoint-energy of 18.57 keV thus being the  $\beta$ -emitter with the second lowest energy of all possible candidates.
- **short half-life** Tritium is a rather short-lived isotope, having a half-life of only 12.3 a. This has the advantage that there is less source material needed in order to reach an adequate count rate and shortens the measurement time.
- **simple electron shell** The electron shell configurations of tritium and its daughter <sup>3</sup>He<sup>+</sup> are quite simple. This is also true for their molecular states. The atomic and molecular corrections and the corrections due to the interaction with the emitted electron can be precisely computed [DT08], [ReW83].
- **small inelastic scattering probability** As tritium has a low nuclear charge  $Z$  the probability for inelastic scattering of emitted  $\beta$ -decay electrons within the source will be small.
- **nuclear matrix element** The tritium  $\beta$ -decay is super-allowed as it is a transition between mirror nuclei. Thus the nuclear matrix elements are energy independent and no corrections from the nuclear transition matrix elements  $\mathcal{M}$  have to be taken into account.

An alternative to tritium would be  $^{187}\text{Rh}$ , which has the lowest endpoint energy (2.47 keV) of all known  $\beta$ -decay nuclei. The MARE experiment [Hal06] will use arrays of low temperature calorimeters to measure the Rhenium-187- $\beta$ -spectrum. It aims for a sensitivity comparable to the current  $m_{\nu_e}^2$ -limits set by the Mainz and Troitsk experiments. As this calorimetric approach offers scalability, they plan to reach a sub-eV sensitivity in the future.

## 2.2 Basic setup

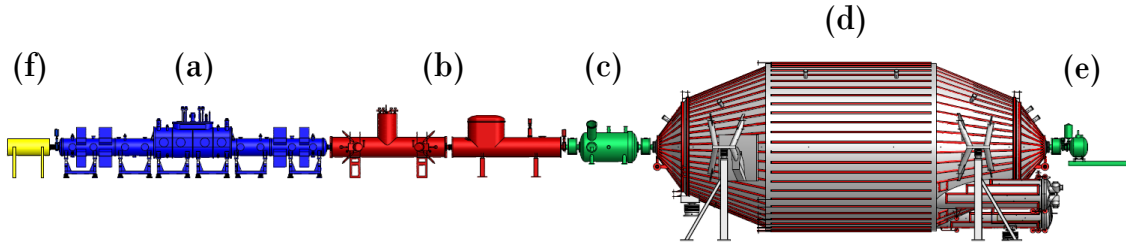


Figure 2.1: Overview of the KATRIN experimental setup, showing: the WGTS(a), the transport section(b), the pre-spectrometer(c), the main spectrometer(d), the detector(e) and the rear section(f).

### 2.2.1 WGTS

WGTS stands for **w**indowless **g**aseous **t**ritium **s**ource, which will be the source of  $\beta$ -electrons, analysed in the experiment. The ultra-cold (27 K) molecular tritium gas with high isotopic purity (>95%) will be injected into the middle of the 10 m long source tube and diffuses towards both ends. The inner tube has a diameter of 0.09 m and has two turbo-molecular pumps sitting at its ends to reduce the gas flow out of the WGTS. By controlling the temperature and the injection rate, the column density within the tube will be fixed to the reference value  $\rho d = 5 \cdot 10^{17}$  molecules/cm<sup>2</sup>, which grants optimal conditions with regard to both luminosity and scattering of  $\beta$ -electrons on residual gas molecules. In addition, the whole source tube is surrounded by superconducting solenoids that deploy a magnetic field strong enough (3.6 T) to guide the  $\beta$ -electrons out of the source towards the transport section.

### 2.2.2 Transport section

As the  $\beta$ -electrons from the source need to reach the spectrometers, the tritium gas from the source cannot be contained with physical barriers, hence why it is called “windowsless”. However, with respect to background reduction it is crucial that the tritium gas in the source must not get into the detector. Therefore, the gas flow from the source must be reduced by 14 orders of magnitude. For this purpose, there are two different pumping sections deployed between the source and the spectrometers. The **Differential Pumping Section** which houses turbo-molecular pumps to reduce the gas flow and the **Cryogenic Pumping Section**, in which the inner beam-tube is covered by argon-frost, to which residual gas molecules are frozen up. In addition, the beam-tube follows a zig-zag-pattern, that increases the efficiency of the residual gas removal. Similar to the WGTS, the electrons in the transport section are guided along a high magnetic field (up to 5.6 T) generated by superconducting solenoids.

### 2.2.3 Spectrometers

The  $\beta$ -electrons coming from the source will be analysed by a set of electrostatic retarding spectrometers of the MAC-E-Filter type. Only those electrons with large enough energy will pass this filter, while all others will be rejected. This will be addressed in detail in section 2.3

### 2.2.4 Detector

As the energy analysis is done by the spectrometers, the detector just needs to count the  $\beta$ -electrons that pass the main spectrometer. Nevertheless the detector still needs to have a good energy resolution in order to be able to discriminate between signal- and background-electrons. The detector has to meet some high requirements:

- low intrinsic background
- ability to operate in high magnetic fields
- sensitive to low count rates
- ability to cope with high rates during calibration phases
- spatial resolution, take into account the potential depression in the analysing plane

A silicon drift detector will be used with an aimed resolution of 600 eV for electron energies about 18.6 keV. Due to the low count rates that are expected at the very high energetic end of the spectrum, the detector must be well shielded to suppress external background. To achieve spatial resolution, the detector is segmented into 148 pixels, each of them covering a part of the flux tube with the same size (see figure 2.2).

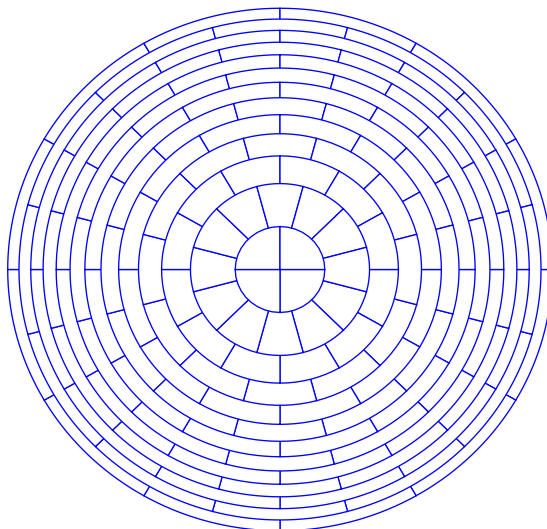


Figure 2.2: Sketch of the detector showing all 148 separated pixels.

## 2.3 MAC-E filter

Most of the information concerning the neutrino mass is contained in the region just below the energy endpoint  $E_0$ . But only a fraction  $10^{-12}$  to  $10^{-13}$  of all decays reside in the area of 1 eV below  $E_0$ . In order to achieve a significant count rate near the endpoint a spectrometer with a large angular acceptance and a good energy resolution at  $E_0$  is needed. The KATRIN spectrometers fulfil these requirements by implementing the principle of magnetic adiabatic collimation, and analysing the electron-energy with an electrostatic filter, or short: the MAC-E filter.

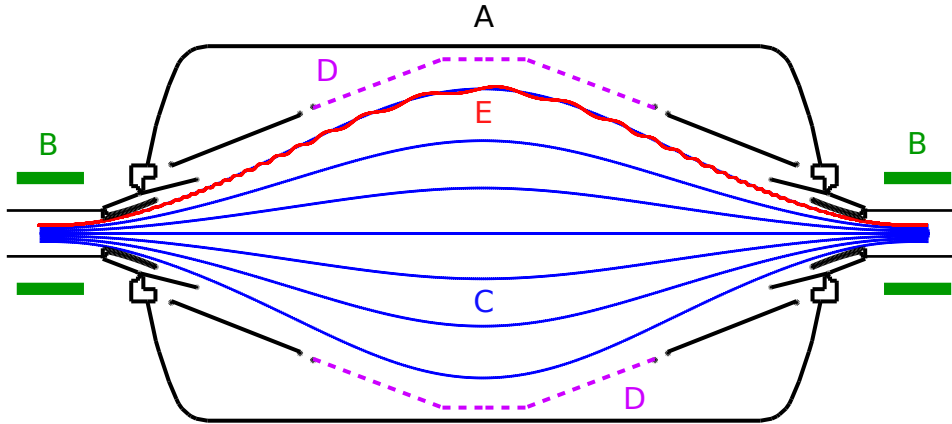


Figure 2.3: Sketch of the KATRIN-pre-spectrometer as an example for a MAC-E filter. It shows the spectrometer hull/massive electrodes (A), which are put on negative potential, the superconducting solenoids (B) and the inner wire-electrodes (D). In addition, magnetic field lines (C) and an exemplary electron-trajectory (E) are displayed.

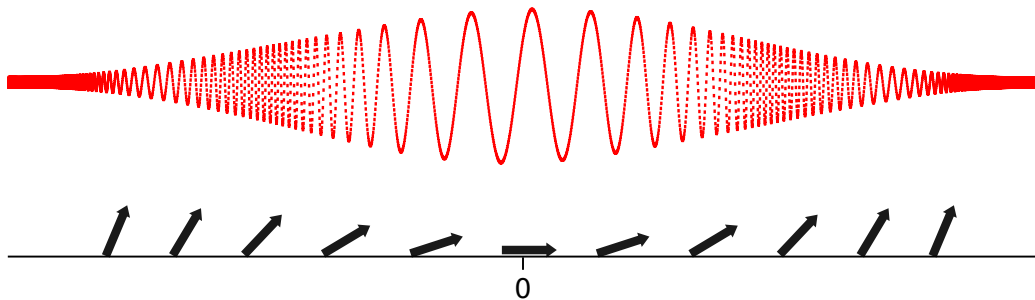


Figure 2.4: This figure shows an exaggerated cyclotron motion of an electron flying through the spectrometer. The arrows below indicate the momentum of the electron with respect to the magnetic field, neglecting the change of the momentum due to the electric field.

### 2.3.1 Principle

The MAC-E filter principle is based on the idea of adiabatic guidance of electrons on a cyclotron motion around magnetic field lines. As the strength of the magnetic field slowly decreases, the momentum of the electrons perpendicular to the magnetic field lines  $p_{\perp}$  is being transformed into the momentum parallel to the magnetic field

lines  $p_{\parallel}$ . At the position of minimal magnetic field strength  $B_{min}$  the electrostatic retarding potential reaches its maximum absolute value  $U_0$ . Merely electrons with a certain minimum parallel momentum  $p_{\parallel}$  and therefore, minimum parallel kinetic energy

$$E_{\parallel} > qU_0 \quad (2.1)$$

are able to pass this potential barrier. Hence the MAC-E filter acts as a so called high-pass filter and the measurements will deliver an integrated spectrum. Furthermore, the adiabatic guidance of electrons along the magnetic field-lines means that the electrons always move in the same flux-tube, with a constant magnetic flux. This flux-tube becomes larger as the magnetic field becomes weaker, therefore a MAC-E filter needs to have the largest radius in the area of the minimal magnetic field strength.

### 2.3.2 Characteristics

#### Adiabacity

In the non-relativistic approximation,  $E_{\perp}$  and  $E_{\parallel}$  can be expressed as follows:

$$\begin{aligned} E_{kin} &= \frac{p^2}{2m} = E_{\parallel} + E_{\perp}, \\ E_{\parallel} &= E_{kin} \cdot \cos^2 \Theta, \\ E_{\perp} &= E_{kin} \cdot \sin^2 \Theta. \end{aligned} \quad (2.2)$$

If the magnetic flux enclosed by the gyrating trajectory of the electron is constant, the motion is called adiabatic. Adiabatic electron motion is achieved, if the magnetic field along the cyclotron motion changes only slightly. As the magnetic field and electric potential vary, the cyclotron radius is resized, thus containing a constant flux. With the prerequisite of conserved enclosed magnetic flux the adiabatic invariant is defined as:

$$\Phi = \int \vec{B} d\vec{A} = const \quad \implies \quad Br_c^2 = const. \quad (2.3)$$

Another formulation for adiabatic motion is the conservation of the product of the absolute value of the orbital magnetic moment  $|\vec{\mu}|$  and the Lorentz-factor  $\gamma = \frac{1}{\sqrt{1-\frac{v^2}{c^2}}}$

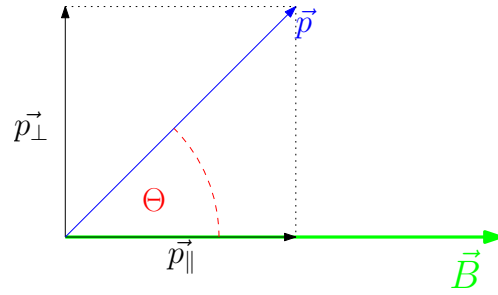
$$\gamma\mu = const. \quad (2.4)$$

In the tritium decay, the maximum occurring Lorentz-factor is 1.04, thus equation (2.4) can be approximated by only considering the magnetic moment:

$$\mu = \frac{E_{\perp}}{B} = const. \quad (2.5)$$

#### Energy resolution

As denoted in 2.3.1, the momentum and the kinetic energy of electrons performing a cyclotron motion along the magnetic fieldlines accordingly can be divided into a longitudinal component, parallel to the magnetic field lines ( $p_{\parallel}, E_{\parallel}$ ) and a transversal component, perpendicular to the magnetic field lines ( $p_{\perp}, E_{\perp}$ ). These components are defined by the polar angle  $\Theta$  between the momentum of the electron  $\vec{p}$  and the magnetic field at its position  $\vec{B}$  see figure 2.5. So this is the main condition, that

Figure 2.5: Definition of the angle  $\Theta$ .

a MAC-E filter has to fulfil. One can also derive from this an expression for the so called energy resolution  $\Delta E$  of a MAC-E filter. It is assumed that the motion is adiabatic and the electron has its maximum kinetic energy  $E_{kin,max}$  stored in the perpendicular component at the point with maximum magnetic field  $B_{max}$  ( $\Theta = 90^\circ$ ). Then the remaining energy  $\Delta E_\perp$  that is still stored in the perpendicular momentum at the point of minimum magnetic field  $B_{min}$  can be determined by the relation

$$\frac{E_{kin,max}}{B_{max}} = \frac{\Delta E_\perp}{B_{min}}. \quad (2.6)$$

Meaning that  $\Delta E_\perp$  cannot help to pass the potential barrier. For the KATRIN main spectrometer the maximum magnetic field strength is  $B_{max} = 6$  T at the pinch magnet. The minimum value  $B_{min} = 3 \cdot 10^{-4}$  T is present in the middle of the spectrometer, the so called *analysing plane*. With the tritium endpoint energy at approximately  $E_0 = 18600$  eV we get an energy resolution of:

$$\Delta E_\perp = \frac{B_{min}}{B_{max}} E_0 = \frac{3 \cdot 10^{-4} \text{ T}}{6 \text{ T}} \cdot 18600 \text{ eV} = 0.93 \text{ eV}. \quad (2.7)$$

The transversal energy is transformed into longitudinal energy, and simultaneously, the electric potential reduces the longitudinal energy. Therefore, the possible polar angle  $\Theta$  an electron has at the analysing plane ranges from  $0^\circ$  to  $90^\circ$ .

### Transmission function

One of the most important attributes of a MAC-E filter is its *transmission function*. It can be described as relative detected rate over kinetic surplus energy of the signal-electrons. Ideally this would be a step function, but as the spectrometer has a finite resolution it typically looks like the example shown in figure 2.6. To determine the transmission function of a MAC-E filter we have to investigate which initial conditions at the entrance of the spectrometer an electron has to fulfil in order to pass the filter. This is mainly defined by the relation between the initial transversal energy  $E_{\perp,start}$  of the electron (which can be expressed in terms of the initial angle  $\Theta_{start}$  with respect to the magnetic field) and the retarding potential  $U_0$  at the position where the electron will pass the filter. Following equation (2.1) only electrons that

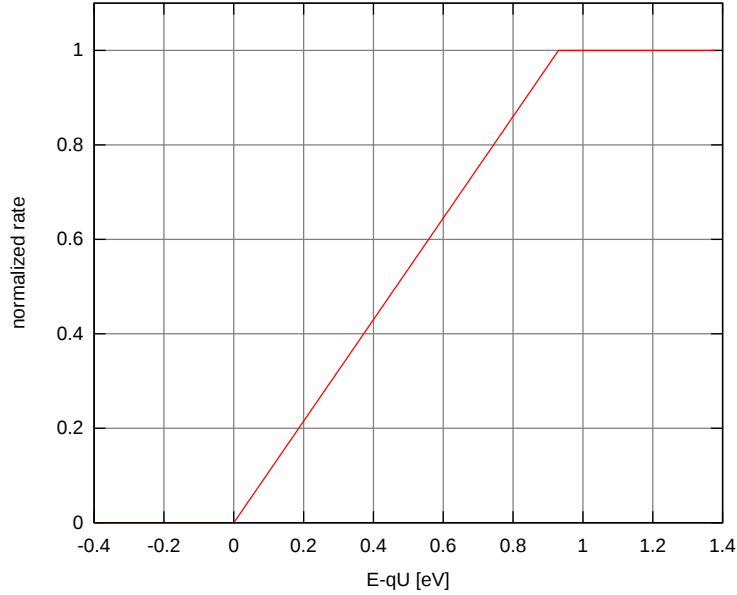


Figure 2.6: Theoretical transmission function of a MAC-E filter.

have enough longitudinal energy can pass the spectrometer:

$$\begin{aligned}
 E_{\parallel, B_{min}} > 0 &\implies E_{\parallel, B_{min}} = E_{kin, B_{min}} - E_{\perp, B_{min}} \\
 &= E_{kin, B_{min}} - E_{\perp, B_{start}} \frac{B_{min}}{B_{start}} \\
 &= E_{kin, B_{start}} - qU_0 - E_{kin, B_{start}} \sin^2 \Theta_{start} \frac{B_{min}}{B_{start}} \quad (2.8) \\
 &\implies qU_0 > E_{kin, B_{start}} \left( 1 - \sin^2 \Theta_{start} \frac{B_{min}}{B_{start}} \right).
 \end{aligned}$$

Where the indices *min* and *start* describe the conditions in the analysing plane and at the entrance of the filter respectively. Furthermore we can limit the maximum accepted  $\Theta$  of transmitted electrons to:

$$\implies \Theta_{start} \leq \arcsin \sqrt{\frac{E_{kin} - qU_0}{E_{kin}} \frac{B_{start}}{B_{min}}}. \quad (2.9)$$

So only electrons with an angle smaller than  $\Theta_{start}$  at the entrance of the filter are able to pass the potential barrier. With the fraction of electrons passing the filter compared to the overall electrons being sent through the filter the transmission function can be determined. From equation (2.9) we get the solid angle  $\Delta\Omega$ . Comparing  $\Delta\Omega$  with the maximal solid angle  $2\pi$  (forward direction) gives the fraction of electrons that are accepted by the filter:

$$\frac{\Delta\Omega}{2\pi} = 1 - \cos \Theta. \quad (2.10)$$

Combining these two equations we get the transmission function  $\mathcal{T}(E_{kin}, U_0)$  of the MAC-E filter:

$$\mathcal{T}(E_{kin}, U_0) = \begin{cases} 0 & \text{for } E_{kin} < qU_0 \\ 1 - \sqrt{1 - \frac{E_{kin} - qU_0}{E_{kin}} \frac{B_{start}}{B_{min}}} & \text{for } qU_0 \leq E_{kin} \leq \frac{qU_0}{1 - \frac{B_{min}}{B_{start}}} \\ 1 & \text{for } \frac{qU_0}{1 - \frac{B_{min}}{B_{start}}} \leq E_{kin} \end{cases} \quad (2.11)$$

In order to measure this transmission function, monoenergetic electron sources are employed. Because the kinetic energy of the electrons  $E_{kin}$  is constant, either the retarding potential  $U_0$  has to be varied or an additional, variable acceleration potential has to be applied to the source. One can also see from equation (2.11) that, in the case of a perfectly monoenergetic source, the width of the transmission function solely depends on the ratio  $\frac{B_{min}}{B_{start}}$  of the magnetic fields. The width increases if a source with an energy distribution of finite width is used. In this case the transmission function has to be convoluted with respect to the distribution.

Actually, we have to apply some corrections to the transmission function in order to reflect reality correctly. The maximum magnetic field in the KATRIN experiment is not deployed within the source. Therefore, some  $\beta$ -electrons will be reflected by the magnetic mirror effect before they reach the spectrometer. A particle is reflected, if, while moving from a region with lower magnetic field strength into a region with higher magnetic field strength, the polar angle exceeds a critical value:

$$\Theta_{crit} = \arcsin \sqrt{\frac{B_{start}}{B_{max}}} \quad (2.12)$$

where  $B_{start}$  is the magnetic field strength at the starting point. Taking this into account and with  $B_S$  being the magnetic field strength in the source, we can write down a modified transmission function:

$$\mathcal{T}'(E_{kin}, U_0) = \begin{cases} 0 & \text{for } E_{kin} < qU_0 \\ \frac{1 - \sqrt{1 - \frac{E_{kin} - qU_0}{E_{kin}} \frac{B_{start}}{B_{min}}}}{1 - \sqrt{1 - \frac{B_S}{B_{max}}}} & \text{for } qU_0 \leq E_{kin} \leq qU_0 \frac{B_{max}}{B_{max} - B_{min}} \\ 1 & \text{for } qU_0 \frac{B_{max}}{B_{max} - B_{min}} \leq E_{kin} \end{cases} \quad (2.13)$$

It is improbable that measurements will reproduce exactly this form of the transmission function. There are some additional factors for example, like detector and background effects, which modify the shape of this function.

### Electric potential depression

Usually, the electric potential across the analysing plane of a MAC-E filter is not homogeneous. This is called *potential depression*. As a result, the transmission condition of a signal electron depends on its radial distance to the filter's symmetry axis. Therefore, the detector of the KATRIN experiment is separated into 148 pixels (see section 2.2.4) to be able to determine the radial position of any detected electron. This data will then be taken into account for the analysis.

### Magnetic field depression

Analogously to the electric potential the magnetic field is not homogeneous in the analysing plane, a fact that leads to a radial dependence of the energy resolution. Within the main spectrometer, this deviation will be of the order of about 10%, in the pre-spectrometer about 25% of the maximum value.

## 2.3.3 KATRIN spectrometers

The KATRIN experiment features three different spectrometers of the MAC-E filter type, namely the pre- and main spectrometer, which will directly analyse the tritium- $\beta$ -decay spectrum, and the monitor spectrometer that is used to monitor

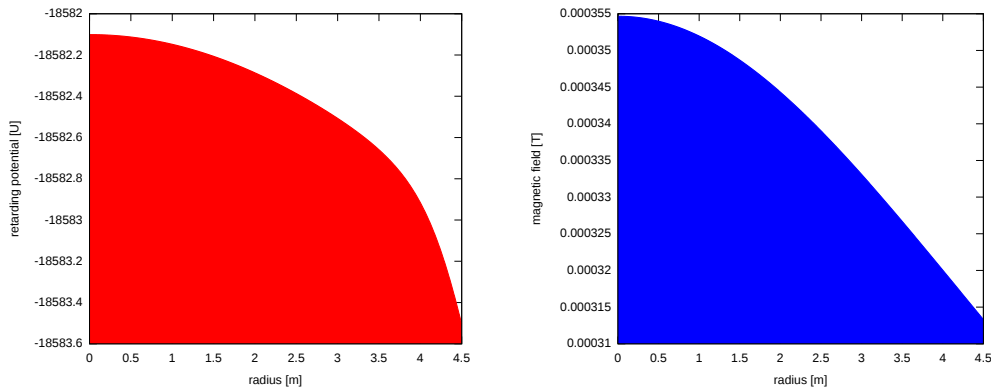


Figure 2.7: radial depression of the electric potential (left) and magnetic field (right) in the analysing plane of the KATRIN mainspectrometer

the stability of the main spectrometer retarding potential.

### Monitor spectrometer

In order to achieve the desired sensitivity for the neutrino mass of the KATRIN experiment, the retarding potential of the analysing spectrometer has to be known with a precision of 4 ppm at 18.6 kV. In order to control this, a real-time calibration experiment will be run in parallel, occupying the so called monitor spectrometer. This apparatus was already utilised in the Mainz Neutrino Mass Experiment to analyse the  $\beta$ -decay spectrum of a condensed tritium film and has been transferred to the KATRIN experimental site in late 2009. During operation, the spectrometer will be connected to the retarding potential of the main experiment, analysing nuclear electron sources and by this monitoring the potential with the help of well known nuclear standards.

### Pre-spectrometer

The pre-spectrometer is of importance for the KATRIN experiment during both, the conceptual phase and the actual measurements. It serves as a prototype for the main-spectrometer by investigating the vacuum concept including the heating- and cooling-system and by optimizing the electromagnetic design especially with respect to background. Later, during the tritium measurements the pre-spectrometer will serve as additional MAC-E filter, prior to the main spectrometer to reflect all electrons with energies  $E \lesssim E_0 - 300$  eV. This results in a reduction-factor of  $10^6$  for  $\beta$ -decay-electrons that reach the main spectrometer. The pre-spectrometer is 3.4 m long, has a diameter of 1.7 m and will be operated with a pressure of about  $10^{-11}$  mbar. It achieves an energy resolution of  $\Delta E \approx 100$  eV. It arrived at KIT in late 2003 and has been used for tests since then.

### Main spectrometer

The main MAC-E filter and thereby measuring tool of the KATRIN experiment is the main spectrometer. It is about 23 m long and has a inner radius of 4.5 m with a operating pressure below  $10^{-11}$  mbar. Similar to the pre-spectrometer, its vessel hull can be put on high voltage and it features an inner electrode system of wire electrodes for potential shaping and background reduction. Two superconducting solenoids are positioned at the ends of the spectrometer to provide the magnetic guiding field. Furthermore, the spectrometer is surrounded by a system of cable

loops, the so called the *aircoil system* which is responsible for fine-tuning the magnetic field shape and strength and compensation of magnetic stray fields. With a maximum magnetic field of 6 T within the superconducting coils and a minimum magnetic field of about 3 G in the analysing plane it features an energy resolution of  $\Delta E = 0.93$  eV.

### 2.3.4 Aircoil system

In regions of low magnetic field like in the analysing plane of the mainspectrometer, the Earth's magnetic field is not negligible and has a strong influence on the magnetic field inside the spectrometer. A hereby caused deformation of the flux-tube would lead to the loss of signal electrons and, at the same time, imply a rigorous increase of background electrons that are guided from the wall towards the detector (see figure 2.8). To avoid such a distortion, the KATRIN mainspectrometer features a so called aircoil system consisting of the **E**arth's **M**agnetic field **C**ompensation **S**ystem (EMCS) and the **L**ow **F**ield **C**orrection **S**ystem (LFCS). The EMCS will compensate the vertical and horizontal, non-axisymmetric component of the Earth's magnetic field. It consists of 16 vertical and 10 horizontal cosine coils. To have the fluxtube fit into the mainspectrometer at the analysing plane the LFCS will apply a magnetic field additionally to the superconducting solenoids sitting at the connection ports(see figure 2.8). The LFCS consists of 15 large coils, whose rotational symmetry axis is the beamtube. Having them run with individually up to 1500 Ampere-turns, they assure the desired flux-tube form that fits into the spectrometer. For more information see [GMO<sup>+</sup>09].

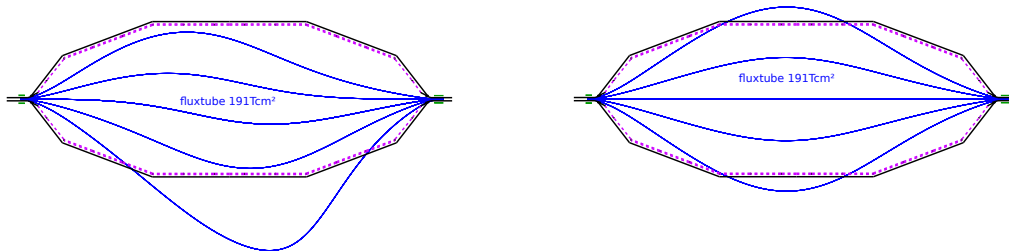


Figure 2.8: Sketch of the mainspectrometer without any magnetic field compensation (left) and with the EMCS compensating the Earth's magnetic field (right).

### 2.3.5 Background

Predecessor experiments have shown that there are several non negligible mechanisms that can lead to the creation of background-electrons within a MAC-E filter:

- **ionisation of residual gas**, through either signal electrons or
- **particles stored in penning traps and the magnetic bottle of the filter**, and
- **electrons emitted from the vessel hull.**

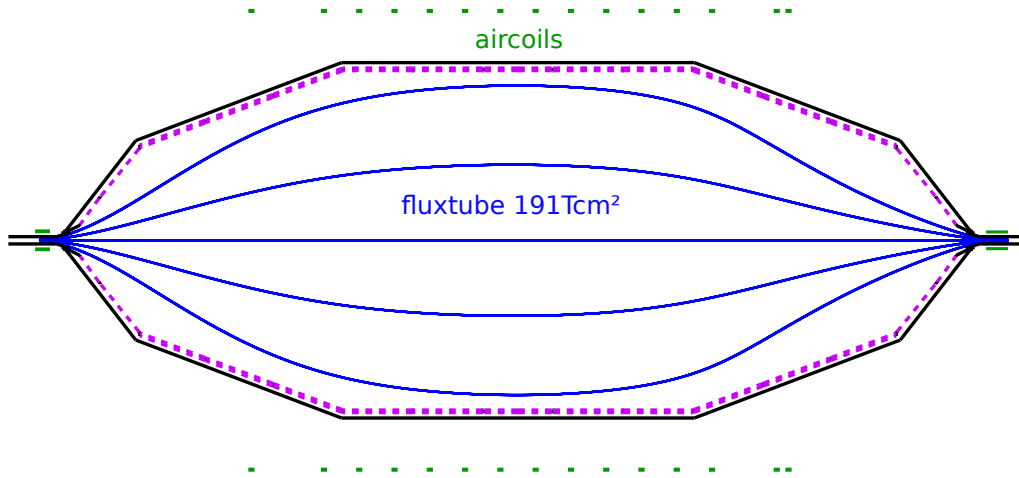


Figure 2.9: Sketch of the mainspectrometer with both, EMCS and LFCS installed. It is clearly visible that the flux-tube then fits into the spectrometer.

The ionisation of residual gas will be suppressed due to the very low operating pressure of  $10^{-11}$  mbar or less inside the spectrometer vessels. This has already been tested by predecessor experiments and test measurements at the pre-spectrometer. Penning traps are created in areas with an axial magnetic field and a minimum in the electrostatic potential. If there is a flaw in the electrode designed, there are several penning traps existent within a MAC-E filter. The particles stored within the traps can cause enormous background through ionisation of residual gas by electrons and photons, coming from photo-emission out of the traps. To prevent this, one must be very careful when designing the electrodes and must pay special attention to avoid formation of penning traps.

High energetic particles that get into the filter can be stored through the magnetic mirror effect. In order to remove them from the spectrometers, there is the possibility to apply an electric dipole field that guides those particles to the vessel walls or out of it.

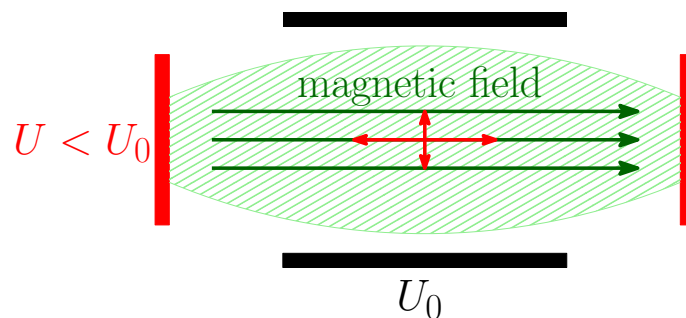


Figure 2.10: Sketch showing the principle of a penning trap: The magnetic field constrains the particle vertically, whereas the potential minimum constrains it horizontally

Electrons emitted from the vessel hull could be induced by cosmic rays, environmental radiation, intrinsic radioactivity or field-emission due to flawed electrode design. The last mentioned cause is easily avoided but it is impossible to shield the mainspectrometer from outside radiation. Therefore a mechanism is needed, that prevents background electrons, emitted from the vessel hull, from getting into the flux tube

that is mapped on the detector. Basically, this is done through compensation of non axially symmetric magnetic fields, like for example the earth's magnetic field, to achieve a so called magnetic shielding that prevents radial drift of background-electrons into the reference fluxtube. In addition, the inner wire electrode system consists of two layers that are put on slightly more negative potential than the hull, leading to a acceleration of the background-electrons back towards the vessel hull (see figure 2.11).

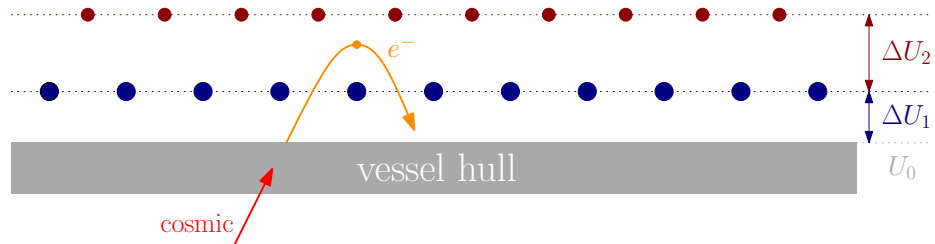


Figure 2.11: Working principle of the wire electrodes.

## 3. Methods for electric and magnetic field-calculation

The ability to calculate electric and magnetic fields, generated by all kinds of geometries and bodies is very important for an experiment whose main components are based on an exact interplay of the very same. Field-simulation-tools are important for electro-magnetic design calculations as well as for investigations of a wide spectrum of difficulties in connection with the trajectories of charged particles, as for example, investigations of penning traps or simulations of transmission functions. Most of the methods presented in this chapter were originally developed and implemented in C-code by Dr. Ferenc Glück [Glü06] at the KIT. The existing code has been rewritten, restructured and improved in the context of this diploma thesis and was brought into an object oriented shape using C++. An implementation of the line-segment and interpolation methods did not exist before, they were newly written.

### 3.1 Magnetic field calculation

The magnetic fields in the KATRIN experiment are of special interest, as they do both, guide the electrons through the experiment and grant an adiabatic transformation of the electron-momentum in the spectrometers. Depending on the generating component, there are several ways to calculate the resulting magnetic field: the *line-segment* methods are able to emulate complex forms by composing them of numerous small lines, thus being flexible but slow. In contrast to them, the *Legendre polynomial* methods are very fast, but need pre-calculations and are only applicable to axisymmetric coils. This section will give an introduction to these methods, explaining the physical and mathematical principles they are based on.

#### 3.1.1 Line-segment discretization methods

Usually, when simulating an existing, real experimental configuration, one reaches the point where the field-generating components can no longer be seen as simple geometric shapes. Nevertheless, the common way to simulate them is to approximate

their real geometric shape with line-segments. This method is very popular, because it offers the opportunity to scale the discretization of the emulated object. The user can choose either an inaccurate model that is fast to compute, or a very accurate model, thus taking a lot of computation time.

### 3.1.1.1 Integrated Biot-Savart

In the KATRIN experiment, there are a few components, generating magnetic fields that have a relatively simple shape, consisting of just a conductor that is shaped or wound in a distinct way. There are for example the components of the air coil system (see also 2.3.4): the EMCS, that consists of several cosine coils and the LFCS that features some non-circular coils. Further applications will also include calculating the magnetic field of the dipole coils in the DPS1-R, DPS1-F and the rear section. To compute their effects on the magnetic field in the experiment the integrated Biot-Savart method is used.

The magnetic field that is generated by any current-carrying component can be described using Biot-Savart's law: From an infinitely long conductor segment with current  $I$ , an infinitesimally small segment  $d\vec{l}$  in direction of the current generates at the position  $\vec{r}$  the magnetic field:

$$d\vec{B} = \frac{\mu_0}{4\pi} \frac{I d\vec{l} \times \hat{r}}{r^2}. \quad (3.1)$$

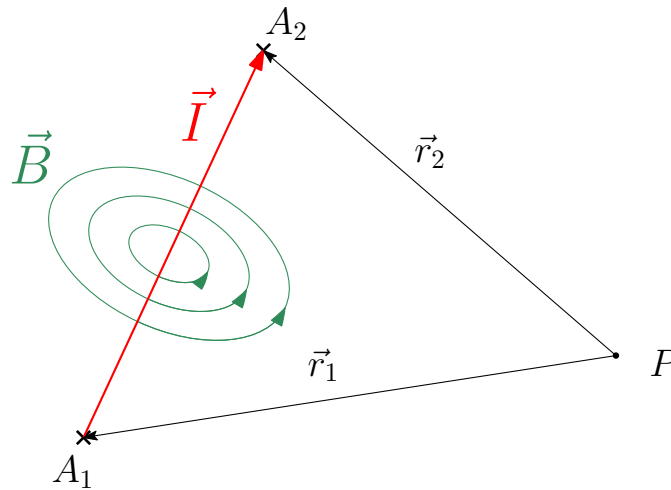


Figure 3.1: A line-current-segment is defined by a start point  $A_1$ , an endpoint  $A_2$  and the magnitude of the current  $I$  that flows from  $A_1$  to  $A_2$ .

As we want to discretize our objects down to finite line-current segments, similar to the one shown in figure 3.1, we integrate along a line current segment and get:

$$\begin{aligned} \vec{B}_i &= \frac{\mu_0}{4\pi} d\vec{L} \times \vec{I} \quad \text{with} \\ d\vec{L} &= \left( \frac{\hat{r}_1 + \hat{r}_2}{R + l} - \frac{\hat{r}_1 + \hat{r}_2}{R - l} \right), \\ R &= |\vec{r}_1| + |\vec{r}_2|, \quad l = |\vec{r}_2 - \vec{r}_1| \quad \text{and} \quad \hat{r}_i = \frac{\vec{r}_i}{|\vec{r}_i|}. \end{aligned} \quad (3.2)$$

Being able to use the superposition principle, it is possible to approximate complex shapes by numerous line-current-segments and simply sum up their individual field contributions  $\vec{B}_i$  to get the overall resulting magnetic field:

$$\vec{B}_{total} = \sum_{i=1}^N \vec{B}_i \quad (3.3)$$

Geometries composed of such line current segments can easily be tested by checking the validity of the Maxwell-equations. If, for example, the curl of the magnetic field  $\vec{\nabla} \times \vec{B}_{total}$  is non-zero in vacuum, this is a hint that a current loop is not closed and that you should check your discretization.

### 3.1.1.2 Magnetic dipole-bars

Today's buildings consist mainly of concrete and ferro-magnetic steel. Unfortunately so does the hall where the KATRIN experiment is housed. The steel rods inside the floor and the walls cause non-negligible, highly inhomogeneous magnetic stray-fields. As people have already foreseen that during the planning of the experiment, the KATRIN-hall was partially built with stainless steel that has a by far decreased magnetisation. However, there remains a strong magnetic component caused by the magnetic materials in the walls of the KATRIN-hall.

Fortunately, it is known how the obstructed steel bars are magnetized: namely along their symmetry axis. In this case, one can make the simplifying approximation of a magnetic dipole with two magnetic charges  $Q$  at both ends of the bar (see figure 3.2).

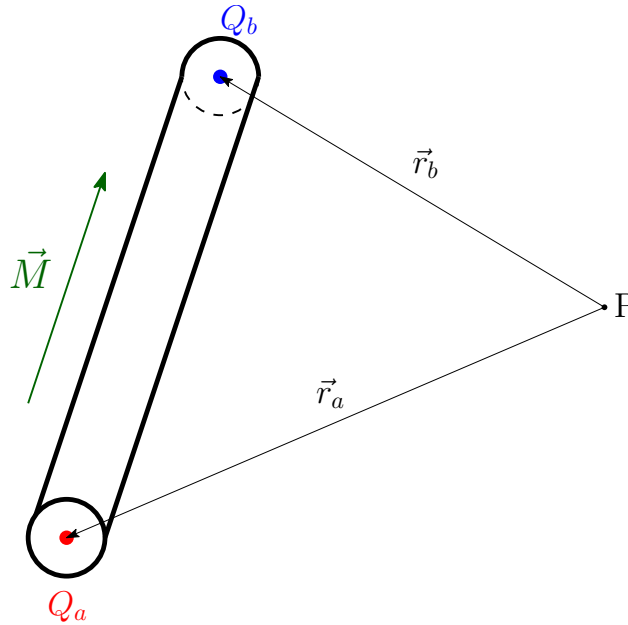


Figure 3.2: The magnetic-dipole-bars are characterised by two magnetic charges at the ends of the bar, their distance and the radius of the bar.

The magnetic field of such a dipole can be easily calculated analogue to Coulomb's law:

$$\vec{B}_i(P) = -Q \frac{\mu_0}{4\pi} \left( \frac{\vec{r}_a}{|\vec{r}_a|^3} + \frac{\vec{r}_b}{|\vec{r}_b|^3} \right) \quad \text{with} \quad Q = |\vec{M}| \cdot \pi r^2 \quad (3.4)$$

$\vec{M}$  denotes the magnetisation and  $r$  the radius of the dipole-bar. Again, to get the total magnetic field from all dipole-bars their contributions  $B_i$  have to be summed up. However, as the steel in the buildings is enclosed by concrete and thereby not accessible for direct measurements of the magnetization, it is quite complicated to build a model to describe them them [Rei10]. In order to get an appropriate model, many magnetic field measurements near the walls of the KATRIN hall are necessary. With this data and an assumed distribution of the steel bars in the wall, one can post a set of linear equations. The solution of these linear equations leads to a good model for the magnetisation which enables us to calculate the magnetic field due to magnetic materials in the KATRIN hall.

### 3.1.2 Legendre polynomial expansion

#### 3.1.2.1 Elliptic Integrals

The main components generating magnetic fields in the KATRIN experiment are circular coils and superconducting solenoids. These are simple circular current loops, that have a rotational symmetry axis (compare fig. 3.3).

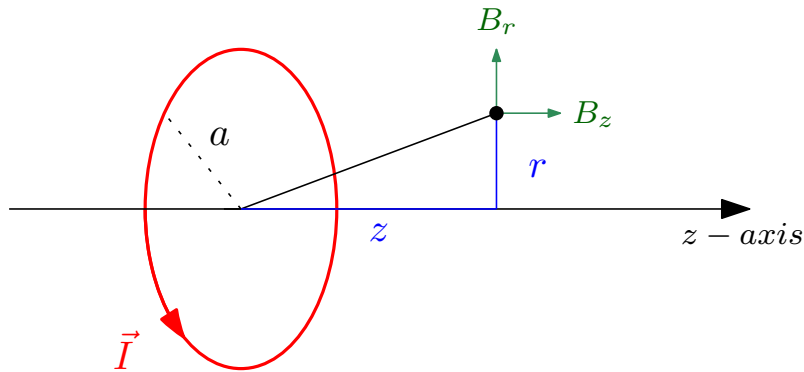


Figure 3.3: A loop with the radius  $a$  and the current  $\vec{I}$  running through it, induces a magnetic field  $\vec{B}$

The Biot-Savart law (3.1) for a thin coil can be expressed in terms of the complete elliptic integrals:

$$K(k) = \int_0^{\frac{\pi}{2}} \frac{d\varphi}{\sqrt{1 - k^2 \sin^2 \varphi}} \quad (\text{I})$$

$$E(k) = \int_0^{\frac{\pi}{2}} d\varphi \sqrt{1 - k^2 \sin^2 \varphi} \quad (\text{II}) \quad (3.5)$$

$$\Pi(c, k) = \int_0^{\frac{\pi}{2}} \frac{d\varphi}{(1 - c^2 \sin^2 \varphi) \sqrt{1 - k^2 \sin^2 \varphi}} \quad (\text{III})$$

They can be used for an analytical computation of the magnetic field [Jac98]:

$$\begin{aligned}
B_r &= \frac{I}{c} \frac{2z}{r\sqrt{(a+r)^2+z^2}} \left[ -K(k) + \frac{a^2+r^2+z^2}{(a+r)^2+z^2} E(k) \right] \\
B_\varphi &= 0 \\
B_z &= \frac{I}{c} \frac{2}{r\sqrt{(a+r)^2+z^2}} \left[ K(k) + \frac{a^2-r^2-z^2}{(a+r)^2+z^2} E(k) \right]
\end{aligned} \tag{3.6}$$

where  $k^2 = \frac{4ar}{z^2+(a+r)^2}$ . For real coils, with a finite length, the third integral is also needed for a description of the magnetic field. Usually,  $K(k)$ ,  $E(k)$  and  $\Pi(c, k)$  are expressed via Carlson's elliptic integrals  $R_F$ ,  $R_J$ ,  $R_D$  [PTVF07]:

$$\begin{aligned}
K(k) &= (R_F, 0, 1 - k^2, 1) \\
E(k) &= (R_F, 0, 1 - k^2, 1) - k^2 \frac{1}{3} (R_D, 0, 1 - k^2, 1) \\
\Pi(c, k) &= (R_F, 0, 1 - k^2, 1) - c^2 \frac{1}{3} (R_J, 0, 1 - k^2, 1, 1 - c^2)
\end{aligned} \tag{3.7}$$

These solutions are valid everywhere and hence, the magnetic field can even be calculated inside the coils. In addition, Carlson's elliptic integrals offer a relatively fast numerical computation method. But still a numerical integration is necessary, which usually means summing over many numbers. To speed things up, a solution has to be found that is fast to compute: the zonal-harmonics are appropriate solutions for axisymmetric coils. They can be computed fast and offer a variable precision, depending on the number of expansion orders that are considered.

### 3.1.2.2 Zonal Harmonic Expansion

The magnetic field at a point  $\vec{p}(r, z)$  close to the symmetry axis, can be expressed in terms of the Legendre polynomial expansion and its derivatives at the point  $z_0$  that lies on the symmetry axis, a so called sourcepoint. In case the distance of the field-point to the sourcepoint is smaller than the minimal distance of the sourcepoint to the coil body ( $\rho < \rho_{cen}$ , see fig. 3.4), the magnetic field is given by the so called central expansion:

$$\begin{aligned}
B_r &= -s \sum_{n=1}^{\infty} \frac{B_n^{cen}}{n+1} \left( \frac{\rho}{\rho_{cen}} \right)^n P'_n(u) \\
B_\varphi &= 0 \\
B_z &= \sum_{n=0}^{\infty} B_n^{cen} \left( \frac{\rho}{\rho_{cen}} \right)^n P_n(u)
\end{aligned} \tag{3.8}$$

with  $u = \cos \theta$  and  $s = \sin \theta$

with  $B_n^{cen}$  being the central source coefficients and  $P_n$  the Legendre polynomials. The minimal distance between the sourcepoint and the coil  $\rho_{cen}$  is usually called central convergence radius and equation (3.8) is only valid within.

As we want to know the magnetic field outside of the convergence radius too, a second polynomial expansion has to be introduced. This remote expansion is only valid for distances to the sourcepoint greater than the remote convergence radius

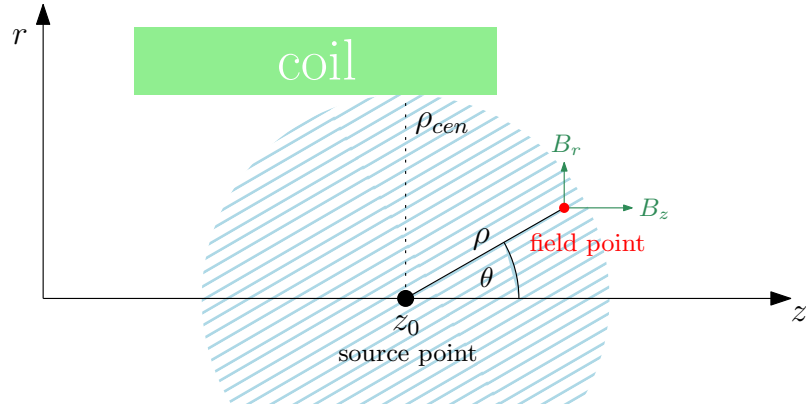


Figure 3.4: Convergence radius of the central expansion.

$\rho_{rem}$ , which is the maximal distance of the sourcepoint to the coil ( $\rho > \rho_{rem}$ , see fig. 3.5). The magnetic field is then defined by the remote expansion:

$$\begin{aligned} B_r &= s \sum_{n=2}^{\infty} \frac{B_n^{rem}}{n} \left( \frac{\rho_{rem}}{\rho} \right)^{n+1} P'_n(u) \\ B_\varphi &= 0 \\ B_z &= \sum_{n=2}^{\infty} B_n^{rem} \left( \frac{\rho_{rem}}{\rho} \right)^{n+1} P_n(u) \end{aligned} \quad (3.9)$$

with  $B_n^{rem}$  being the remote source coefficients.

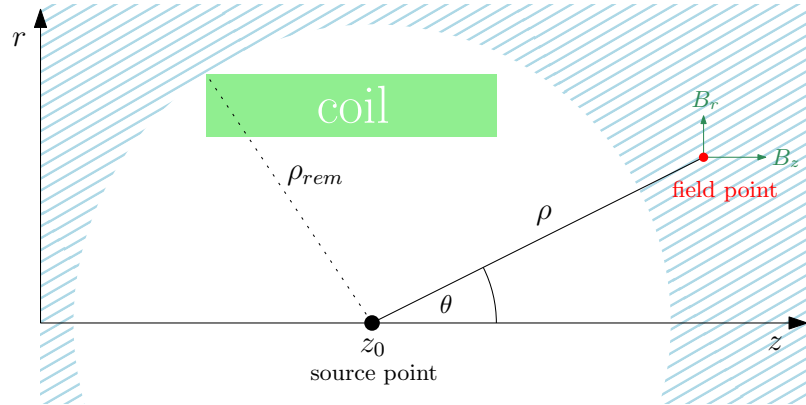


Figure 3.5: Convergence radius of the remote expansion.

These expansions now allow a very fast field-computation nearly everywhere in the system. They are not valid close to and inside the coils, so elliptic integrals have to be used here.

### 3.1.2.3 Application

For the description of a system of multiple coils, the convergence radii are determined by the closest, respectively the most remote coil (see fig. 3.6). To cover a larger area the amount of sourcepoints can simply be increased as shown in figure 3.7. Another benefit of having several sourcepoints is a faster computation, as the polynomial expansion converges faster if the fractions  $\frac{\rho}{\rho_{cen}}$  and  $\frac{\rho_{rem}}{\rho}$  are smaller. By choosing

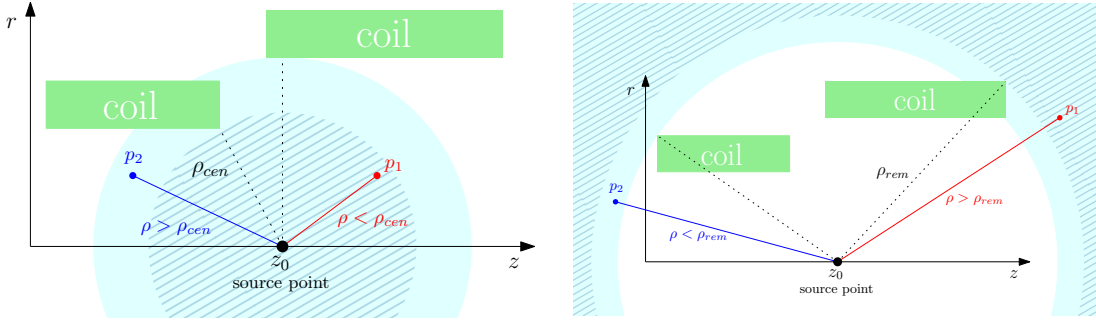


Figure 3.6: Central convergence radius (top) and remote convergence radius (below), with two coils using only one sourcepoint. The expansions converge in  $p_1$  but not in  $p_2$ .

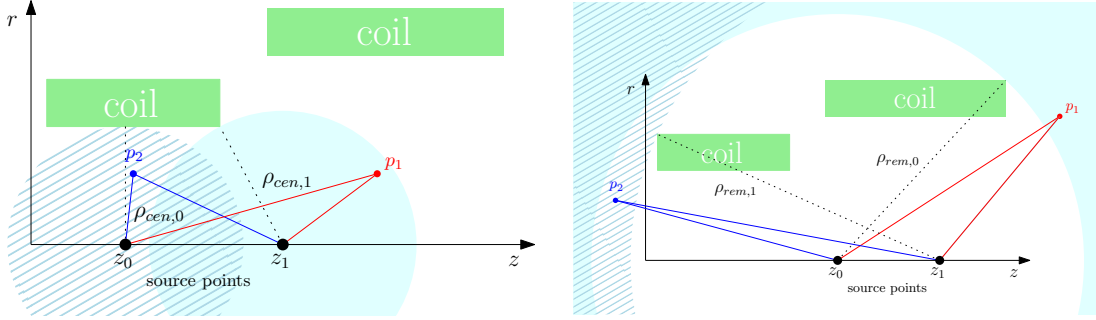


Figure 3.7: With the additional sourcepoints, it is now possible to compute the magnetic field in both  $p_1$  and  $p_2$  with the polynomial expansion.

the sourcepoint with the smallest fraction for the field point to be calculated, a lot of computation time can be saved.

In preparation for the polynomial expansion, the source coefficients  $B_n^{cen}$  and  $B_n^{rem}$  need to be computed at every sourcepoint. They can be expressed in two dimensional integrals over the coil profile:

$$B_n^{cen} = \int_{R_{min}}^{R_{max}} dR \int_{Z_{min}}^{Z_{max}} dZ b_n(R, Z) \quad \text{and} \quad (3.10)$$

$$B_n^{rem} = \int_{R_{min}}^{R_{max}} dR \int_{Z_{min}}^{Z_{max}} dZ b_n^*(R, Z),$$

with

$$b_n(R, Z) = \frac{\mu_0 I}{2A\rho_{cen}} \left( 1 - \left( \frac{Z - z_0}{\rho_{ZR}} \right)^2 \right) \left( \frac{\rho_{cen}}{\rho_{ZR}} \right)^{n+1} P'_{n+1} \left( \frac{Z - z_0}{\rho_{ZR}} \right), \quad (3.11)$$

$$b_n^*(R, Z) = \frac{\mu_0 I}{2A\rho_{rem}} \left( 1 - \left( \frac{Z - z_0}{\rho_{ZR}} \right)^2 \right) \left( \frac{\rho_{rem}}{\rho_{ZR}} \right)^n P'_{n-1} \left( \frac{Z - z_0}{\rho_{ZR}} \right),$$

$\rho_{ZR}$  being the distance between the sourcepoint  $z_0$  and the point  $(Z, R)$  in the coil body and  $\frac{I}{A}$  being the current density within the coil.

It is even possible to compute the field of multiple coils that do not have a common symmetry axis. In this case, the coils can be merged into groups with common symmetry axes (see fig. 3.8). The source coefficients are computed for the sourcepoints in the respective coordinate system. Afterwards the magnetic field is transformed back into the reference system.

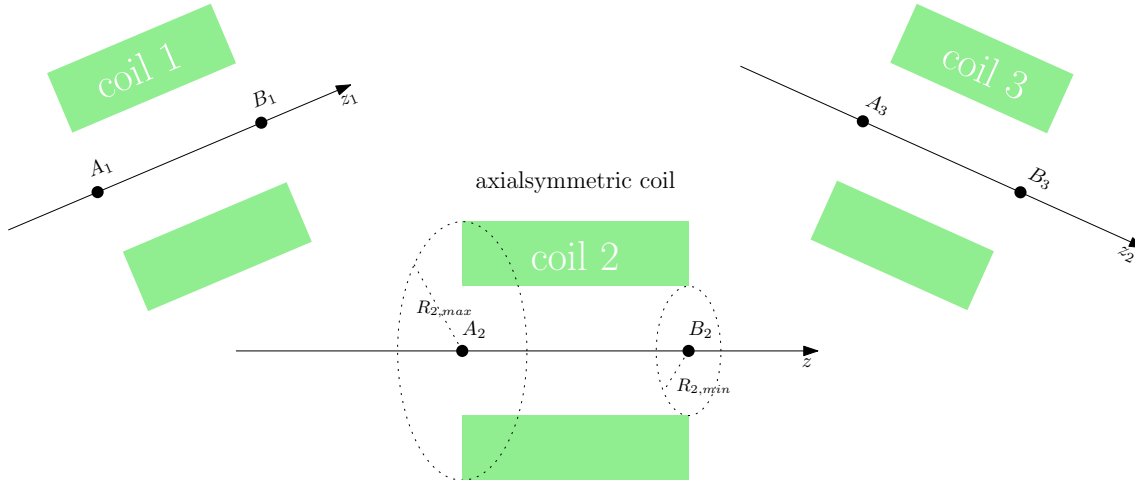


Figure 3.8: Tilted coils with different symmetry axes

## 3.2 Electric field calculation

Electric field and potential calculations turn out to be more complicated than the magnetic ones. Magnetic fields are caused by electric current, a quantity which can be directly measured and set. The electric field and potential, however, are caused by a charge distribution that is usually not known. The quantity you can set and measure on your electrodes is the voltage. The charge density on the electrodes is dependent on the voltage, but also highly dependent on the geometry of the electrode itself and on its surrounding. Another KATRIN-specific requirement is the ability to handle large volumes enclosed by electrodes. Most of the methods used to simulate electric fields, like for example the Finite Difference Method, are not applicable in such a case, as they divide the volume into a close-meshed grid, which, for extended geometries, can not be handled without serious problems regarding computer memory.

Actually, a method exists that meets these requirements, the so called **Boundary Element Method**.

### 3.2.1 Boundary element method

Working with the boundary element method (BEM), it is assumed that on a given surface-part of the electrode the charge density is distributed homogeneously and the resulting electric field can be derived from it. Analogous to the line-segment methods discussed earlier in this chapter, the discretization into surface elements offers the ability to form any complex shape out of such elements with variable level of detail and thereby accuracy.

An electrode can be discretized into  $N$  sub-elements  $S_j$ . The geometry  $S$  can be written as a sum of these sub-elements:

$$S = \sum_{j=1}^N S_j \quad (3.12)$$

Integrating over the charge densities  $\sigma$  of all subelements, we get the potential at the position  $\vec{r}$  caused by the geometry  $S$  [HK89]:

$$\Phi(\vec{r}) = \frac{1}{4\pi\epsilon_0} \int_S \frac{\sigma(\vec{r}_S)}{|\vec{r} - \vec{r}_S|} d^2\vec{r}_S \quad (3.13)$$

Although they are assumed to be constant within one subelement, the charge densities are usually not known. The quantities that are known are the voltages  $U_i$ , applied to the electrodes. It is possible to write down an equation system, relating the charge densities  $\sigma_j$  with the voltage of the subelements  $U_i$ :

$$U_i = \sum_{j=1}^N C_{ij}(\vec{r})\sigma_j, \quad (3.14)$$

with  $C_{ij} = C_j(\vec{r}_i)$  the so called Coulomb-matrix-element. It can be seen as the electric potential at the midpoint of subelement  $i$  caused by subelement  $j$ . It is a geometrical factor given by:

$$C_j(\vec{r}_i) = \frac{1}{4\pi\epsilon_0} \int_{S_j} \frac{1}{|\vec{r}_i - \vec{r}_S|} d^2\vec{r}_S \quad (3.15)$$

The equation system (3.14) is solved using the Gauss-Jordan-algorithm, providing us with the charge densities  $\sigma_j$  of the individual subelements.

The electrodes in the KATRIN setup are in good approximation rotational symmetric. This makes it easy to describe them as cones.

The electric potential of an infinitesimally thin charged ring at a field point  $(z, r)$  is given by the formula:

$$\Phi(z, r) = \frac{Q}{2\pi^2\epsilon_0} \frac{K(k)}{S} \quad (3.16)$$

where

$$S = \sqrt{(R+r)^2 + (z-Z)^2}, \quad k = \frac{2\sqrt{Rr}}{S}, \quad (3.17)$$

$Z$  is the axial coordinate of the ring,  $R$  its radius,  $Q$  its total charge and  $K(k)$  the first complete elliptic integral (see eq. (3.5)).

By numerical integration of this formula, the potential of a conical subelement with constant charge density  $\sigma$  can be computed. A conical subelement, described by two points  $(z_a, r_a)$  and  $(z_b, r_b)$ , can be expressed as a sum of thin charged rings:

$$Z = z_a + (z_b - z_a) \cdot \frac{p}{L}, \quad R = r_a + (r_b - r_a) \cdot \frac{p}{L}. \quad (3.18)$$

Here  $p$  is the distance of the arbitrary subelement point  $(Z, R)$  from the point  $(z_a, r_a)$  that lies between 0 and  $L$ , where  $L$  denotes the length of the line segment. Taking

the infinitesimal charge  $dQ = 2\pi\sigma R dp$  of the ring, the potential of the cone can finally be described:

$$\Phi = \frac{\sigma}{\pi\epsilon_0} \int_0^L dp \frac{RK(k)}{S} \quad (3.19)$$

This integral has divergences, when evaluating it close to the segment. To avoid this the integration region is divided into smaller subintervals, within which the integrand does not have any divergences.

### 3.2.2 Legendre polynomial expansion

Similar to the magnetic field, the zonal harmonic expansion is applicable in case of axisymmetric electric fields. Depending on the convergence ratio, the computation by expansion is much faster than by elliptic integrals. Nevertheless, it needs the charge densities, computed by the BEM, as input parameters, in order to compute the source coefficients at the sourcepoints.

Analogous to eq. (3.8) and (3.9) for the magnetic field, there exists a central polynomial expansion (for  $\rho < \rho_{cen}$ ) for electric fields, given by:

$$\begin{aligned} \Phi(z, r) &= \sum_{n=0}^{\infty} \phi_n^{cen} \left( \frac{\rho}{\rho_{cen}} \right)^n P_n(u) \\ \mathcal{E}_z(z, r) &= -\frac{1}{\rho_{cen}} \sum_{n=0}^{\infty} (n+1) \phi_{n+1}^{cen} \left( \frac{\rho}{\rho_{cen}} \right)^n P_n(u) \\ \mathcal{E}_r(z, r) &= \frac{s}{\rho_{cen}} \sum_{n=0}^{\infty} \phi_{n+1}^{cen} \left( \frac{\rho}{\rho_{cen}} \right)^n P_n'(u) \end{aligned} \quad (3.20)$$

with  $u = \cos \theta$  and  $s = \sin \theta$

and a remote expansion (for  $\rho > \rho_{rem}$ ), given by:

$$\begin{aligned} \Phi(z, r) &= \sum_{n=0}^{\infty} \phi_n^{rem} \left( \frac{\rho_{rem}}{\rho} \right)^{n+1} P_n(u) \\ \mathcal{E}_z(z, r) &= \frac{1}{\rho_{rem}} \sum_{n=1}^{\infty} n \phi_{n-1}^{rem} \left( \frac{\rho_{rem}}{\rho} \right)^{n+1} P_n(u) \\ \mathcal{E}_r(z, r) &= \frac{s}{\rho_{rem}} \sum_{n=1}^{\infty} \phi_{n-1}^{rem} \left( \frac{\rho_{rem}}{\rho} \right)^{n+1} P_n'(u) \end{aligned} \quad (3.21)$$

where, again,  $P_n(u)$  are the Legendre polynomials,  $\phi_n^{rem}$  and  $\phi_n^{cen}$  are the source coefficients at the source points and  $\rho_{rem}$  and  $\rho_{cen}$  are the convergence radii, given by the maximum and minimum distance from the sourcepoint to the electrode. The source coefficients  $\phi_n^{rem}$  and  $\phi_n^{cen}$  are determined by the surface and volume charge of the electrode [Glü09a].

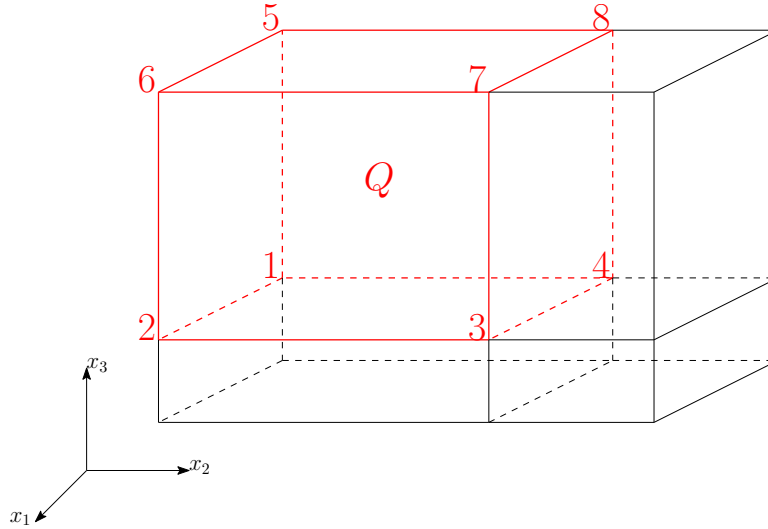
## 3.3 Three-dimensional Hermite-interpolation

### 3.3.1 Motivation

Interpolation methods are often employed when calculating the field of a static setup. The interpolation grid is plotted once in advance and every time the field needs to

be evaluated in a certain point, it is interpolated and optionally scaled using the precomputed grid. The Hermite-interpolation, in contrast to the linear-interpolation does not only need the values at the grid points, but also their partial derivatives. This results in a longer precomputation time, but as the accuracy of the Hermite-interpolation scales not just with the 2nd but with the 4th power of the grid distance, this is the preferred method to use when interpolating with relatively large grids. Interpolating usually means a dramatic speed up of the field calculations, especially for non axisymmetric fields and still grants a high numeric precision. However, in axisymmetric fields, close to the symmetry axis, the Legendre-polynomial methods are faster.

### 3.3.2 Theory



We are given a rectangular, three-dimensional grid that consists of cuboids. A cuboid  $Q$  of this grid can be described as follows.

$$Q := \{(x_1, x_2, x_3) \in \mathbb{R}^3 / x_{ui} < x_i < x_{oi} ; i = 1, 2, 3\} \quad (3.22)$$

Through a coordinate-transformation of the form:

$$\begin{aligned} u_i &= \frac{x_i - x_{mi}}{a_i} \quad \text{with} \\ x_{mi} &= \frac{x_{oi} + x_{ui}}{2} \quad \text{and} \quad a_i = \frac{x_{oi} - x_{ui}}{2} \end{aligned} \quad (3.23)$$

we project  $Q$  to the unit-cube  $E$ :

$$E := \{(u_1, u_2, u_3) \in \mathbb{R}^3 / -1 < u_i < 1 ; i = 1, 2, 3\} \quad (3.24)$$

Now we define a function  $g(\vec{u})$  on  $E$  with:

$$f(\vec{x}) = g(\vec{u}(\vec{x})) \quad (3.25)$$

The goal is to interpolate  $g(\vec{u})$  within the unit-cube  $E$ . Therefore, we need to know the function-values at the eight corner points  $\vec{u}_i$  as well as their first partial derivatives. We combine them into a Matrix  $\mathcal{G}$ , where the function-values fill one column:

$$\mathcal{G}_{i0} := g(\vec{u}_i) \quad (i = 1, \dots, 8) \quad (3.26)$$

and the others are filled by their partial derivatives:

$$\mathcal{G}_{ij} := \left\{ \frac{\partial g(\vec{u})}{\partial u_j} \right\}_{\vec{u}=\vec{u}_i} \quad (i = 1, \dots, 8 ; j = 1, 2, 3) \quad (3.27)$$

The next step is to define a so called Interpolation-polynomial:

$$G(\vec{u}) = \sum_{i=1}^8 \sum_{j=0}^3 \mathcal{G}_{ij} \phi_{ij}(\vec{u}) \quad (3.28)$$

The coefficient-polynomials  $\phi_{ij}$  are chosen, so that  $G(\vec{u}_k) = \mathcal{G}_{k0}$  and  $\left\{ \frac{\partial g(\vec{u})}{\partial u_1} \right\}_{\vec{u}=\vec{u}_k} = \mathcal{G}_{k1}$ . This leads to the following constraints:

$$\phi_{ij}(\vec{u}_k) = \delta_{ik} \delta_{j0} \quad \text{and} \quad \left\{ \frac{\partial \phi_{ij}(\vec{u})}{\partial u_1} \right\}_{\vec{u}=\vec{u}_k} = \delta_{ik} \delta_{j1} \quad (3.29)$$

These are fulfilled, if we define  $\phi_{ij}$  like:

$$\phi_{ij}(\vec{u}) := u_{ij} \prod_{k=1}^3 \varphi_{jk}(u_{ik} \cdot \vec{u}_k) \quad (3.30)$$

where  $\varphi_{jk}$  is given by:

$$\varphi_{jk}(t) := \frac{1}{4} \left[ (2 + 3t - t^3) + (-3 - 4t + t^2 + 2t^3) \delta_{jk} \right] \quad \text{and} \quad u_{i0} := 1 \quad (3.31)$$

In order to interpolate the function  $f(\vec{x})$  within the cuboid  $Q$ , we have to follow some simple steps:

1. calculate the function-values and their partial derivatives of  $f$  regarding  $\vec{x}$  at all 8 corner points,
2. transform them into the unit-cube  $E$ :

$$\mathcal{G}_{ij} = \begin{cases} a_j \cdot \left\{ \frac{\partial f(\vec{x})}{\partial x_j} \right\}_{\vec{x}=\vec{x}_i} & \text{if } j > 0 \\ f(\vec{x}_i) & \text{if } j = 0 \end{cases} \quad (3.32)$$

3. and interpolate function-values and derivatives at any point  $\vec{x} \in Q$  :

$$\begin{aligned} \frac{\partial f(\vec{x})}{\partial x_j} &= a_j^{-1} \cdot \frac{\partial G(\vec{u}(\vec{x}))}{\partial u_j} \quad j = 1, 2, 3 \\ f(\vec{x}) &= G(\vec{u}(\vec{x})) \end{aligned} \quad (3.33)$$

Interpolation methods yield the possibility of a scalable precision. When a high precision is needed, the distance between the grid points can be chosen very small and in the contrary case, when a lower precision is sufficient, it can be chosen rather large. This has no impact on the actual computation time, just on the time needed to compute the initial grid.

## 4. Tracking of charged particles

This chapter describes the mathematical methods and approximations that are used to calculate the trajectories of charged particles in the KATRIN experiment. At first, the Runge-Kutta methods will be introduced, which are able to approximate the solutions of 1st order differential equation systems. This is followed by descriptions, how this numerical solvers can be applied to calculate particle trajectories and field lines. The chapter concludes with a rather simple example of how to calculate relative distances of a particle to geometry components.

### 4.1 The Runge-Kutta method

The Runge-Kutta methods are a family of implicit and explicit iterative methods for the approximation of solutions of ordinary differential equations. They have proven themselves to have a very high precision. In this section, a brief introduction to the explicit 4th order Runge-Kutta (RK4) will be given. Although both the 4th order and 8th order Runge-Kutta methods are being used for particle tracking calculations in the KATRIN experiment, this section will just describe the RK4 method in detail. Conclusively, there will be a short description of the generalization of the RK4 method to higher orders.

The basic idea of the RK methods is the same as for the Euler method: An exact solution  $y = y(x)$  of a 1st order ordinary differential equation

$$y' = f(x; y) \tag{4.1}$$

with the given initial value  $y(x_0) = y_0$  is replaced by a line in every sub-interval of length  $h$ .

The starting point is the given initial point  $P_0 = (x_0; y_0)$ . We replace the solution within the interval  $x_0 \leq x \leq x_1$  with a line that is described by the equation:

$$\frac{y - y_0}{x - x_0} = m \quad \text{or} \quad y = y_0 + (x - x_0)m \tag{4.2}$$

In contrast to the Euler method<sup>1</sup>, the slope  $m$  of the replacement-line is taken as a weighted average of slopes of the solution, taking into account: the slope at the beginning of the interval:  $(k_1)$ ; two mutually distinct computed slopes at the midpoint of the interval:  $(k_2, k_3)$ ; and the slope at the end of the interval:  $(k_4)$ . With these the approximated solution  $y(x)$ , running through  $P_n(x_n; y_n)$  can be computed point-wise:

$$\begin{aligned}
 y(x_{n+1}) \approx y_{n+1} &= y_n + \frac{1}{6} (k_1 + 2k_2 + 2k_3 + k_4) \quad \text{with} \\
 k_1 &= h \cdot f(x_n; y_n) \\
 k_2 &= h \cdot f\left(x_n + \frac{h}{2}; y_n + \frac{k_1}{2}\right) \\
 k_3 &= h \cdot f\left(x_n + \frac{h}{2}; y_n + \frac{k_2}{2}\right) \\
 k_4 &= h \cdot f(x_n + h; y_n + k_3)
 \end{aligned} \tag{4.3}$$

The auxiliary quantities  $k_1, k_2, k_3$  and  $k_4$  have to be computed for every step. The error of the method estimates to:

$$\Delta y_k = y(x_k) - y_k \approx \frac{1}{15}(y_k - \tilde{y}_k), \tag{4.4}$$

where  $y(x_k)$  is the exact solution at  $x_k$ ,  $y_k$  the approximate solution at  $x_k$  with step-size  $h$  and  $\tilde{y}_k$  the approximate solution at  $x_k$  with doubled step-size  $2h$ .

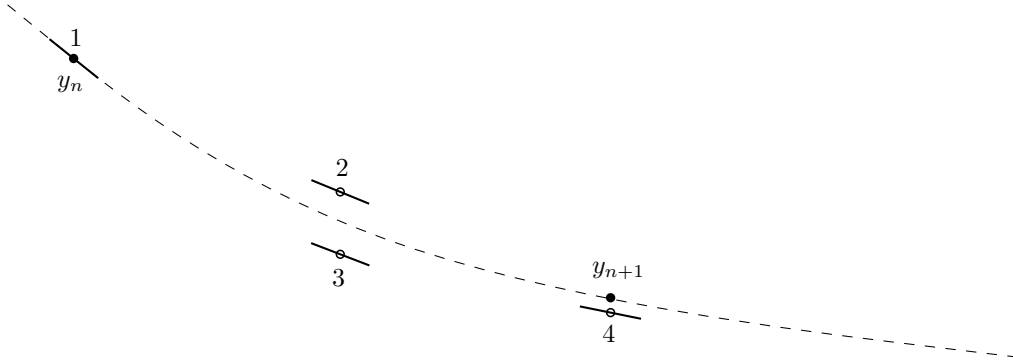


Figure 4.1: Graphical interpretation of the 4th order Runge-Kutta method. In each step the derivative is evaluated four times: once at the initial point, twice at trial midpoints, and once at a trial endpoint. From these derivatives the final function value (filled dot) is calculated. Figure taken from [PTVF07]

The generalization for the approximate solution, taking into account  $s$  derivatives, is given by [Pap96]:

$$y(x_{n+1}) \approx y_{n+1} = y_n + h \sum_{i=1}^s b_i k_i \tag{4.5}$$

<sup>1</sup>In the Euler method, only the slope in the left boundary point of the interval is taken into account.

with the auxiliary quantities  $k_i$  described by:

$$k_i = f \left( x_n + hc_i; h \sum_{j=1}^s a_{ij} k_j \right). \quad (4.6)$$

The coefficients  $b_i$ ,  $c_i$  and  $a_{ij}$  are given through the so called Butcher-tables [Ver78]. Although the RK8 method needs 13 computation steps and the RK4 only 4, RK8 is the preferred method because the step size  $h$  can be chosen larger than RK4 with equal numerical precision. Clever use of this advantage makes the computation about 10 times faster for RK8 than for RK4.

## 4.2 Particle motion in general force fields

This section gives an example, how to apply the Runge-Kutta method to a physical problem. Given is a non-relativistic particle that is moving in a general force field and we aim to calculate its trajectory.

The motion of a particle in such a field can be written as a 1st order differential equation system:

$$\begin{aligned} \dot{x}_j &= v_j \\ \dot{v}_j &= \frac{1}{m} F_j(x_1, x_2, x_3; v_1, v_2, v_3; t) \quad (j = 1, 2, 3) \end{aligned} \quad (4.7)$$

where  $x_1, x_2, x_3$  are the Cartesian space coordinates,  $v_1, v_2, v_3$  are the components of the particle's velocity,  $t$  is the time,  $m$  is the mass of the particle and  $F_j$  are the forces acting on it. The differential equation system (4.7) consists of 6 first order differential equations. The  $y_i$  variables ( $i = 1, \dots, 6$ ) are defined as:

$$\begin{aligned} y_i &= x_i \quad \text{for } i = 1, 2, 3 \text{ and} \\ y_i &= v_{i-3} \quad \text{for } i = 4, 5, 6. \end{aligned} \quad (4.8)$$

Equation (4.7) can now be expressed in terms of the derivative function  $f$ :

$$\begin{aligned} f(i, y_1, \dots, y_6, t) &= v_i \quad \text{for } i = 1, 2, 3 \text{ and} \\ f(i, y_1, \dots, y_6, t) &= \frac{1}{m} F_{i-3} \quad \text{for } i = 4, 5, 6. \end{aligned} \quad (4.9)$$

With these, we are now able to calculate the trajectory of the particle via Runge-Kutta-steps.

## 4.3 Charged particle motion in electric and magnetic fields

For the KATRIN experiment, the trajectories of relativistic electrons are of main interest. Therefore a way to compute the electron-trajectories within electric and magnetic fields is very important.

A particle in an electro-magnetic field is experiencing the Lorentz-force:

$$\vec{F}_L = q \left( \vec{\mathcal{E}} + \vec{v} \times \vec{B} \right) \quad (4.10)$$

with  $q$  being the charge of the particle,  $\vec{v}$  the velocity 3-vector,  $\vec{\mathcal{E}}$  the electric field vector and the  $\vec{B}$  magnetic field vector.

Again, we can write down a first order differential equation system, describing the motion:

$$\begin{aligned}\dot{\vec{x}} &= \vec{v} & \text{and} \\ \dot{\vec{p}} &= \vec{F}_L,\end{aligned}\tag{4.11}$$

where  $\vec{v}$  and  $\vec{p}$  are the velocity and momentum 3-vectors. In this case the  $y_i$  variables are defined by the momentum instead of the velocity:

$$\begin{aligned}y_i &= x_i & \text{for } i = 1, 2, 3 \text{ and} \\ y_i &= p_{i-3} & \text{for } i = 4, 5, 6.\end{aligned}\tag{4.12}$$

For the KATRIN electrons we use the relativistic relations between velocity and momentum:

$$\begin{aligned}\vec{p} &= \frac{m\vec{v}}{\sqrt{1 - \frac{v^2}{c^2}}} & \text{and} \\ \vec{v} &= \frac{\vec{p}}{\sqrt{m^2 + \frac{p^2}{c^2}}},\end{aligned}\tag{4.13}$$

where  $m$  stands for the rest mass. Then the derivate functions are:

$$\begin{aligned}f(i, y_1, \dots, y_6, t) &= v_i & \text{for } i = 1, 2, 3 \text{ and} \\ f(i, y_1, \dots, y_6, t) &= \frac{1}{m} F_{L,i-3} & \text{for } i = 4, 5, 6.\end{aligned}\tag{4.14}$$

with  $v_i$  being calculated using the relations from the equations (4.13). For further information see [Glü02].

## 4.4 Field lines

When speaking of the motion of charged particles, field lines might not be the first thing that comes to mind. In fact, calculation of field lines and calculation of particle trajectories are very related to each other, as they are both defined by a specific force.

In general, the calculation of field lines is a very important task in electro-magnetic simulations. It is essential when studying new electrode designs to, for example, control the electric potential along a magnetic field line in order to avoid penning traps. It is even possible to approximate the actual electron trajectory with a field line, as the electrons perform a cyclotron motion around those field lines, thus saving computation time.

The differential equation system defining a field line of a three-dimensional vector field  $\vec{A}$  is:

$$\frac{dx_i}{ds} = \pm \frac{A_i}{|\vec{A}|} \quad (i = 1, 2, 3).\tag{4.15}$$

with  $s$  denoting the path. This equation system is time independent. Instead of a force that depends on location and velocity, the “force“ in the case of field lines

just depends on the position. As usual, we define  $y_i$  variables for the Runge-Kutta method:

$$y_i = x_i \quad \text{for } i = 1, 2, 3, \quad (4.16)$$

and the derivative functions  $f$ , which embed the "force":

$$f(i, y_1, y_2, y_3, t) = \pm \frac{A_i}{|\vec{A}|} \quad \text{for } i = 1, 2, 3. \quad (4.17)$$

As the initial differential equation system (4.15) has only 3 components, the computation of field lines is pretty fast. By slightly modifying the "force", so that it points orthogonal to field vector, it is also possible to compute equipotential lines.

## 4.5 Adiabatic approximation

Charged particles flying through a time- and position-independent magnetic field perform a uniform cyclotron motion. It can be described by a circular motion with its center moving along the magnetic field lines. If the magnetic field is in fact dependent on time or position there is no longer an ideal cyclotron motion, but is assumed as an approximately cyclotron-like motion. The basic idea of the *adiabatic approximation* is that the actual motion can be approximated by taking the ideal motion and adding some corrections to it.

At first the motion of the center of the cyclotron motion, the so called guiding centre motion shall be described. It is very similar to the field lines and given by the differential equation system:

$$\begin{aligned} \dot{\vec{x}} &= \frac{B_i}{|\vec{B}|} v_{\parallel} \quad \text{and} \\ p_{\parallel} &= -\frac{\mu}{\gamma} \vec{\nabla}_{\parallel} \vec{B} + q\mathcal{E}_{\parallel}, \end{aligned} \quad (4.18)$$

where  $\mu = \frac{p_{\perp}^2}{2m|\vec{B}|}$  is the magnetic moment,  $\gamma = \sqrt{1 + \frac{p_{\parallel}^2 + p_{\perp}^2}{m^2 c^2}}$  the Lorentz-factor and  $\mathcal{E}_{\parallel}$  the electric field parallel to the magnetic field  $\vec{B}$ . The velocity  $v_{\parallel}$ , the momentum  $p_{\parallel}$  and the gradient  $\nabla_{\parallel}$  are parallel to the magnetic field as well.

The  $y_i$  variables are then defined as follows:

$$\begin{aligned} y_i &= x_i \quad \text{for } i = 1, 2, 3 \quad \text{and} \\ y_i &= p_{\parallel} \quad \text{for } i = 4. \end{aligned} \quad (4.19)$$

The derivative functions are again obtained by the force:

$$\begin{aligned} f(i, y_1, \dots, y_4, t) &= \frac{B_i}{|\vec{B}|} v_{\parallel} \quad \text{for } i = 1, 2, 3 \quad \text{and} \\ f(i, y_1, \dots, y_4, t) &= -\frac{\mu}{\gamma} \vec{\nabla}_{\parallel} \vec{B} + q\mathcal{E}_{\parallel} \quad \text{for } i = 4. \end{aligned} \quad (4.20)$$

The guiding centre performs a longitudinal motion along the magnetic field lines. To approximate the real cyclotron motion, a motion transversal to the magnetic field lines has to be added.

With the adiabatic invariant  $\mu = \frac{\gamma+1}{2} \frac{E_{\perp}}{|\vec{B}|}$  (see section 2.3.2) and the transversal momentum  $p_{\perp} = 2\mu m |\vec{B}|$  the cyclotron radius can be expressed by:

$$r = \frac{\gamma m v_{\perp}}{q |\vec{B}|} = \frac{p_{\perp}}{q |\vec{B}|} \quad (4.21)$$

With the given step size of the Runge-Kutta step  $h$  and the cyclotron frequency  $\omega = \frac{q |\vec{B}|}{m \gamma}$ , the change of the azimuthal angle results to:

$$\Delta\varphi = \omega h \quad (4.22)$$

The cyclotron radius and the change of azimuthal angle completely describe the approximated transversal motion. They are simply added to the guiding centre position at the end of the Runge-Kutta step, resulting in an adiabatic approximated step.

This approximation has proven itself to be very fast if the step size  $h$  is large. For small step sizes  $h$  and especially when tracking close to an electrode, this approximation is often slower than the "exact" numerical solution, because it requires more electric field calculations, which are rather slow. The step size is controlled by monitoring the energy conservation. If the energy conservation within one step is not good enough, the step size is reduced and the step is redone. If it is sufficient, the step size for the next step is increased.

A gyrating electron performs an additional magnetron motion. This magnetron drift has also to be added separately to the step, for further informations see [Thu02].

## 4.6 Distance calculation

In order to decide which field calculation method to use during particle tracking and when investigating if a particle hits a certain geometrical object, it is crucial to know the distance between the particle and the geometrical components. This allows dynamic switching between field calculation methods and trajectory monitoring and control, depending on this distance.

Nearly all geometries to which we want to check the distance can be approximated by cones. Therefore, we can simplify the task of distance monitoring, to distance calculations to various cones forming the geometry. Figure 4.2 shows a general cone described by two points  $(\vec{a}_1, \vec{a}_2)$  and two radii  $(r_1, r_2)$ .

First, we calculate the "orientation" vector  $\vec{n}$  of the cone:

$$\vec{n} = \frac{\vec{a}_2 - \vec{a}_1}{|\vec{a}_2 - \vec{a}_1|}, \quad (4.23)$$

It describes the orientation of the two boundary planes of the cone. For the special case of a disc ( $\vec{a}_1 = \vec{a}_2$ ) this vector must be specified. The next step is projecting  $\vec{x}_i$  to the symmetry axis of the cone:

$$\vec{x}'_i = \vec{a}_1 + [\vec{n} \cdot (\vec{x}_i - \vec{a}_1)] \vec{n}. \quad (4.24)$$

With  $\vec{x}'_i$  it is already possible to check if the point  $\vec{x}_i$  lies within the volume defined by the cone surface ( $|\vec{x}'_i - \vec{a}_j| \geq |\vec{a}_1 - \vec{a}_2|$ ). Now we build a unity vector pointing into

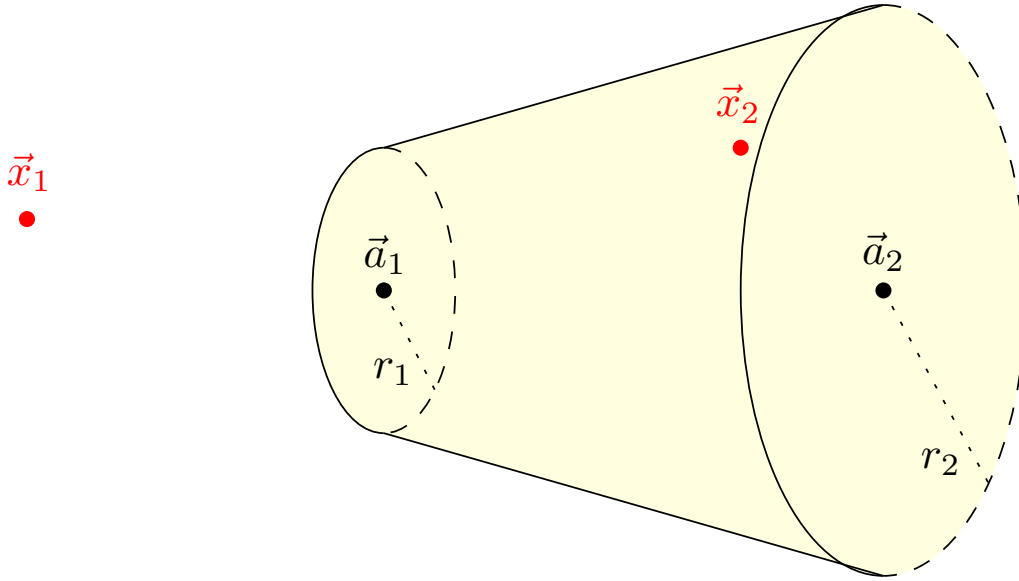


Figure 4.2: Illustration of a cone, represented by two the vectors pointing to the start- and endpoint of the cone on its symmetry axis  $\vec{a}_1$  and  $\vec{a}_2$ , and two radii at these points  $r_1$  and  $r_2$ . The distance shall be calculated for a point outside the cone ( $\vec{x}_1$ ) and a point inside the cone ( $\vec{x}_2$ ).

the direction from  $\vec{x}'_i$  to  $\vec{x}_i$  and project it onto the edges of the cone. This defines two points  $\vec{\alpha}_1$  and  $\vec{\alpha}_2$  on the cone edges:

$$\vec{\alpha}_j = \vec{a}_j + r_j \frac{\vec{x}_i - \vec{x}'_i}{|\vec{x}_i - \vec{x}'_i|}. \quad (4.25)$$

In the case of point  $\vec{x}_1$  that lies outside of the cone, the distance is obtained by just calculating

$$d_j = |\vec{\alpha}_j - \vec{x}_1|, \quad (4.26)$$

and searching for the minimum. For  $\vec{x}_2$  we need to calculate another auxiliary vector  $\vec{\beta}$  that lies on the line, linking two points on the cone edges,  $\vec{\alpha}_1$  and  $\vec{\alpha}_2$ :

$$\vec{\beta} = \vec{\alpha}_1 + \left[ \frac{\vec{\alpha}_2 - \vec{\alpha}_1}{|\vec{\alpha}_2 - \vec{\alpha}_1|} (\vec{x}_2 - \vec{\alpha}_1) \right] \frac{\vec{\alpha}_2 - \vec{\alpha}_1}{|\vec{\alpha}_2 - \vec{\alpha}_1|}. \quad (4.27)$$

The requested distance  $d$  is then given by:

$$d = |\vec{x}_2 - \vec{\beta}| \quad (4.28)$$

In order to save computation time this computation chain is executed up to equation (4.26) and then just the distances to the cones within as sphere, defined by  $\varepsilon_d$  are computed further.



# 5. Code implementation

This chapter deals with the implementation of the calculation methods introduced in the chapters 3 and 4 into a C++ framework. Several of them existed already in C-code [Glü06]. In context of this diploma thesis, together with S. Mertens and with contributions of N. Wandkowsky, they were reworked and rewritten into a more technically sophisticated form, in order to be standardised, flexible, modular and easy to use. The novel implementations of the line-segment and interpolation methods form the KNAXS (**K**ATRIN **N**on-**A**Xisymmetric field **S**imulation) field calculation package. The following chapter is not a line per line programme documentation but a basic description of the classes and how they work. The source-code is fully available from the KATRIN-subversion-repository [rep]. The whole code is now part of the **Kassiopeia** framework that aims to be a universal tool for a complete physical simulation of the KATRIN experiment. It includes the simulation of the source, especially gas dynamics and particle generation, *field calculation* and *particle tracking* and simulation of detector and data-aquisition [Ob].

## 5.1 Overview

Figure 5.1 shows an overview of the **KTrack** framework. It is able to track charged particles within almost the whole KATRIN experiment, and can, in addition, compute electric and magnetic field lines of specified fields.

The framework features a management structure, consisting of the following classes:

- **Initializer**: it reads in the major configuration file, creates and configures all other objects that are needed for trajectory calculation.
- **ExitConditionChecker**: this class monitors the particle being tracked and checks if any exit conditions for the track are reached, like, for example, the particle leaving the area of interest or hitting a wall etc.
- **TrackOutput**: this class manages the output of the programme. It writes user configured information about the track into an output file.

The physics component classes are independent and, though being created by the **Initializer** during runtime, not members of the **KTrack** framework, except for the

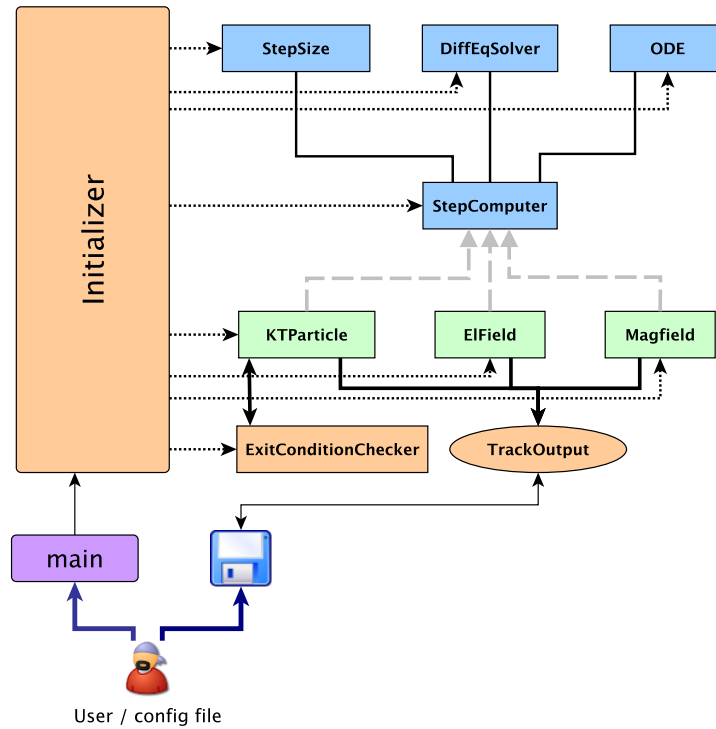


Figure 5.1: Overview of the KTrack program package. Shown is the structure that divides into the management classes (orange), the physics classes (green) including the external field classes and the core components (blue), responsible for the trajectory calculation.

**KTrackParticle.** The `KTrackParticle` describes not only the physical attributes of a particle, like mass and charge, but contains also some technical information like a label, a time stamp and other track information. The field classes will be discussed in more detail in the following section 5.2.

The core component classes work together in order to perform the actual tracking. They are discussed in detail in section 5.3.

## 5.2 Field classes

The field classes in the Kassiopia programme package have to be compatible and usable by a lot of other classes and programmes. Because of this, two abstract base classes were defined, `Elfield` and `Magfield`, and every electric and magnetic field class must inherit from them.

Listing 5.1 shows the source code of the `Elfield` base class. It uses `TVector3`, a class from the `ROOT` programme package [ROO] that represents a three-dimensional vector. The two virtual methods `GetField` and `GetPhi` are pure and have to be redefined by every derived class. They are the key interface to obtain the electric field and potential.

Listing 5.1: The header Elfield.h that describes the abstract class Elfield

```

class Elfield
{
    public :

        Elfield () {}
        virtual ~Elfield () {}
        virtual TVector3 GetField(const TVector3& p) = 0;
        virtual double GetPhi(const TVector3& p) = 0;

};

```

Listing 5.1: The header Elfield.h that describes the abstract class Elfield

Listing 5.2 shows the source code of the `Magfield` base class. It is very similar to the `Elfield` class and uses also the `TVector3` class from `ROOT`. `Magfield` has the pure, virtual method `GetField` that has to be redefined in every derived class analogously to `Elfield` it returns the magnetic field at the field point specified by the `Tvector3` `p`.

Listing 5.2: The header Magfield.h that describes the abstract class Magfield

```

class Magfield
{
    public :

        Magfield () {}
        virtual ~Magfield () {}
        virtual TVector3 GetField(const TVector3& p) = 0;

};

```

Listing 5.2: The header Magfield.h that describes the abstract class Magfield

### 5.2.1 Magfield3

`Magfield3` is based on the `magfield3.c` C-program [Glü06]. It calculates the magnetic field by using the elliptic integrals or the Legendre polynomial expansion (see section 3.1.2). It is also capable of magnetic field calculations for a coil system with different axial symmetry axes.

The input-file describing the coil setup does have the following structure:

```

N
J[1]  A[1][x-z]  B[1][x-z]  Rmin[1]  Rmax[1]  n[1]
⋮      ⋮ ⋮ ⋮      ⋮ ⋮ ⋮      ⋮          ⋮          ⋮
J[N]  A[N][x-z]  B[N][x-z]  Rmin[N]  Rmax[N]  n[N]

```

with `N` being the number of coils described in the setup, `J[i]` being the current density in the coil, `A[i][x-z]` and `B[i][x-z]` being the coordinates of the coil end points, `Rmin[i]` and `Rmax[i]` being the inner and outer radii of the coil and `n[i]` being the number of subsegments the coil is divided into for numerical integration. These parameters are all given in SI-units.

Prior to the magnetic field computation, `Magfield3` tests the input coils and writes them, with additional information, in a file (extension `.magcoil3`). Then it computes the central and remote source points and coefficients for the coil system, and stores them in separate files that are either specified by the user or chosen automatically. These files carry the extensions `.magsource3_central` and `.magsource3_remote` respectively. The source points and coefficients for all coils with the global axis as symmetry axis are evaluated separately and stored in a file with the extension `.magsource3_axisymm`. This last step is not essential, but it offers the opportunity to save computation time, because the Legendre polynomial expansion of these coil can be combined to one.

After these preparing computations, the field at a point, defined by the `TVector3 position`, is obtained with the `GetField(position)` method. Depending on the distance from the field point to the coils and the symmetry axis, the method chooses either the Legendre polynomial expansion method or the elliptic integrals to compute the magnetic field.

### 5.2.2 Elfield2

The `Elfield2` class is based on the C-program `elcd2.c` [Gli06]. It is able to compute the electric potential and field of an electrode system that consists of solid, axially symmetric electrodes using the field computation methods introduced in section 3.2. The class is not able to compute the field and potential of wires present in the geometry directly, but they have to be approximated by solid cones. The input files the extension `.el2` and are of the following structure:

```

N
g[1]  Z1[1]  R1[1]  Z2[1]  R2[1]  U[1]  n[1]
:      :      :      :      :      :      :
g[N]  Z1[N]  R1[N]  Z2[N]  R2[N]  U[N]  n[N]

```

`N` specifies the number of electrodes in the file. `g[i]` denotes the group index, `Z1[i]`, `R1[i]` and `Z2[i]`, `R2[i]` are the cylindrical coordinates of the cone edges, `U[i]` the voltages of the cones and `n[i]` the number of conical subelements, a cone is divided in for numerical integration. Again all physical quantities are given in SI-units.

The class has to perform three steps in advance as preparation, in order to be able to compute the electric field and potential:

1. Discretization of the full electrodes into many small subelements. They are saved in a file with the extension `.element2`.
2. Calculation of the charge densities within the subelements, using the boundary element method.
3. Calculation of the source coefficients at the source points. They are written in a file with the extension `.elsource2`.

With these steps done the class is now able to calculate the electric field and potential. As it inherits from the abstract base class `Elfield`, the virtual method `GetField(position)` returns the electric field, and the virtual method `GetPhi(position)` the electric potential, at any field point specified by the `TVector3 position` for

which the field calculation methods are valid. The class decides automatically which method to use, elliptic integrals or Legendre polynomial expansion, depending on the convergence radii.

### 5.2.3 Elfield32

`Elfield32` is an upgrade of the `Elfield2` class is based on the C-program `elcd3_2.c` [Glü06]. In addition to the calculation of the electric field and potential of full electrodes, it is also able to compute the electric field and potential of wire electrodes that have a cylindrical symmetry with the centre on the  $z$ -axis. Therefore they have to be approximated as linear segments. The input files for `Elfield32` have the extension `.el32`. The input file for the full electrodes looks as following:

```

N
Z1[1]  R1[1]  Z2[1]  R2[1]  U[1]  n[1]
⋮      ⋮      ⋮      ⋮      ⋮      ⋮
Z1[N]  R1[N]  Z2[N]  R2[N]  U[N]  n[N]

```

It is almost the same as for the `Elfield2` class, except that the group index is missing. Again,  $N$  specifies the number of electrodes in the file,  $Z1[i]$ ,  $R1[i]$  and  $Z2[i]$ ,  $R2[i]$  are the cylindrical coordinates of the cone edges,  $U[i]$  the voltages of the cones and  $n[i]$  the number of conical subelements, a cone is divided into for numerical integration.

The wires are defined in a separate input file with the form :

```

N
Z1[1]  R1[1]  Z2[1]  R2[1]  d[1]  phi[1]  Numwire[1]  U[1]  n[1]
⋮      ⋮      ⋮      ⋮      ⋮      ⋮      ⋮      ⋮      ⋮
Z1[N]  R1[N]  Z2[N]  R2[N]  d[N]  phi[N]  Numwire[N]  U[N]  n[N]

```

$N$  specifies the number of wire electrodes. The wires of a wire electrode lie on a cone with startpoint  $Z1[i]$ ,  $R1[i]$  and endpoint  $Z2[i]$ ,  $R2[i]$  given in cylindrical coordinates. The wire diameter  $d[i]$  in meter, their azimuthal angle  $\phi[i]$  in deg and their number  $Numwire[i]$  are specified additionally. Again,  $U[i]$  denotes the voltage of the wires and  $n[i]$  the number of subelements the wires have to be divided into for numerical integration.

`Elfield32` has to do the same preparation calculation as `Elfield2`, with the difference that the wire electrodes are represented by linear instead of conical segments. Analogously, a subelement file with the extension `.element32` and a source coefficient file with the extension `.elsource32` are created. `Elfield32` also inherits from the abstract base class `Elfield`, and thereby redefines the `GetPhi` and `GetField` methods. Like `Elfield2`, it is able to switch between calculation of the full electrodes by elliptic integrals or Legendre polynomial expansion, depending on the position of the field point.

### 5.2.4 Elfield33

The class `Elfield33` is able to compute the electric potential and field of an arbitrary electrode system, and is based on the C-program `elcd3_3.c` [Glü06]. However, the

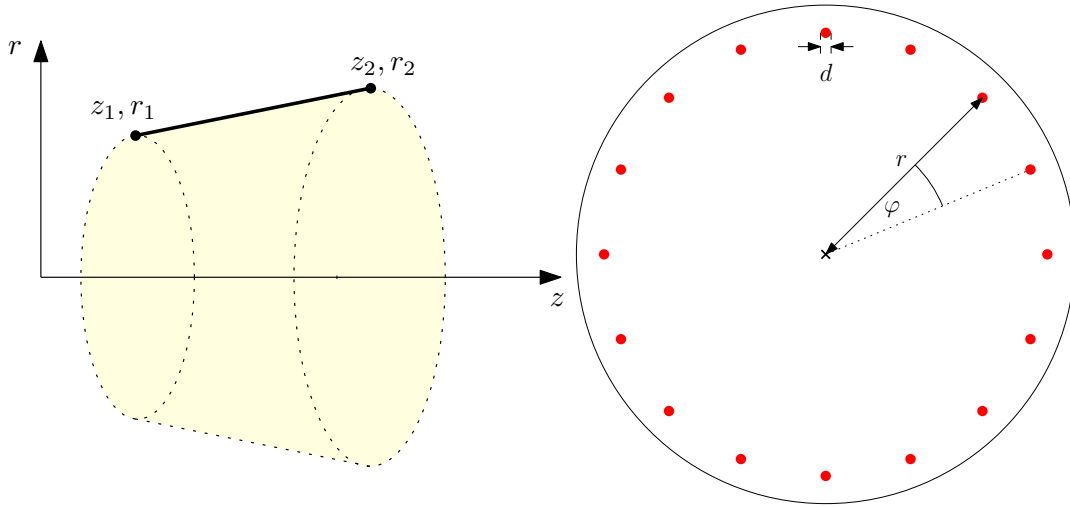


Figure 5.2: Graphical explanations of the electrode input parameters.

class is not able to do a discretization of the electrodes on its own. The user has to do this in advance, and then pass the appropriate input file with the extension `.el33` that contains the discretized electrode geometry to the method. The input file is of the form:

```

L
  1[1]  g[1]  type[1]  rot[1]  P1-P11[1]  U[1]
  ⋮      ⋮      ⋮      ⋮      ⋮      ⋮
  1[L]  g[L]  type[L]  rot[L]  P1-P11[L]  U[L]

```

`L` specifies the number of lines in the file, and thereby the number of subelements, `1[i]` are the subelement indices and `g[i]` the subelement-group indices, which are the same for subelements with the same charge density. `type[i]` are integers that determine the type of the subelements: for `type[i]=1` the subelement is a rectangle and for `type[i]=2` it is a wire. The integers `rot[i]` define the rotational number, if they are greater than 1, `rot[i]-1` extra subelements are added. They are obtained by discrete rotational transformations of the given subelements along the  $z$ -axis, forming a uniform azimuthal distribution. The values of `type[i]` and `rot[i]` should be the same for every subelement in a group `g[i]`. The eleven parameters `P1-P11[i]` define the geometry of the subelements. For rectangles (`type[i]=1`) they have the following definition (see figure 5.3):

- `P1-P3[i]` are the three Cartesian coordinates of a corner point  $P_0$  of the rectangles
- `P4-P6[i]` are the components of the unit vector  $\vec{n}_1$  that points from  $P_0$  towards the neighbouring corner point  $P_1$
- `P7-P9[i]` are the components of the unit vector  $\vec{n}_2$  that points from  $P_0$  towards the other neighbouring corner point  $P_2$ , the vectors  $\vec{n}_1$  and  $\vec{n}_2$  should be orthonormal
- `P10[i]` are the edge lengths  $a$  of the rectangles corresponding to  $\vec{n}_1$
- `P11[i]` are the edge lengths  $b$  of the rectangles corresponding to  $\vec{n}_2$

As for wires (`type[i]=2`), they have the definitions:

- `P1-P3[i]` are the three Cartesian coordinates of one endpoint  $P_a$  of the wires
- `P4-P6[i]` are the three Cartesian coordinates of the other endpoint  $P_b$  of the wires
- `P7[i]` are the diameters  $d$  of the wires
- `P8-P11[i]` are not used, but must be filled with arbitrary numbers, in case of wires

`U[i]` contains the voltages of the subelements.

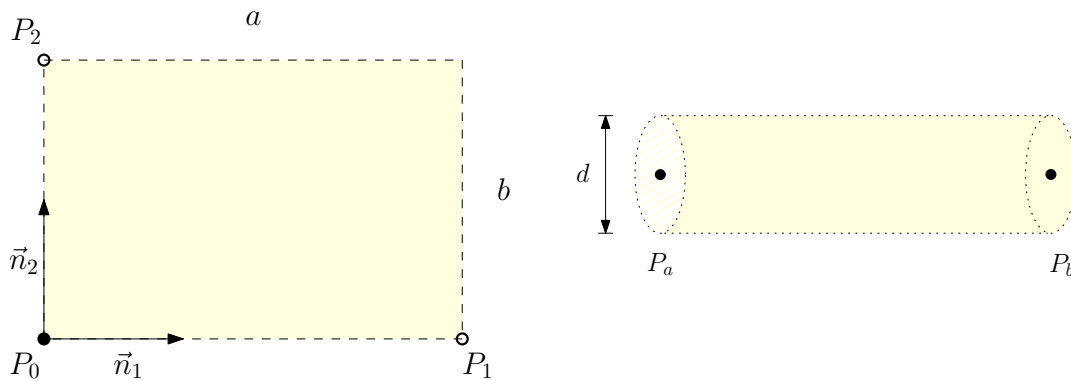


Figure 5.3: Geometrical parameter definition of a rectangular (left) and a wire (right) subelement.

After the subelements are read in, the corresponding charge densities are calculated via a Gauss-Jordan-algorithm using their voltage values. The subelements and their charge densities are written into a file with the extension `.element33`. With all preparations done, the `Elfield33` class is able to calculate the electric potential and field of the given geometry by numerical integration. Similar to all electric field classes, it inherits from the abstract base class `Elfield`, redefining the `GetPhi` and `GetField` methods. The field and potential calculations in `Elfield33` are rather slow, compared to other electric field calculation classes. This is due to the fact that the fast Legendre polynomial expansion can only be used with axially symmetric electrode setups. On the other hand, `Elfield33` has the advantage that it can cope with all kinds of (discretized) electrode geometries.

### 5.2.5 BiotSavart

This class is an implementation of the integrated Biot-Savart method introduced in section 3.1.1.1. Figure 5.4 shows a diagram of the class.

`BiotSavart` uses line-current segments with which the geometry is approximated, and calculates their resulting magnetic field. It is possible to read in input lines from a file and/or create and add `Line` objects dynamically during runtime. The input file, with the extension `.bio`, has the form:

```

X1[0]  Y1[0]  Z1[0]  X2[0]  Y2[0]  Z2[0]  I[0]
⋮      ⋮      ⋮      ⋮      ⋮      ⋮      ⋮
X1[N]  Y1[N]  Z1[N]  X2[N]  Y2[N]  Z2[N]  I[N]

```

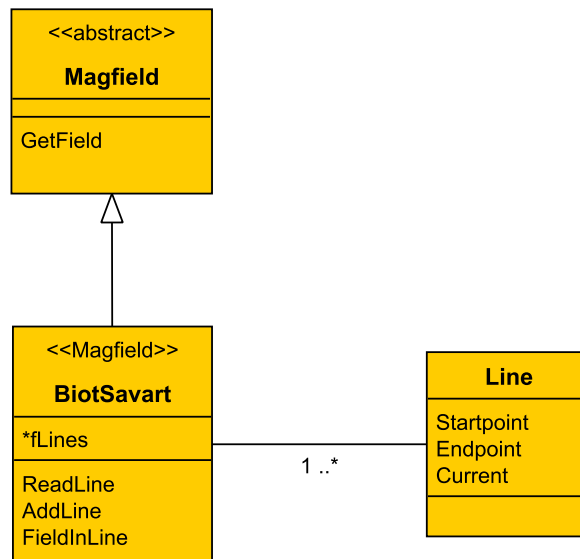


Figure 5.4: Overview of the **Biot-Savart** class: It inherits from **Magfield** and has one or more member objects of the class **Line**.

where  $X1-Z1[i]$  and  $X2-Z2[i]$  are the Cartesian coordinates of the start and endpoint and  $I[i]$  is the current in the line segment, flowing from the start- to the endpoint. So, every row describes one **Line** object that is added to the **BiotSavart** object. As it inherits from the abstract class **Magfield**, the field at the field point **TVector3 position** can be obtained by the virtual method **GetField(position)**.

## 5.2.6 MagMaterials

The **MagMaterials** class calculates the magnetic field of dipole-bars, as described in section 3.1.1.2. Figure 5.5 shows a principle diagram of the class.

The dipole-bars are described by **Bar** objects, which can, analogously to the **BiotSavart** class, be read in from an input file and/or created and added during runtime. The input files use the extension **.magmat** and contain data with the following format:

$X1[0]$	$Y1[0]$	$Z1[0]$	$X2[0]$	$Y2[0]$	$Z2[0]$	$M[0]$	$R[0]$	$Chi[0]$
$\vdots$								
$X1[N]$	$Y1[N]$	$Z1[N]$	$X2[N]$	$Y2[N]$	$Z2[N]$	$M[N]$	$R[N]$	$Chi[N]$

A **Bar** object is described by: the Cartesian coordinates of its start- and endpoint  $X1-Z1[i]$  and  $X2-Z2[i]$ , the strength of the magnetisation pointing from the start- to the endpoint  $M[i]$ , the radius of the bar  $R[i]$  and the magnetic susceptibility  $Chi[i]$  of the bar material. As for all classes, derived from **Magfield**, the field can be obtained with the **GetField** method.

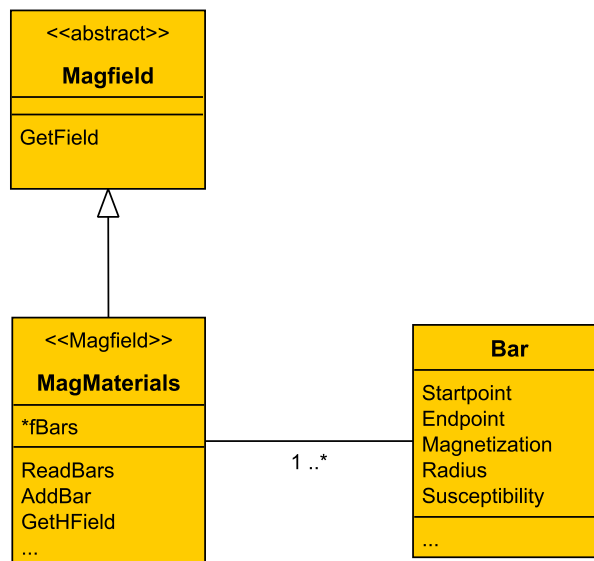


Figure 5.5: Overview of the `MagMaterials` class: It inherits from `Magfield` and has one or more member objects of the class `Bar`.

### 5.2.7 Interpolation

In section 3.3 we learned about using the three-dimensional Hermite-interpolation to speed up field calculations. This method was implemented in a very modular design into the class `FieldInterpolation`. The classes `MagfieldInterpolate` and `ElfieldInterpolate` inherit from this class, and of course from the abstract field base classes. Figure 5.6 shows a principle diagram of the `MagfieldInterpolate` class and figure 5.7 of the `ElfieldInterpolate` class, respectively.

Objects of the stereotype `FieldInterpolation` store one or more interpolation grids in objects of the stereotype `Fieldmap`. These grids contain for example the scalar electric potential with just one value at a grid point in case of a `Fieldmap1` object, and the grids for the three-dimensional vector fields, that have three values and nine partial derivatives in one grid point, are stored in `Fieldmap3` objects. In case of rotational symmetry, one can also use the `Fieldmap2` objects, but this has to be specified explicitly by the user.

In order to pre-compute a grid, the virtual methods `CreateMagFieldmap` and `CreateElFieldmap` that are members of the `Fieldmap` classes have to be called. They compute a grid of the specified `Magfield` or `Elfield` object, respectively. `CreateElfieldmap` actually creates two field maps, one for the electric field and one for the potential. Afterwards they are saved to a file and can be read in with the virtual method `ReadMapFromFile`. For the `Fieldmap1` classes, the grid points are stored into files of the form:

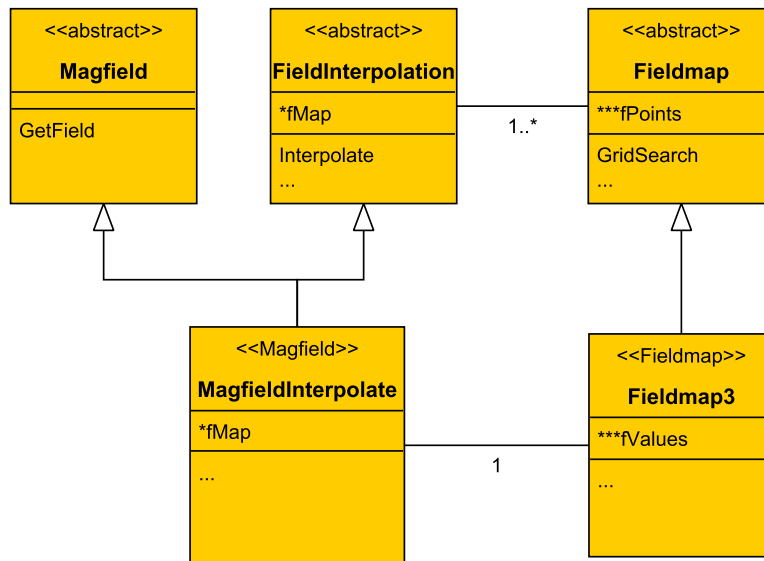


Figure 5.6: Overview of the `MagfieldInterpolate` class: It inherits from the abstract classes `Magfield` and `FieldInterpolation`. It has one member object of the class `Fieldmap3` that inherits from the abstract class `Fieldmap`.

NX	NY	NZ	d			
X[0]	Y[0]	Z[0]	Val[0]	d/dX[0]	d/dY[0]	d/dZ[0]
⋮	⋮	⋮	⋮	⋮	⋮	⋮
X[N]	Y[N]	Z[N]	Val[N]	d/dX[N]	d/dY[N]	d/dZ[N]

where  $NX$ - $Z$  are the edge sizes of the grid,  $d$  is the grid spacing,  $X$ - $Z[i]$  are the Cartesian coordinates of the grid point,  $Val[i]$  is the value at the grid point and  $d/dX$ - $d/dZ[i]$  are the partial derivatives of the value at the grid point. The input files for the `Fieldmap2` and `Fieldmap3` classes are similar but instead of just one entry for the value they have two and three respectively, each of them with its own set of partial derivatives. The `Fieldmap` classes implement a fast `GridSearch` method that return the corner point indices to the `FieldInterpolate` class. It obtains the indices by a component-wise integer division of the field point coordinates with respect to the origin of the interpolation grid. This is very fast but only usable in isotropic interpolation grids.

### 5.3 Tracking classes

Section 5.1 and the graph shown in figure 5.1 give a short introduction to the `KTrack` framework. In this section the core components of `KTrack` that are responsible for the actual tracking will be discussed further.

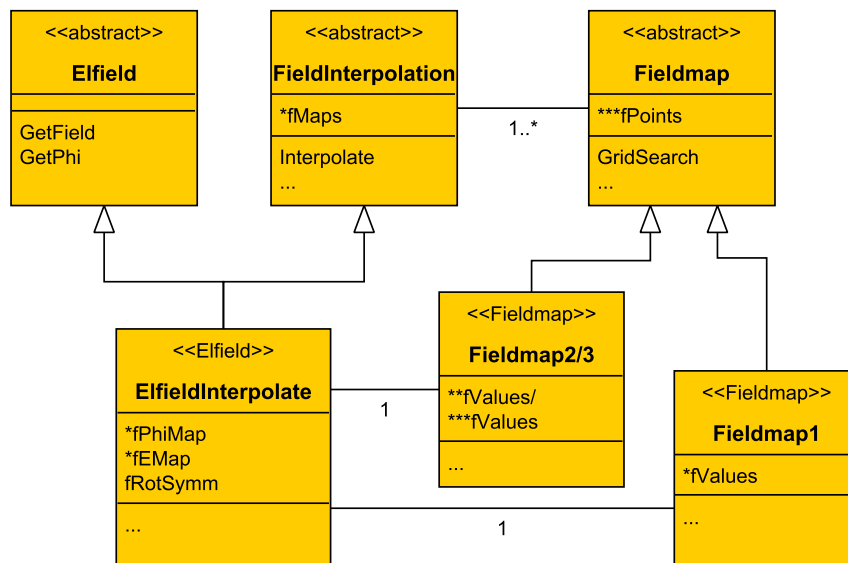


Figure 5.7: Overview of the `ElfieldInterpolate` class: It inherits from the abstract classes `Elfield` and `FieldInterpolation`. It has two member objects that inherit from the abstract class `Fieldmap`: a `Fieldmap1` object, in which the interpolation grid for the electric potential is stored and a `Fieldmap2` or `Fieldmap3` object, depending if the field is axially symmetric, in which the interpolation grid for the electric field is stored.

### 5.3.1 KTrackParticle

The class `KTrackParticle` is a virtual analogue to a physical particle, and has the same basic attributes: charge, mass, position and momentum. To save computation time, the class has extensive attributes like: kinetic energy, polar and azimuthal angles,  $\Theta$  and  $\varphi$ , to the magnetic field, velocity, kinetic energy and their corresponding longitudinal and transversal components, Lorentz-factor, etc. Altogether, there are 28 additional parameters to the 4 that are needed to uniquely describe a particle. Some of them are derived physical quantities and some of them are technical quantities, like the particle-label or the total path length travelled by the particle during tracking. The physical attributes of the `KTrackParticle` can be retrieved and altered by `Get...` and `Set...` methods. After setting an attribute, the `Update` method has to be called to guarantee consistency of the particle's physical attributes. The `KTrackParticle` also stores information about scattering processes that could have happened during the track.

### 5.3.2 StepSize

`StepSize` is an abstract base class. The derived classes implement two virtual functions: `ComputeTimeStep` that returns the step size  $h$  for the next tracking step and `Check` which tests the last tracking step and returns a boolean if valid (`true`) or not (`false`). At the moment, there are three other classes that implement the `StepSize` class:

- **StepSizeFix**: A trivial implementation that always returns a constant step size. The step size is defined in the constructor of the class. It is the only step determination method functional without any magnetic field.
- **StepSizeCyclotron**: This class returns a fraction of the duration of one cyclotron period at the particle's current location. The fraction and global upper and lower limits for the step size are defined in the constructor of the class.
- **StepSizeEnergy**: This class should only be used, when using the adiabatic approximation. It calculates the particle's kinetic energy before and after the step. If the energy conservation lies within user-defined limits, the step is valid and the step size for the next step is increased up to the step size limit. If the energy conservation is not below the upper limit, the step size is reduced and the step is redone. The energy conservation and step size limits are specified in the constructor of the class.

In contrast to other components of the step computation mechanism, **StepSizeCyclotron** and **StepSizeEnergy** are not usable for other purposes than for tracking. For other tasks that require the numerical solution of differential equation systems, for example field line calculation, only **StepSizeFix** can be used.

### 5.3.3 DiffEqSolver

All of the numerical solvers for differential equation systems implement the abstract **DiffEqSolver** class. The class has the virtual member function **Solve**. The step size  $h$ , the initial conditions  $y_i$  and the ODE<sup>1</sup> object, which simply computes the derivative functions  $f_i$ , are passed to this function. It returns a `vector<double>` in which the final conditions are stored. At the moment three classes exist that implement these base class: **RungeKutta4** and **RungeKutta8** which are 4th and 8th error order implementations of the Runge-Kutta method introduced in section 4.1, and the experimental **PredictorCorrector** class that uses the Predictor-Corrector method to numerically solve first order differential equation systems [PTVF07].

### 5.3.4 StepComputer

The task of the **StepComputer** class is to manage the **StepSize**, ODE and **DiffEqSolver** objects and compute the attributes of the **KTrackParticle** at the location of the next step. It also computes energy loss due to synchrotron radiation and checks if scattering events occurred, calculates the attributes of the particle after scattering and even creates secondary particles. **StepComputer** is an abstract base class and has just one interface, the virtual function **MakeStep**. The input for this method are the **KTrackParticle** to track and pointers of the type **Elfield\*** and **Magfield\*** to the polymorphic electric and magnetic field objects. With these it computes the step and writes its parameters into the **KTrackParticle** object. There are two classes implementing **StepComputer**:

- **ExactStep**: This step computer uses the “exact” numerical solution of the equation (4.10) to compute the step.
- **ApproxStep**: This step computer uses the adiabatic approximation described in section 4.5.

---

<sup>1</sup>ODE stands for ordinary differential equation.

To ensure the physical consistency of the `KTrackParticle` at any time during the runtime of the programme, the changes computed during the `MakeStep` call are stored in an intermediate particle. At the end of the step, this is then written into the `KTrackParticle` object.

## 5.4 Comparison

The most important reasons for the creation of the `KTrack` and `KNAXS` programme packages were:

- making the simulation tools more user friendly and simplify their structure
- improved flexibility by modular design
- equal or better precision and equal or faster computation speed

In order to evaluate, if these intentions were fulfilled, several computations were done as comparison. Therefore, `KTrack` and `KNAXS` were compared with pre existing, software, if any, or, in case of the interpolation and line segment methods, compared with other field calculation methods.

### 5.4.1 Ktrack compared to singletraj.c

`singletraj.c` is a pre existing C-programme [Glü06], for fast tracking of particles within the pre- and main spectrometer. It uses `magfield2.c` to compute the magnetic field and `elcd2.c` to compute the electric field and potential. Hence, only particle tracks in axially symmetric systems can be computed, as `magfield2.c` does not support tilted coils.

A track through the main spectrometer of an electron with 10 eV surplus energy to the analysing potential was used for this comparison. The stepping parameters were the same for both programmes and the positions of the particular steps agreed with a precision of  $10^{-6}$  m for exact tracking and  $10^{-4}$  m for adiabatic approximation. The track was run 10 times with every programme on an *Intel Core 2 Quad Q6600* with 4 GB of RAM and Ubuntu Linux 8.04 installed. The average values of the particular computation times are listed in the tabular below:

stepping type	KTrack		singletraj.c	
	Exact	Approx	Exact	Approx
time	4.5 s	1.5 s	10.6 s	2.5 s

This table clarifies two things: the adiabatic approximation normally just takes a quarter of the time of the exact computation and `KTrack` is nearly twice as fast as `singletraj.c`. The main reason for this is the consequent performance optimisation done in the step computers and numerical solvers of `KTrack`. For example, all objects are passed by reference, the memory is allocated dynamically and the routines were generally straightened.

## 5.4.2 Interpolation precision and computation time

In order to evaluate the possible fields of application for the field interpolation method, several test computations were done. In preparation, four particular interpolation grids were computed, with different grid spacings 1 mm, 5 mm, 10 mm and 50 mm. They were compared with the other field calculation methods that are currently implemented. As test  $10^5$  arbitrary points were chosen within the pre-spectrometer at which the particular fields were calculated. This ensures that field interpolations in both, rather homogeneous and rather inhomogeneous regions are taken into account. Field points at which some methods would not be able to compute the field, e.g. inside the coils or electrodes, were not used. The time for needed the function call was recorded with the C-function `clock()` and averaged over all points. In addition, the relative errors of the fields magnitude and components, and in the case of electric fields, additionally the potential, were averaged.

### MagfieldInterpolate vs. BiotSavart

For this test calculation, the field of a model of the EMCS with 672 line-elements was calculated.

$d$ [mm]	$t$ [s]	$t_{interp}$ [s]	error	error <sub><math>x</math></sub>	error <sub><math>y</math></sub>	error <sub><math>z</math></sub>
1	6.112 e-04	1.720 e-05	3.74e-08	0	3.74e-08	0
5	4.160 e-04	5.000 e-06	5.03e-09	0	5.03e-09	0
10	4.230 e-04	2.000 e-06	2.70e-08	0	2.70e-08	0
50	4.110 e-04	1.100 e-05	5.75e-08	0	5.75e-08	0

Table 5.1: Computation time and error comparison between `MagfieldInterpolate` and `BiotSavart`.

Table 5.1 and shows the results of the test.  $t$  denotes the average time for the `GetField` function call of `BiotSavart` and  $t_{interp}$  for `MagfieldInterpolate`, respectively. As expected, both times are independent of the grid spacing and the interpolation is about ten to a hundred times faster than `BiotSavart` even with this relatively small number of line-elements to calculate. The relative error is shown for the absolute magnetic field and the three field components. A 0 for the error means, that the numbers agree with double precision. Even for the largest grid-spacing of 50 mm the error is in the order of  $10^{-8}$  and thereby more than sufficient. For the interpolation of the EMCS, the grid-spacing could be chosen even larger, to save memory and to shorten the computation time of the interpolation grid.

### MagfieldInterpolate vs. MagMaterials

The second test computation was the comparison of `MagfieldInterpolate` against `MagMaterials`. The magnetic field of a model consisting of 2142 dipole bars was computed and interpolated within the main spectrometer.

Table 5.2 shows the results of this test computations. Again the computation times of the interpolation are in the order of microseconds. And due to the many elements to compute the `MagMaterials` class is 500 times slower. The relative errors are one to two orders of magnitudes higher than for the interpolation of the EMCS. This is due to the stronger inhomogeneity of the field caused by the magnetic materials.

$d$ [mm]	$t$ [s]	$t_{interp}$ [s]	error	error <sub><math>x</math></sub>	error <sub><math>y</math></sub>	error <sub><math>z</math></sub>
1	1.181 e-03	8.000 e-06	5.51e-07	5.63e-06	2.15e-05	2.72e-08
5	1.403 e-03	6.000 e-06	2.88e-06	2.82e-05	1.07e-04	1.39e-09
10	1.178 e-03	1.000 e-05	5.71e-06	5.65e-05	2.14e-04	4.02e-08
50	1.175 e-03	9.000 e-06	2.86e-05	2.88e-04	1.06e-03	1.35e-08

Table 5.2: Computation time and error comparison between `MagfieldInterpolate` and `MagMaterials`

However, even the error for 50 mm grid-spacing in the order of  $10^{-5}$  is acceptable. With a fixed model of the magnetic dipole distribution in the experimental area, implying just one initial computation of the interpolation grid, `MagfieldInterpolate` is a significantly better choice for field computation.

#### `MagfieldInterpolate` vs. `Magfield3` (Legendre polynomial)

For this test the magnetic fields of all the coils in the KATRIN setup were computed inside the main spectrometer.

$d$ [mm]	$t$ [s]	$t_{interp}$ [s]	error	error <sub><math>x</math></sub>	error <sub><math>y</math></sub>	error <sub><math>z</math></sub>
1	8.100 e-06	1.270 e-05	4.34e-08	9.49e-03	0	4.34e-08
5	8.100 e-06	1.150 e-05	8.56e-08	4.73e-02	0	8.54e-08
10	8.800 e-06	1.220 e-05	4.32e-08	9.40e-02	0	4.34e-08
50	7.000 e-06	1.300 e-05	2.35e-08	4.50e-01	0	2.19e-08

Table 5.3: Computation time and error comparison between `MagfieldInterpolate` and `Magfield3` (Legendre polynomial).

The results are shown in table 5.3. As expected, the Legendre polynomial expansion of the magnetic field is about twice as fast as the interpolation. The relative errors are very small except for the  $x$ -component. In this case `Magfield3` would be the better choice, as it is faster and the error of the  $x$  component would require a small grid-spacing.

#### `MagfieldInterpolate` vs. `Magfield3` (elliptic integrals)

Again, the magnetic fields of all the coils in the KATRIN setup were computed inside the main spectrometer, but this time `Magfield3` was forced to use the elliptic integral field computation method.

$d$ [mm]	$t$ [s]	$t_{interp}$ [s]	error	error <sub><math>x</math></sub>	error <sub><math>y</math></sub>	error <sub><math>z</math></sub>
1	1.524 e-02	2.400 e-05	4.31e-08	9.49e-03	0	4.32e-08
5	1.413 e-02	2.100 e-05	8.65e-08	4.73e-02	0	8.64e-08
10	1.515 e-02	1.800 e-05	3.78e-08	9.40e-02	0	3.80e-08
50	1.450 e-02	1.200 e-05	9.11e-09	4.50e-01	0	7.53e-09

Table 5.4: Computation time and error comparison between `MagfieldInterpolate` and `Magfield3` (elliptic).

The results are shown in table 5.4. The errors are in the very same order as for the Legendre polynomial expansion. And due to the time consuming numerical integration, `MagfieldInterpolate` is nearly a thousand times faster than `Magfield3` when being forced to use the elliptic integral method. A computation method would be possible, that combines the Legendre polynomial expansion that uses interpolation instead of elliptic integrals in region where the expansions do not converge, thus gaining computation speed in these regions.

#### ElfieldInterpolate vs. Elfield2 (Legendre polynomial)

For this test, the electric potential and field of the main spectrometer electrode setup were calculated. As usual for computations with `Elfield2`, the wire electrodes were approximated by full electrodes.

$d$ [mm]	$t$ [s]	$t_{interp}$ [s]	error	error <sub><math>x</math></sub>	error <sub><math>y</math></sub>	error <sub><math>z</math></sub>	error <sub><math>\Phi</math></sub>
1	2.10 e-05	1.20 e-05	5.026e-08	0	0	2.384e-09	9.024e-08
5	1.30 e-05	1.00 e-05	1.277e-06	0	0	9.564e-08	9.024e-08
10	1.60 e-05	1.10 e-05	4.753e-06	0	0	1.073e-07	1.812e-07
50	1.70 e-05	1.00 e-05	1.457e-04	0	0	4.568e-05	1.273e-07

Table 5.5: Computation time and error comparison between `ElfieldInterpolate` and `Elfield2` (Legendre polynomial).

Table 5.5 shows the results of this test computations. The polynomial expansion for the electric field is insignificantly slower than for the magnetic field. The relative errors are very small and that of the  $x$  and  $y$  component are even better than double precision for all grid-spacings. For this case no clear recommendation can be given, as the computation times are almost equal and the interpolation needs an extensive preparation.

#### ElfieldInterpolate vs. Elfield2 (elliptic integrals)

Again, the electric potential and field of the main spectrometer electrode setup were calculated, but this time forcing `Elfield2` to use the elliptic integral method.

$d$ [mm]	$t$ [s]	$t_{interp}$ [s]	error	error <sub><math>x</math></sub>	error <sub><math>y</math></sub>	error <sub><math>z</math></sub>	error <sub><math>\Phi</math></sub>
1	7.01 e-03	7.00 e-06	5.03e-08	0	0	2.38e-09	9.02e-08
5	7.00 e-03	1.20 e-05	1.28e-06	0	0	9.56e-08	9.02e-08
10	1.03 e-02	1.50 e-05	4.75e-06	0	0	1.07e-07	1.81e-07
50	9.99 e-03	2.00 e-05	1.46e-04	0	0	4.57e-05	1.27e-07

Table 5.6: Computation time and error comparison between `ElfieldInterpolate` and `Elfield2` (elliptic).

Table 5.6 shows the results of this test computations. The relative errors are in the same regime as for the the Legendre polynomial expansion method. As expected, the interpolation is over a five hundred times faster than the numerical integration. This suggesting to replace the field computation of `Elfield2` in region where elliptic integrals would be used with the interpolation method.

ElfieldInterpolate vs. Elfield32 (Legendre polynomial)

This time we use again a geometry of the main spectrometer electrodes, but with accurate wire electrodes. The field computation of `Elfield32` using Legendre polynomial expansion is compared with `ElfieldInterpolate`.

$d$ [mm]	$t$ [s]	$t_{interp}$ [s]	error	error <sub><math>x</math></sub>	error <sub><math>y</math></sub>	error <sub><math>z</math></sub>	error <sub><math>\Phi</math></sub>
1	1.00 e-05	1.40 e-05	7.16e-09	0	0	1.73e-08	1.00e-07
5	8.00 e-06	1.10 e-05	2.33e-07	0	0	2.20e-08	1.00e-07
10	7.00 e-06	1.00 e-05	9.31e-07	0	0	1.01e-07	9.98e-08
50	6.00 e-06	1.50 e-05	2.49e-06	0	0	2.62e-05	1.66e-07

Table 5.7: Computation time and error comparison between `ElfieldInterpolate` and `Elfield32` (Legendre polynomial).

The results are shown in table 5.7. Again the computation times for the expansion and the interpolation are almost equal. And the relative errors are very small. Regarding the pre-computation time for the grid, the polynomial expansion should be preferred over the interpolation in regions where it is applicable.

ElfieldInterpolate vs. Elfield32 (elliptic integrals)

Again, the electrode geometry of the main spectrometer with accurate wire electrodes is used to compare the field computation of `Elfield32` and `ElfieldInterpolate`. This time with `Elfield32` being forced to use elliptic integrals.

$d$ [mm]	$t$ [s]	$t_{interp}$ [s]	error	error <sub><math>x</math></sub>	error <sub><math>y</math></sub>	error <sub><math>z</math></sub>	error <sub><math>\Phi</math></sub>
1	5.72 e-02	2.60 e-05	2.37e-06	0	0	2.36e-06	1.00e-07
5	3.87 e-02	1.70 e-05	4.60e-05	0	0	4.63e-05	1.00e-07
10	3.96 e-02	1.30 e-05	2.67e-04	0	0	2.66e-04	9.98e-08
50	3.91 e-02	8.00 e-06	5.31e-04	0	0	4.99e-04	1.66e-07

Table 5.8: Computation time and error comparison between `ElfieldInterpolate` and `Elfield32` (elliptic).

The results are shown in table 5.8. `ElfieldInterpolate` is about two thousand times faster than `Elfield32` operating with elliptic integrals. The relative errors are slightly higher between than for the polynomial expansion, especially the error of the  $z$  component. Again, a combination of the Legendre polynomial expansion and the interpolation method is recommendable.

ElfieldInterpolate vs. Elfield33

For the comparison calculations with `Elfield33` a square condenser geometry with two plates of  $1 \times 1$  m edge lengths and a distance of 25 cm was created and discretized. The field and potential was calculated in arbitrary points between.

The results of the test computations are shown in table 5.9. As `Elfield33` does a numerical integration it is more than a thousand times slower than the interpolation. The relative errors of the absolute field and potential are very small in contrast to the errors of the  $x$  and  $y$  component. This could be explained by the very small values of these field components, as they are almost zero between the plates of a

$d$ [mm]	$t$ [s]	$t_{interp}$ [s]	error	error <sub><math>x</math></sub>	error <sub><math>y</math></sub>	error <sub><math>z</math></sub>	error <sub><math>\Phi</math></sub>
1	7.32 e-02	1.60 e-05	2.87e-08	1.19e-01	1.30e-01	2.87e-08	1.43e-07
5	4.87 e-02	2.70 e-05	6.02e-07	4.32e-01	4.04e-01	6.01e-07	3.84e-07
10	5.84 e-02	2.30 e-05	1.67e-06	1.87e-01	3.00e-02	1.67e-06	1.40e-06
50	6.93 e-02	9.00 e-06	1.33e-03	3.14e-01	1.16e-01	1.33e-03	1.34e-03

Table 5.9: Computation time and error comparison between `ElfieldInterpolate` and `Elfield33`.

square condensator. So, even with large grid-spacings, `ElfieldInterpolate` would be a suitable substitute for `Elfield33` for purposes where fast calculation of static fields is needed.

## 6. Investigation of background due to non-axially-symmetric fields

Environmental radioactivity and cosmic rays are able to create secondary charged particles inside the walls and electrodes of the KATRIN spectrometers. In addition, field emission of electrons at electrode edges due to a suboptimal electrode design could occur. If these particles would be able to enter the flux tube and therefore be guided to the detector, they would create a background in the kHz region.

Measurements of the background rate from the walls at the pre spectrometer and Mainz spectrometer [Glü09b] can be up-scaled to the main spectrometer surface and give an expected background rate of  $10^5 \frac{1}{s}$ . However, the required background rate is  $10^{-2} \frac{1}{s}$ , so effective methods to reduce background created by particles coming from these surfaces are needed.

### 6.1 Magnetic shielding

In section 2.3.5 the reduction of the background coming from the walls by the inner wire-electrodes was already discussed. The wire-electrodes are on slightly more negative potential than the vessel hull and thereby reflect electrons coming from the walls. This reduces the background rate by a factor of  $10^2$ . In addition, another mechanism to reduce the background from walls is present in the KATRIN spectrometers, the so called *magnetic shielding*.

The combination of electric and magnetic fields in a MAC-E filters leads to a magnetron drift  $\vec{v}_d$  of the background electrons. It has two components (see figure 6.1):

$$\vec{v}_d = \vec{v}_{\vec{\mathcal{E}} \times \vec{B}} + \vec{v}_{\nabla B} \quad (6.1)$$

where the first component is the  $\vec{\mathcal{E}} \times \vec{B}$  drift:

$$\vec{v}_{\vec{\mathcal{E}} \times \vec{B}} = \frac{\vec{\mathcal{E}} \times \vec{B}}{|\vec{B}|^2} \quad (6.2)$$

and the second component is the gradient  $\vec{B}$  drift:

$$\vec{v}_{\nabla B} = \frac{(E_{\perp} + 2E_{\parallel})}{|\vec{B}|^3} (\nabla B \times \vec{B}) \quad (6.3)$$

which actually would have the opposite sign for positively charged particles.  $\vec{\mathcal{E}}$  and  $\vec{B}$  denote the electric and magnetic field vectors in SI-units, and  $E_{\perp}$  and  $E_{\parallel}$  are the transversal and longitudinal energy components of the electron in eV.

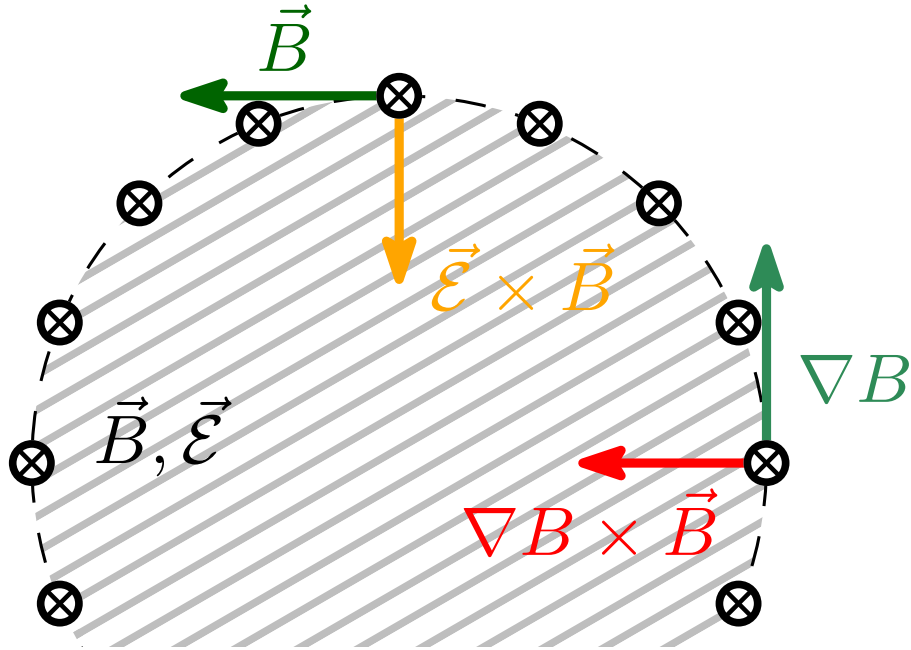


Figure 6.1: Excerpt from the cross section of the flux tube. Azimuthal  $\vec{B}$  and  $\nabla B$  components cause a radial drift.

In the case of axially symmetric fields  $\vec{\mathcal{E}}$ ,  $\vec{B}$  and  $\nabla B$  are parallel within the  $zr$ -meridian plane. As a result, the magnetron drift of the electron is perpendicular to this plane and has no axial or radial component, only an azimuthal one. This means that the electron does not change its radial position  $r$  due to magnetron drift. Therefore, the electron will follow a magnetic field line in the meridian plane and a circle with constant radius in the  $xy$ -plane. Thus it will not be able to enter the flux tube.

With a perfectly axisymmetric magnetic field, the background reduction factor of this method would be infinite. The maximum allowed deviation from axial symmetry of the magnetic field is about 5 mG, leading to a corresponding reduction factor would be of the order of  $10^5$ [Col04].

## 6.2 Non-axially symmetric field contributions

There are several sources of non-axially symmetric magnetic fields which have to be taken into account for the KATRIN-experiment. The most significant ones are the Earth's magnetic field, stray fields from magnetic materials within the walls of the building and magnetic stray fields caused by deformed coils. As the Earth's magnetic field is very homogeneous, it can be compensated with a cosine coil system, the EMCS. The other components are less homogeneous and have to be modelled when investigating the axial symmetry of the magnetic field within the spectrometers.

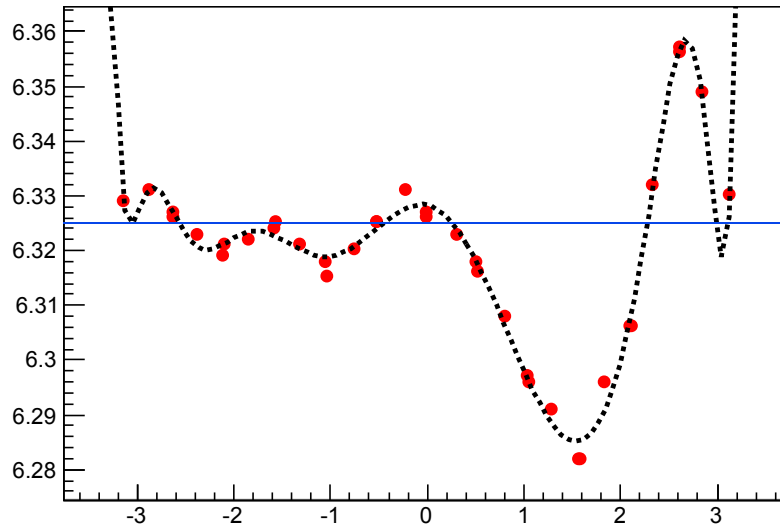


Figure 6.2: Radius in m over azimuthal angle in rad of a LFCS mounting ring. The red dots are measured points, the dashed black line is the fitted function and the blue line denotes the nominal radius.

### 6.2.1 Deformed LFCS

The mounting structure on which the aircoil system is installed has some deviations from the circular shape due to mechanical tolerances. These deviations have been measured with a precision of  $\pm 0.5$  cm in 36 points on the mounting rings.

Figure 6.2 shows the measured points of one ring. A polynomial function fit was applied to them and the ring was then discretized into line segments with the radius dependency obtained from the polynomial fit. Afterwards, the resulting discrete model was compared with actual field measurements to validate it.

### 6.2.2 Magnetic materials in the building's walls

Magnetised steel bars within the walls and the floor of the KATRIN-hall are deploying a relatively strong, inhomogeneous magnetic field. These magnetic stray fields within the KATRIN-hall have been measured, and with these measurements a model for the distribution of magnetic dipole bars has been created [Rei10]. Of course, this model was also validated by additional measurements, to ensure a true-to-reality model of the magnetic materials.

In figure 6.3 some test-field-calculations of the magnetic stray field in the analysing plane are shown. The deviation is of the order of 40 mG which is quite high and mostly caused by the magnetic materials.

Figure 6.4 shows the azimuthal magnetic field component and the figures 6.5 show the  $\nabla_{\varphi} B$  and the resulting radial drift velocity due to the non-axisymmetric contributions on a circle with radius 4 m in the analysing plane. As the drift velocities are rather small, compared to the average time of an electron spent within in the

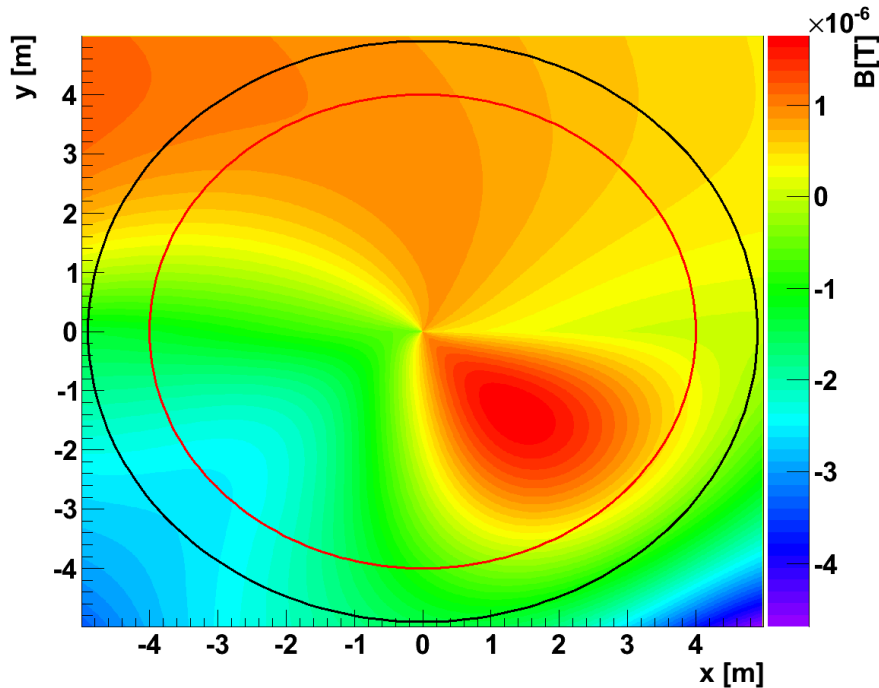


Figure 6.3: Azimuthal magnetic field components in the analysing plane of the main spectrometer. The black circle denotes the vessel hull, the red circle is the radius where the drift velocities were calculated.

main spectrometer ( $\approx 10^{-6}$  s), only low energetic electrons that are stored within the spectrometer are really affected.

### 6.3 Particle tracks influenced by non-axisymmetric magnetic fields

The non-axisymmetric magnetic field contributions are simulated with objects of the `BiotSavart` and `MagneticMaterials` classes. This makes it possible to add them to the ordinary magnetic field contributions of the experiment and calculate particle trajectories using the total magnetic field. As we are searching for background electrons that enter the flux tube, we have to investigate trajectories of low energetic electrons that start from the surface and are stored in the main spectrometer.

Figures 6.6 and 6.7 show a particle that actually enters the flux tube and would be able to cause background particles that are guided to the detector, by scattering or residual gas ionisation. The storage time for such a particle is of the order of seconds. In this period a scattering will almost certainly happen, as the low energetic electrons are in the maximum of the cross-section for residual gas ionisation. In addition, this storage time leads to a computation time that is in the order of weeks. To speed this up, an interpolation grid of the magnetic stray field was created and used for particle tracking, resulting in a reduction of computation time down to a few days.

These test calculations show that it is possible for background electrons with an energy of about 2 eV to get into the flux tube and it can be assumed that they

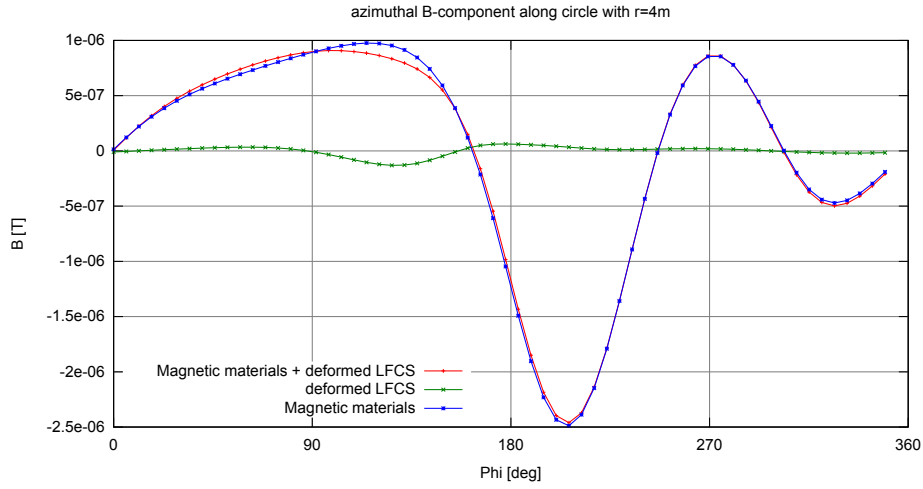


Figure 6.4: Azimuthal  $\vec{B}$  component on a circle of 4 m radius in the analysing plane of the main spectrometer.

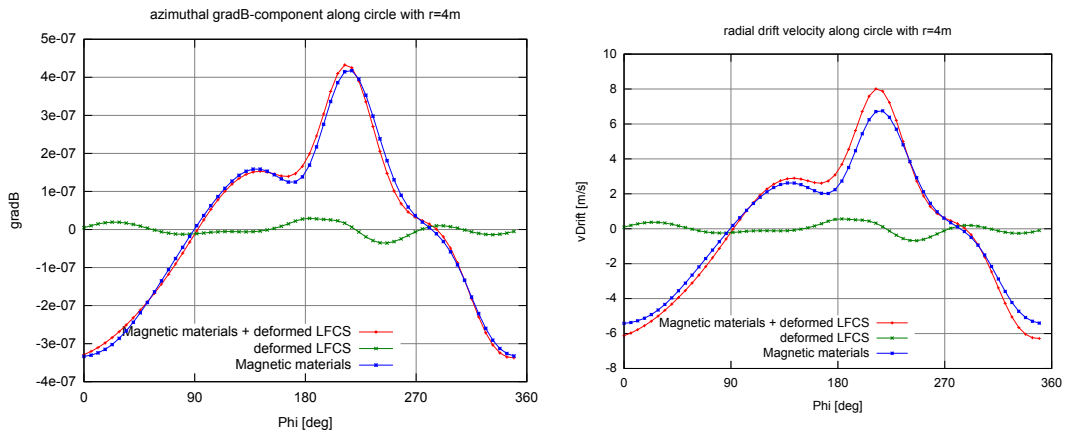


Figure 6.5: Azimuthal  $\nabla B$  (left) and radial drift velocity (right) on a circle with radius of 4 m in the analysing plane of the KATRIN main spectrometer.

will cause background particles there. To evaluate the actual reduction factor of the magnetic field in pre- and main spectrometer a big Monte-Carlo-simulation has to be done, which has to consider the actual creation mechanisms and rates of the electrons that are emitted from the walls.

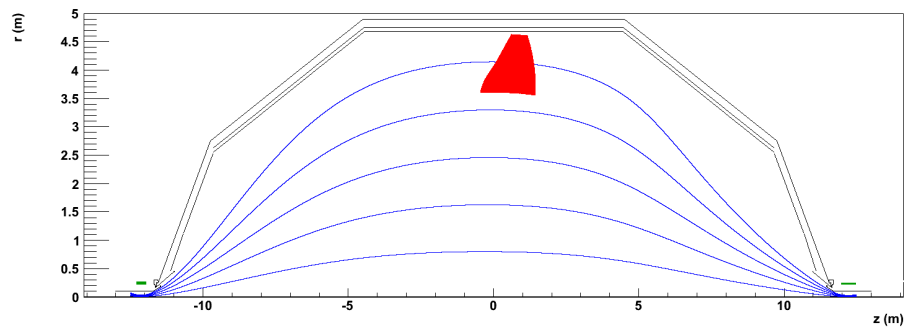


Figure 6.6: Electron trajectory in the  $z$ - $r$  plane (red). The electron started from the vessel hull with 2 eV of kinetic energy. The track was stopped in the flux tube (blue) because a scattering event happened.

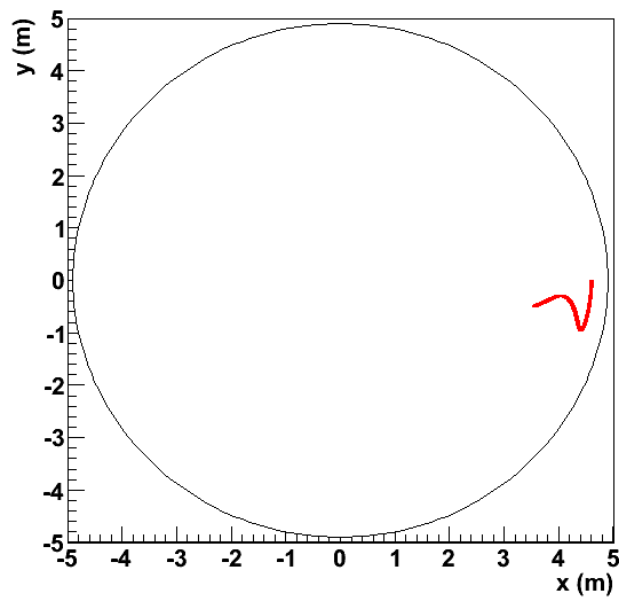


Figure 6.7: Same electron trajectory in the  $x$ - $y$  plane (red). The black line marks the vessel hull.

## 7. Summary and outlook

The KATRIN experiment aims to determine the mass of the electron anti-neutrino with a sensitivity of 0.2 eV (90%C.L.). A precision measurement of the tritium- $\beta$ -spectrum close to the endpoint energy will be done. The experiment uses two MAC-E filter type spectrometers that work on the principle of magnetic adiabatic collimation with an electrostatic filter.

This diploma work focussed on the creation and rework of new and pre-existing tools for the electromagnetic design of the KATRIN MAC-E filters. In its context, the C-codes of the magnetic and electric field calculation programmes (written by F.Glück) were rewritten into a user friendly and flexible object oriented version that now forms the KAFCA (**K**ATRIN **F**ield **C**Alculation). Furthermore, a programmes package that is able to simulate non axially symmetric fields and offers an interpolation method, KNAXS (partially basing on pre-existing C-routines) was implemented. And, together with F. Glück, S. Mertens and N. Wandkowsky a new programme package to compute electron trajectories (basing on an old C-version) KTrack was implemented.

During this diploma thesis, these programmes were developed further and tested extensively. In this process, more and more compatibilities to other programme packages, simulating experimental components like the source or detector, were added. So that today there exists a stable and reliable tool set for all kinds of electron trajectory and field simulation purposes for the KATRIN experiment. And it not only exists, its simple but sophisticated form makes it easy to use and to expand. For this reason, it established itself as standard simulation tool, used to investigate all kinds of problems in the electromagnetic design.

With the help of the KTrack, KAFCA and KNAXS packages, the study of the impacts of non-axially symmetric magnetic field on background electrons, starting from the walls of the main spectrometer was started. First simulations show that, with the current stray fields in the KATRIN-hall, it is possible for low energetic electrons ( $\approx 2$  eV) starting from the wall to get into the flux tube, thus creating a background signal.

To investigate and quantify this background, a large Monte-Carlo-Simulation with realistic presuppositions concerning secondary electron spectra and rate has to be done in the future. Another future task is the further integration of KTrack, KNAXS and KAFCA into the Kassiopeia framework, with the long term goal of an integration of Kassiopeia into ORCA and ADEL, for the purposes of fast near-time simulations.

# Bibliography

- [A<sup>+</sup>96] K. Assamagan *et al.*, “Upper limit of the muon-neutrino mass and charged pion mass from momentum analysis of a surface muon beam,” *Phys. Rev.*, vol. D53, pp. 6065–6077, 1996.
- [A<sup>+</sup>97] W. W. M. Allison *et al.*, “Measurement of the atmospheric neutrino flavour composition in soudan 2,” *Physics Letters B*, vol. 391, p. 491, 1997. [Online]. Available: doi:10.1016/S0370-2693(96)01609-7
- [A<sup>+</sup>02a] J. Abdurashitov *et al.*, “Solar neutrino flux measurements by the soviet-american gallium experiment (sage) for half the 22-year solar cycle,” *Journal of Experimental and Theoretical Physics*, vol. 95, no. 2, pp. 181–193, 2002.
- [A<sup>+</sup>02b] Q. R. Ahmad *et al.*, “Direct evidence for neutrino flavor transformation from neutral-current interactions in the sudbury neutrino observatory,” *Phys. Rev. Lett.*, vol. 89, no. 1, p. 011301, Jun 2002.
- [A<sup>+</sup>03] M. Apollonio *et al.*, “Search for neutrino oscillations on a long baseline at the CHOOZ nuclear power station,” *Eur. Phys. J.*, vol. C27, pp. 331–374, 2003.
- [A<sup>+</sup>05a] B. Aharmim *et al.*, “A search for periodicities in the B-8 solar neutrino flux measured by the Sudbury Neutrino Observatory,” *Phys. Rev.*, vol. D72, p. 052010, 2005.
- [A<sup>+</sup>05b] E. Aliu *et al.*, “Evidence for muon neutrino oscillation in an accelerator-based experiment,” *Phys. Rev. Lett.*, vol. 94, p. 081802, 2005.
- [A<sup>+</sup>05c] T. Araki *et al.*, “Measurement of neutrino oscillation with KamLAND: Evidence of spectral distortion,” *Phys. Rev. Lett.*, vol. 94, p. 081801, 2005.
- [A<sup>+</sup>05d] Y. Ashie *et al.*, “A Measurement of Atmospheric Neutrino Oscillation Parameters by Super-Kamiokande I,” *Phys. Rev.*, vol. D71, p. 112005, 2005.
- [aaa98] T. S.-K. C. al al al al al, “Study of the atmospheric neutrino flux in the multi-gev energy range,” *Physics Letters B*, vol. 436, p. 33, 1998. [Online]. Available: <http://www.citebase.org/abstract?id=oai:arXiv.org:hep-ex/9805006>
- [B<sup>+</sup>82] G. Battistoni *et al.*, “FULLY CONTAINED EVENTS IN THE MONT BLANC NUCLEON DECAY DETECTOR,” *Phys. Lett.*, vol. B118, p. 461, 1982.

- [B<sup>+</sup>89] C. Berger *et al.*, “Study of Atmospheric Neutrino Interactions with the Frejus Detector,” *Phys. Lett.*, vol. B227, p. 489, 1989.
- [B<sup>+</sup>98] R. Barate *et al.*, “An upper limit on the tau neutrino mass from three- and five-prong tau decays,” *Eur. Phys. J.*, vol. C2, pp. 395–406, 1998.
- [BPG04] J. N. Bahcall and C. Pena-Garay, “Solar models and solar neutrino oscillations,” *New J. Phys.*, vol. 6, p. 63, 2004.
- [BSS] R. Beuselinck, J. Sedgbeer, and Y. Shitov. The Supernemo Experiment. [Online]. Available: <http://www.imperial.ac.uk/research/hep/research/supernemo.htm>
- [Col04] K. Collaboration. (2004) KATRIN Design Report 2004. [Online]. Available: <http://www-ik.fzk.de/~katrin/publications/documents/DesignReport2004-12Jan2005.pdf>
- [Dav94] R. Davis, “A review of the homestake solar neutrino experiment,” *Progress in Particle and Nuclear Physics*, vol. 32, pp. 13–32, 1994. [Online]. Available: <http://www.sciencedirect.com/science/article/B6TJC-471XBFN-H/2/2af56436c91f2ca64bb2619efed29555>
- [DT08] N. Doss and J. Tennyson, “Excitations to the electronic continuum of  $3\text{He}^+$  in investigations of  $t_2$   $\beta$ -decay experiments,” *Journal of Physics B: Atomic, Molecular and Optical Physics*, vol. 41, no. 12, p. 125701, 2008. [Online]. Available: <http://stacks.iop.org/0953-4075/41/i=12/a=125701>
- [E<sup>+</sup>03] K. Eguchi *et al.*, “First results from KamLAND: Evidence for reactor anti-neutrino disappearance,” *Phys. Rev. Lett.*, vol. 90, p. 021802, 2003.
- [F<sup>+</sup>98] Y. Fukuda *et al.*, “Evidence for oscillation of atmospheric neutrinos,” *Phys. Rev. Lett.*, vol. 81, no. 8, pp. 1562–1567, Aug 1998.
- [Fer34] E. Fermi, “Versuch einer Theorie der Betastrahlen,” *Zeitschrift für Physik*, vol. 88, pp. 161–177, 1934.
- [GGN03] M. C. Gonzalez-Garcia and Y. Nir, “Neutrino masses and mixing: evidence and implications,” *Rev. Mod. Phys.*, vol. 75, no. 2, pp. 345–402, Mar 2003.
- [GK07] C. Giunti and C. W. Kim, *Fundamentals of Neutrino Physics and Astrophysics*. Oxford University Press, 2007.
- [Glü02] F. Glück. (2002, Apr.) Runge-Kutta method for numerical solution of differential equation system. [Online]. Available: <http://fuzzy.fzk.de/bscw/bscw.cgi/d479152/rungekutta.pdf>
- [Glü06] ——. (2006) C-programs for electromagnetic design. [Online]. Available: <https://fuzzy.fzk.de/bscw/bscw.cgi/34401>
- [Glü09a] ——. “Axisymmetric electric field calculation with zonal harmonic expansion,” 2009.

- [Glü09b] ——. (2009, Mar.) Secondary electron emission in the pre-spectrometer and in the Mainz spectrometer. [Online]. Available: <https://fuzzy.fzk.de/bscw/bscw.cgi/d540741/95-TRP-4652-A5-FGlueck.ppt>
- [GMO<sup>+</sup>09] F. Glück, S. Mertens, A. Osipowicz, P. Plischke, J. Reich, and N. Wandkowsky. (2009, Mar.) Air Coil System and Magnetic Field Sensor System. [Online]. Available: <http://fuzzy.fzk.de/bscw/bscw.cgi/d530439/Air%20Coil%20System%20and%20Magnetic%20Field%20Sensor%20System.pdf>
- [H<sup>+</sup>88] K. S. Hirata *et al.*, “Experimental Study of the Atmospheric Neutrino Flux,” *Phys. Lett.*, vol. B205, p. 416, 1988.
- [H<sup>+</sup>99] W. Hampel *et al.*, “Gallex solar neutrino observations: results for gallex iv,” *Physics Letters B*, vol. 447, no. 1-2, pp. 127–133, 1999. [Online]. Available: <http://www.sciencedirect.com/science/article/B6TVN-3VR1H2M-M/2/160790dfc1442b029b4f20ba4221d640>
- [Hal06] C. Hall. (2006, Oct.) Proposal for neutrino physics with superconductive bolometers in DUSEL. [Online]. Available: [http://mare.dfm.uninsubria.it/frontend/docs/Hall\\_Goddard\\_NSF\\_Oct31.pdf](http://mare.dfm.uninsubria.it/frontend/docs/Hall_Goddard_NSF_Oct31.pdf)
- [Han05] S. Hannestad, “Neutrino mass bounds from cosmology,” *Nuclear Physics B - Proceedings Supplements*, vol. 145, pp. 313–318, 2005, nOW 2004. [Online]. Available: <http://www.sciencedirect.com/science/article/B6TVD-4G3CBPY-2C/2/a3e4c3334362d0f4e56520ea60e34197>
- [HK89] P. W. Hawkes and E. Kasper, *Principles of Electron Optics*. Academic Press, 1989, vol. 1.
- [Höt09] M. Hötzel, “Berechnung von KATRIN Messspektren unter Einbeziehung der fensterlosen gasförmigen Tritiumquelle,” Master’s thesis, Universität Karlsruhe, 2009.
- [Jac98] J. D. Jackson, “Classical electrodynamics,” 1998.
- [Kay03] B. Kayser, “Neutrino Mass, Mixing, and Flavor Change,” in *Neutrino Mass*, G. Altarelli & K. Winter, Ed., 2003, pp. 1–+.
- [KKDHK01] H. V. Klapdor-Kleingrothaus, A. Dietz, H. L. Harney, and I. V. Krivosheina, “Evidence for Neutrinoless Double Beta Decay,” *Mod. Phys. Lett.*, vol. A16, pp. 2409–2420, 2001.
- [KST87] E. W. Kolb, A. J. Stebbins, and M. S. Turner, “How reliable are neutrino mass limits derived from sn1987a?” *Phys. Rev. D*, vol. 35, no. 12, pp. 3598–3606, Jun 1987.
- [Las06] M. G. T. Lasserre, “Double chooz, a search for the neutrino mixing angle theta-13,” 2006. [Online]. Available: <http://www.citebase.org/abstract?id=oai:arXiv.org:hep-ex/0606025>
- [LL02] T. J. Loredo and D. Q. Lamb, “Bayesian analysis of neutrinos observed from supernova sn 1987a,” *Phys. Rev. D*, vol. 65, no. 6, p. 063002, Feb 2002.

- [Mur08] Murayama. (2008) Oscillation Parameter Plots. [Online]. Available: <http://hitoshi.berkeley.edu/neutrino/>
- [O<sup>+</sup>] A. Osipovicz *et al.* KATRIN Letter of Intend. [Online]. Available: <http://www-ik1.fzk.de/tritium/publications/documents/loi.ps>
- [Obl] N. Oblath. Kassiopeia. [Online]. Available: [http://fuzzy.fzk.de/bscw/bscw.cgi/d630345/Oblath\\_Kassiopeia.pdf](http://fuzzy.fzk.de/bscw/bscw.cgi/d630345/Oblath_Kassiopeia.pdf)
- [Pap96] L. Papula, *Mathematik für Ingenieure und Naturwissenschaftler*. Vieweg + Teubner, 1996, vol. 2.
- [PTVF07] W. H. Press, S. A. Teukolsky, W. T. Vetterling, and B. P. Flannery, *Numerical Recipes*, 3rd ed. Cambridge University Press, 2007.
- [Rei10] J. Reich. (2010, Mar.) Simulation of Magnetic Materials in the Main Spectrometer Hall. [Online]. Available: <http://fuzzy.fzk.de/bscw/bscw.cgi/d631077/95-TRP-4843-A3-JReich.ppt>
- [rep] KATRIN Software Repository. [Online]. Available: <https://nustorage.uni-muenster.de/svn/katrin/>
- [ReW83] W. W. Repko and C. en Wu, “Radiative corrections to the end point of the tritium  $\beta$  decay spectrum,” *Phys. Rev. C*, vol. 28, no. 6, pp. 2433–2436, Dec 1983.
- [ROO] ROOT, a data analysis framework. [Online]. Available: <http://root.cern.ch>
- [Thu02] T. Thuemmler, “Entwicklung von Methoden zur Untergrundreduzierung am Mainzer Tritium- $\beta$ -Spektrometer,” Master’s thesis, Johannes Gutenberg Universität Mainz, Januar 2002. [Online]. Available: <http://fuzzy.fzk.de/bscw/bscw.cgi/d25072/dth-thuemmler1.pdf>
- [Ver78] J. H. Verner, “Explicit Runge-Kutta methods with estimates of the local truncation error,” *SIAM J. Numer. Anal.*, vol. 15, no. 4, pp. 772–790, Aug. 1978.
- [Wei] C. Weinheimer, “Laboratory limits on neutrino masses,” in \*Altarelli, G. (ed.) et al.: Neutrino mass\* 25-52.

# Acknowledgments

An dieser Stelle möchte ich all denjenigen Danken, die zum guten Gelingen dieser Arbeit zugetragen haben. Mein Dank gebührt hierbei besonders folgenden Personen:

- PROF. DR. GUIDO DREXLIN für die anspruchsvolle Aufgabenstellung und die gute Betreuung während der gesamten Zeit,
- DR. FERENC GLÜCK für das Bereitstellen und Erklären seiner zahlreichen Programme, auf denen diese Arbeit basiert, sowie auch für die zahlreichen physikalischen Diskussionen, die beispielhafte Betreuung und das Korrekturlesen meiner Arbeit,
- DIPL.-PHYS. SUSANNE MERTENS für ihre sehr gute Betreuung, die Geduld bei technischen und physikalischen Diskussionen und bei der Beantwortung all meiner Fragen und dem Korrekturlesen meiner Arbeit,
- DIPL.-PHYS. NANCY WANDKOWSKY für das eifrige Korrekturlesen dieser Arbeit,
- ALLEN MITARBEITERN DES INSTITUTS FÜR KERNPHYSIK am Karlsruhe Institut für Technologie für die angenehme Arbeitsatmosphäre und die stets vorhandene Hilfsbereitschaft, sowie jedem, der nicht namentlich erwähnt ist.

Ganz besonders danken möchte ich meiner Familie, ohne deren Unterstützung, besonders moralisch, aber auch finanziell, die ich während meines gesamten Studiums genossen habe, diese Arbeit nicht möglich gewesen wäre.